EARLY DETECTION OF STRESS CHANGES AND FAILURE USING ACOUSTIC MEASUREMENTS

EARLY DETECTION OF STRESS CHANGES AND FAILURE USING ACOUSTIC MEASUREMENTS

Proefschrift

ter verkrijging van de graad van doctor
aan de Technische Universiteit Delft,
op gezag van de Rector Magnificus Prof. dr. ir. T.H.J.J. van der Hagen,
voorzitter van het College voor Promoties,
in het openbaar te verdedigen op vrijdag 7 juni 2024 om 10:00 uur

door

Aukje Veerle VELTMEIJER

Master of Science in Toegepaste Geofysica,
Technische Universiteit Delft, Delft, Nederland,
geboren te Delft, Nederland.

Dit proefschrift is goedgekeurd door de promotoren

Samenstelling promotiecommissie:

Rector Magnificus,	voorzitter
Dr. A. Barnhoorn,	Technische Universiteit Delft, promotor
Prof. dr. ir. C.P.A. Wapenaar,	Technische Universiteit Delft, promotor
Onafhankelijke leden:	
Dr. E. Skurtveit,	U. of Oslo, Norway / NGI, Norway
Prof. dr. L.G. Evers,	Technische Universiteit Delft
Dr. ir. F.C. Vossepoel,	Technische Universiteit Delft
Prof. dr. ir. E.C. Slob,	Technische Universiteit Delft
Prof. dr. ir. D.M.J. Smeulders,	Technische Universiteit Eindhoven

Dit werk heeft financiële steun gekregen van de Nederlandse Organisatie voor Wetenschappelijk Onderzoek, Subsidienummer: DEEP.NL.2018.048

Keywords: Fault Reactivation, Coda Wave Interferometry, Induced Seismicity, Ultrasonic Monitoring

Printed by: Gildeprint

Front & Back: Picture by Marieke de Lorijn

ISBN 978-94-6384-596-0

An electronic version of this dissertation is available at
http://repository.tudelft.nl/.

Science is a wonderful thing
if one does not have to earn one's living at it.

Albert Einstein

CONTENTS

SUMMARY

Activities underground, such as gas extraction or fluid injection, can disturb the natural stresses present and can cause human-induced earthquakes along pre-existing faults. Even though they are related to engineering, these earthquakes are currently unpredictable. Monitoring and understanding how these earthquakes occur are essential for a safe use of the subsurface and to progress with mitigation measures and earthquake forecasting.

Current monitoring relies on post-failure seismic recordings, emphasizing the need for advancements in monitoring and forecasting techniques. Detecting stress changes before seismicity (pre-failure) occurs allows for the timely implementation of mitigation measures. Active seismic monitoring methods have the potential to detect stress changes early and as such precursory information that can improve the forecasting methods and models. However, there is still much to discover regarding the relationship between precursors and the underlying physics. In general, the common fault mechanisms during the seismic cycle are well known. Initial stress build-up is followed by first slip instabilities where the local stress exceeds the fault strength, leading up to a seismic event, during which stress on the fault is released. However, robust and reliable predicting of fault failure and the resulting earthquake has proven to be challenging even for reactivating experimental faults in a controlled laboratory setting.

This thesis uses ultrasonic transmission measurements in laboratory rock mechanic experiments, investigating the relation between seismic precursors and failure under various stress and deformation scenarios to mimic different subsurface stress conditions. The Red Felser sandstones used in this work originate from the Rotliegend formation, which is the same formation as the Groningen reservoir sandstones. Time-lapse monitoring is performed by analyzing the evolution of subsequent transmitted wavefields. Changes in velocity or attenuation between two consecutive wavefields are attributed to structural changes in the rock samples caused by imposed stress changes. By detecting these stress changes early, precursory signals to failure and fault reactivation are extracted. In seismics, the velocity of the first incoming waves is often used to determine rock properties, however, these direct wave velocities can be insensitive to small stress changes. Coda waves, scattering through the samples, show increased sensitivity to subtle perturbations, such as small stress changes. Coda wave interferometry and decorrelation are used to extract velocity changes and scattering information from the coda. The evolution of these coda parameters and attenuation over time are used to obtain precursory signals to failure.

Ultrasonic transmission measurements during the failure of Red Felser sandstones are performed. By loading sandstones until they break, the changing ultrasonic parameters can be analysed. A clear dependence of ultrasonic parameters on (micro-) crack growth leading to failure of sandstone samples is shown. A traffic light forecasting system, based on ultrasonic transmission monitoring, is proposed for detecting upcoming

failure in various subsurface conditions. This methodology is extended to monitoring fault reactivation, by identifying precursory signals to stress-driven fault reactivation from both both P- and S-waves monitoring. Sandstone samples, including a saw-cut fault, are cyclically reactivated by increasing the stresses on the sample. The pre-slip phase of fault reactivation is identified and linked to the physical processes of asperity degradation and creep. Subsequently, acoustic emissions (AE) are recorded. The precursory signals from the active monitoring method occur earlier and are slightly more sensitive to reactivation than the passive (AE) method, with the biggest advantage of being independent of the seismicity-generated movement along the fault.

The ultrasonic transmission method is further expanded to investigate fluid injection-driven fault reactivation of smooth and rough fault planes. Stress variations in the subsurface are often caused by variations in pore fluid pressure, and by increasing pore pressure in faulted sandstones fault movement is imposed. Analyzing the temporal evolution of coda waves and seismic amplitudes, this work identifies stress changes on the fault surface. It outlines the stages in the laboratory seismic cycle, serving as a basis for forecasting injection-induced fault-slip and establishes a link between seismic precursory signals and the mechanisms of failure, indicating the destruction of fault plane asperities (gouge formation) and the opening of the fault, resulting in decreased asperity contact. It shows the sensitivity of velocity change obtained from coda wave interferometry during the pre-slip phase and fault reactivation, especially in scenarios with a more complex fault plane. However, as all compared attributes are derived from the same waveforms, a combination of these properties demonstrates best that stress changes along the fault can be inferred with greater accuracy. Consequently, this combined approach proves useful for monitoring faulted or critically stressed reservoirs experiencing pore pressure changes.

A first step in up-scaling the monitoring method is presented to verify analytical and numerical models that suggest that fault reactivation in Groningen is initiated by the growth of small slip patches nucleating on the corners of offset faults. A layered sample with a displaced normal fault, designed to replicate Groningen's faults, is employed to investigate slip nucleation in a laboratory setting. Both stress and depletion cycles are executed to induce fault instability and reactivation. With the ultrasonic transmission method, these imposed stress changes can be monitored and possible (a-seismic) slip patches are identified, highlighting the benefit of active monitoring.

This thesis demonstrates the monitoring potential of ultrasonic transmission measurements and validates the method's robustness by effectively detecting stress changes leading to failure under various subsurface stress conditions. Emphasizing the significance of coda waves and attenuation as precursors to stress changes and linking them with physical processes within the sample this thesis contributes to an improved understanding of the relation between precursors and mechanisms of failure. The potential to infer (aseismic) stress changes pointing toward seismicity from active ultrasonic campaigns can be of added value to future monitoring and forecasting (models).

SAMENVATTING

De natuurlijke spanningen in de diepe ondergrond kunnen worden verstoord door bedrijvigheid, zoals gasproductie, waterinjectie of ondergrondse CO_2 opslag. Als dit gebeurt om en nabij bestaande breuken in de ondergrond kunnen deze activiteiten aardbevingen veroorzaken. Dit soort aardbevingen zijn momenteel nog zeer onvoorspelbaar, ondanks dat deze worden veroorzaakt door engineering projecten. Het begrijpen, waarom en hoe deze aardbevingen ontstaan en het monitoren hiervan is essentieel voor een veilig gebruik van de ondergrond en belangrijk voor de implementatie van risico beperkende maatregelen en aardbevingsvoorspellingen.

Het huidige monitoring stelsel is gebaseerd op het seismo-akoestische registreren van aardbevingen, dus het meten nadat een beving is geïnduceerd. Verbetering in monitoringmethodes en modellen om aardbevingen te voorspellen is dus hard nodig. Door drukveranderingen in de ondergrond te meten voordat een aardbeving is veroorzaakt, is er mogelijk genoeg tijd om passende maatregelen te nemen. Actief seismisch monitoren heeft het potentieel om drukveranderingen vroegtijdig te detecteren en deze metingen kunnen als waarschuwingssignaal dienen en voorspellingsmethodes en modellen verbeteren. Hiervoor is wel nodig om de relatie tussen het waarschuwingssignaal en de onderliggende natuurkunde te begrijpen.

Over het algemeen zijn de verschillende stappen van de seismische cyclus bekend. Initiële spanningsopbouw wordt gevolgd door lokale instabiliteiten langs de breuklijn waar de opgebouwde spanning groter is dan de breuk sterk. Dit leidt vervolgens tot instabiliteit en beweging langs de gehele breuk en seismiciteit (de aardbeving) wordt gegenereerd, waarbij de opgebouwde druk op de breuk wordt vrijgegeven. Echter het betrouwbaar voorspellen van breuk beweging en de daaruit gegenereerde aardbevingen is zeer moeilijk, zelfs het voorspellen van een in een laboratorium gemaakte aardbeving in een gecontroleerde omgeving blijft een uitdaging.

In dit proefschrift worden laboratoriumexperimenten uitgevoerd waarbij ultrasone transmissiemetingen door gesteentes worden gedaan. Hierbij wordt de relatie tussen de seismische waarschuwingssignalen en het breken of schuiven van gesteente onderzocht. Verschillende druk en deformatie scenario's, die de verschillende ondergrondse spanningsomstandigheden nabootsen, zijn getest. De rode Felser zandstenen die in deze experimenten zijn gebruikt komen uit de Rotliegend, dit is dezelfde formatie als de zandstenen die de Groningen reservoir uitmaken. Door de opeenvolgende gezonden golfvelden te analyseren wordt tijdsafhankelijke monitoring uitgevoerd. Snelheidsveranderingen of verandering in de demping van de gestuurde golven kunnen worden toegeschreven aan fysische veranderingen in de steenkernen, die zijn ontstaan door de opgelegde drukken. Door deze drukveranderingen vroegtijdig te detecteren, kunnen waarschuwingssignalen worden bepaald uit de tijdsafhankelijke analyse, die kunnen waarschuwen voor het breken van gesteente en de beweging van breuken.

Om de golfsnelheid en gesteente eigenschappen te bepalen wordt vaak de eerst binnenkomende golf gebruikt, maar deze directe golfsnelheden zijn vaak ongevoelig voor minieme drukveranderingen. De staart van de golf komt achter de eerst binnenkomende golf aan en heet de coda-golf. Deze coda-golf wordt meerdere keren weerkaatst binnen in een steenkern en is daardoor een stuk gevoeliger voor kleine veranderingen. Coda-golf interferometrie en decorrelatie worden gebruikt om veranderingen in de snelheid en de weerkaatsing van de coda-golf te bepalen. De tijdsafhankelijke evolutie van deze coda-golfeigenschappen en de demping van de golven worden vervolgens gebruikt om waarschuwingssignalen te bepalen.

Door zandsteenkernen te belasten tot ze breken, kunnen de veranderende gemeten golfeigenschappen worden gekoppeld aan de deformatie van het gesteente, namelijk de creatie en het groeien van (micro-) barsten, die uiteindelijk ervoor zorgen dat de zandsteen breekt. Een vroegtijdige waarschuwingsmethode gebaseerd op de golfeigenschappen is geïntroduceerd om te waarschuwen voor het falen van gesteente in verschillende ondergrondse spanningsomstandigheden.

Deze waarschuwingsmethode gebaseerd op de veranderende golfeigenschappen is uitgebreid naar het meten en monitoren van breukbewegingen gebruikmakend van zowel compressiegolven (P-golven) als schuifgolven (S-golven). Beweging langs een breuk is opgelegd door de druk cyclisch te verhogen op een doorgezaagde zandsteenkern. Het voorstadium van breukbeweging kan worden geïdentificeerd uit specifieke kenmerken in tijdsafhankelijke evolutie van de seismische data en kan vervolgens worden gelinkt aan de fysische processen langs het breukvlak, zoals kruipbeweging en contactdegradatie. Daarnaast zijn ook akoestische emissie (AE) metingen gedaan. Hieruit kan worden bepaald dat de waarschuwingssignalen uit de actieve monitoringmethode (ultrasone transmissiemetingen) eerder komen dan van de passieve methode (AE-metingen) en dus gevoeliger zijn voor kleine drukveranderingen die tot breukbeweging leiden. Ook heeft de actieve monitoringmethode het voordeel dat deze onafhankelijk is van seismisch gegenereerde beweging langs de breuk.

De ultrasone transmissie meetmethode is uitgebreid naar het detecteren van breukbeweging die door vloeistofinjectie is veroorzaakt. Dit is onderzocht voor beweging langs zowel gladde als ruwe breukvlakken. Spanningsveranderingen in de ondergrond worden vaak veroorzaakt door variaties in de vloeistofdruk in de poriën van een gesteente, dit is nagebootst door de vloeistof druk in een kern met een breuk te verhogen. Met de tijdsafhankelijke analyse van de coda-golven en golf amplitudes kunnen de drukveranderingen langs de breuk in kaart worden gebracht. Aan de hand van deze parameters kunnen de verschillende fases van de seismische cyclus worden vastgesteld. Dit vormt de basis tot het voorspellen van breukbeweging en legt het verband tussen de fysische mechanismes die tot breukbeweging leiden. Dit zijn het openen van de breuk, wat leidt tot verminderd contact en het kapot maken van de zandkorrelcontacten, wat zorgt voor slipvorming langs het oppervlak van de breuk. De resultaten laten zien dat vooral de coda-golf gevoelig is voor de verandering langs de breuk in het voorstadium tot beweging, zeker in het geval van een complex breukoppervlak. Echter, alle parameters uit dezelfde golf zijn afgeleid, en met de combinatie van de verschillende parameters kunnen de drukveranderingen langs de breuk nauwkeuriger worden bepaald. De combinatie van kenmerken is dus zeer nuttig voor het monitoren van kritiek gespannen

reservoirs (met breuken) die veranderingen in vloeistofdruk ondergaan.

Een eerste stap in het opschalen van de monitoringmethode wordt ook gepresenteerd. Deze stap is ontworpen om analytische en numerieke modellen te verifiëren in een laboratoriumexperiment. Deze modellen suggereren dat de aardbevingen in Groningen ontstaan vanuit de hoekpunten van het gasreservoir daar waar breuken het reservoir doorkruisen. Een teststuk, met hierin een breuk die verschillende verschoven lagen doorkruist is ontworpen om de situatie in de Groningse ondergrond na te bootsen. Om de breuk te laten bewegen is zowel de verticale druk als de vloeistofdruk cyclisch verhoogd. Gebruik makend van de ultrasone transmissie meetmethode kan de opgelegde drukverandering worden gevolgd en potentiële lokale instabiliteit langs het breukvlak worden opgemerkt.

Dit proefschrift toont het potentieel van de ultrasone transmissie meetmethode. Veranderingen in druk worden waargenomen voordat er breuk beweging plaatsvindt voor verschillende ondergrondse spanningsomstandigheden. Het belang van de coda-golven en de demping als waarschuwingssignalen wordt benadrukt samen met de mogelijkheid om deze signalen te koppelen aan de fysische werkingen in de zandsteen teststukken. Daarbij draagt dit onderzoek bij aan de relatie tussen de gevonden waarschuwingssignalen en de onderliggende natuurkunde, met als grote toegevoegde waarde dat deze methode niet berust op het registreren van aardbevingen. De getoonde resultaten en de gepresenteerde ultrasone transmissie meetmethode kunnen van grote waarde zijn voor toekomstige (ondergrondse) monitoringsactiviteiten en in aardbevingsvoorspellingen.

1

INTRODUCTION

Climate change is becoming increasingly evident, showing accelerating ice melt, rising sea levels, and record-breaking heat waves (Copernicus Climate Change Service, 2023). With the aim of a net-zero carbon economy in the future and staying within the 1.5 degree Celsius temperature increase, governments are shifting from fossil fuels towards renewable energy sources. In the need to combat climate change, policymakers also explore alternative uses of the subsurface (IPCC, 2023). While the subsurface previously contributed primarily to the extraction of fossil fuels such as oil and gas, the focus shifted towards the subsurface as a source of thermal resources, such as geothermal heating for houses. Additionally, it offers potential for gas storage in porous reservoirs or geological formations, such as underground CO_2 (Bui et al., 2018) or hydrogen storage (Patonia & Poudineh, 2023). To ensure the safety of these operations, it is crucial to understand the subsurface and the impact of these subsurface activities on altering the present stress conditions. A well-known example of subsurface activities gone wrong is the Groningen gas production, where gas extraction led to differential stresses along pre-existing faults in the subsurface resulting in induced seismicity in relatively densely populated areas. This had a significant societal impact, leading to the closure of the gas field even before it was depleted. Another well-known case involves the geothermal project in Basel, Switzerland, where a large earthquake was induced. This also resulted in stopping the renewable energy project.

Understanding and monitoring the degree of induced stress changes are therefore vital for the continuation of underground projects, especially when located near densely populated areas, as is often the case with geothermal operations. Heat can not be transported over large distances and is therefore consumed locally. Monitoring is currently either nonexistent or limited, often relying on seismometers to detect the seismicity as it occurs. A clear disadvantage is that this recording happens after the fact, after all, seismicity (or earthquakes) only happens due to instability in the subsurface caused by stress changes along pre-existing faults. Ensuring the safe use of the subsurface requires preventing these instabilities. Therefore, there is a need for a robust monitoring system, capable of detecting stress changes before seismicity, with the ultimate future goal

of forecasting seismicity, enabling strategies such as adjusting production methods to mitigate seismic events or providing warnings to the population.

While researchers have investigated earthquake rupture mechanisms for many years, much remains unknown, and accurate forecasting remains elusive, making the occurrence of (induced) earthquakes unpredictable even in a laboratory setting. Various precursory signals have been identified in hindsight of earthquakes, such as precursory foreshocks in the recent M7.8 Türkiye earthquake (Picozzi et al., 2023). The challenge lies in the fact that different fault zones have distinct rupture mechanisms, and not every sequence of (fore)shocks will lead to an earthquake. Active monitoring methods have the potential to improve forecasting methods and models. To date, only limited studies have been conducted in the field to identify precursory signals to earthquakes, therefore there is still much to discover regarding the relationship between precursors and the underlying physics.

In general, the common fault mechanisms occurring during the seismic cycle are well known. This involves initial stress build-up followed by first slip instabilities there where the local stress exceeds the fault strength, leading up to a seismic event, during which stress on the fault is released. Generally speaking, stress changes can be inferred by analyzing the change in acoustic or seismic velocity (Barnhoorn et al., 2018; Hall, 2009; Zhubayev et al., 2016). In particular, it has been shown that the coda of the acoustic wave traveling through the medium is exceptionally sensitive to changes in the microstructure (Hadziioannou et al., 2009; Sang et al., 2020; Zotz-Wilson et al., 2019). However, robust, reliable predicting of fault failure and the resulting earthquake has proven to be challenging even for experimental faults under a controlled laboratory setting.

1.1. THESIS OBJECTIVES

The earthquakes in Groningen have highlighted the significant impact seismicity can have on society and underscored the extensive gaps in our understanding of the subsurface. Despite being one of the best-monitored and most studied gas fields, much remains unknown about how the (Groningen) subsurface responds to induced (local) stress changes, making it challenging to forecast future induced earthquakes

Predicting the degree of induced stress changes, consequently, the potential onset and exact location of failure and seismicity, is highly challenging. Developing effective techniques for monitoring these changes is crucial for better prediction and, consequently, mitigation of failure and seismicity in the subsurface.

This requires more and better understanding of the onset of seismic activity in the deep subsurface. Geophysical methods can be used for monitoring seismic velocities, which provide insight into mechanical (rigidity, density, etc.) evolution (Schubnel et al., 2006). This thesis aims to monitor local stress changes for forecasting by identifying key precursory signals through active monitoring and improving the relationship between these precursors and the mechanics of rock failure and fault reactivation.

This is realized by developing a robust active ultrasonic monitoring method in the laboratory. Key parameters are derived from coda wave analysis and attenuation properties, analyzing the temporal evolution of the recorded ultrasonic waves. Precursory indicators to the onset of material failure and fault reactivation under different subsurface stress conditions are identified and coupled with geomechanical processes within

the samples. Upscaling within the laboratory is performed to investigate the effect of increasing complexity on the obtained precursory signals

1.2. INDUCED SEISMICITY IN GRONINGEN

The gas reservoir in Groningen, known as the Groningen gas field, is located in the Slochteren formation within the Upper Permian Rotliegend Group (de Jager & Visser, 2017). The gas in Groningen originates from the Carboniferous layers beneath the reservoir, and is trapped within the reservoir by the overlaying Ten Boer Claystone, which is capped by a thick salt layer of the Zechstein Group (from tens of meters to more than a kilometer) (de Jager & Visser, 2017; TNO & Ministerie van Economische Zaken, 2020; van Thienen-Visser & Breunese, 2015). The reservoir depth ranges from about 2600 to 3100 meters (Burkitov et al., 2016; de Jager & Visser, 2017; TNO & Ministerie van Economische Zaken, 2020; van Thienen-Visser & Breunese, 2015) and is characterized by numerous normal faults with a predominant NNW-SSE trend, while others have orientations of E-W or N-S (de Jager & Visser, 2017).

The first seismicity associated with the gas extraction in Groningen was recorded in 1991 (TNO & Ministerie van Economische Zaken, 2020; van Thienen-Visser & Breunese, 2015) (Figure 1.1). Since this first event, the number of seismic events has increased over time with frequency and magnitude (van Thienen-Visser & Breunese, 2015), with the largest event to date, the Huizinge earthquake of magnitude 3.6 on August 16, 2012 (TNO & Ministerie van Economische Zaken, 2020; van Thienen-Visser & Breunese, 2015). Most induced events recorded in Groningen are located in the middle of the gas field (KNMI, 2023). This is also the area with the largest amount of subsidence (Figure 1.2) (NAM, 2013, 2016; Pijnenburg, 2019). The subsidence at the surface is a result of compaction of the reservoir due to the decrease in pore pressure and increase in effective vertical stress caused by the gas extraction (Pijnenburg, 2019; van Thienen-Visser & Breunese, 2015).

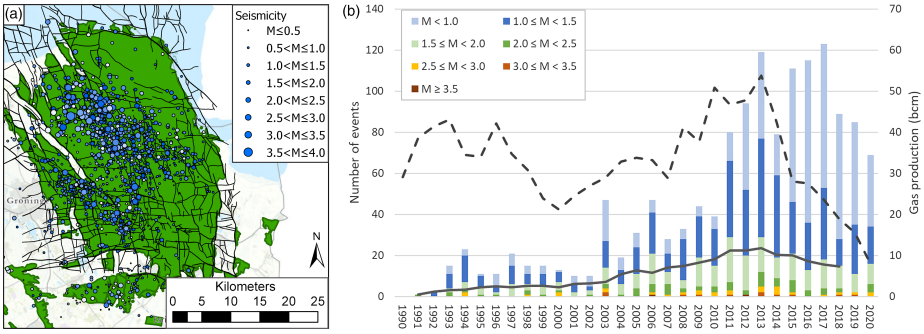

Figure 1.1: Overview of the induced seismicity in the Groningen gas field. (a) Location and size of the seismicity as reported by the KNMI (Royal Dutch Metrological Institute) on a map of the region. The grey lines indicate the faults within the reservoir. (b) The seismicity and annual gas production over time. The dark solid line shows the 5-year moving average of all M ≥ 1.5 events. The dark dashed line shows the annual gas production from the Groningen field in billion cubic metres. (taken from Muntendam-Bos et al. (2022))

This compaction in the reservoir is not uniformly distributed over the reservoir (Figure 1.2) (NAM, 2016; Pijnenburg, 2019; TNO & Ministerie van Economische Zaken, 2020;

van Thienen-Visser & Breunese, 2015; van Thienen-Visser & Fokker, 2017), due to the inability of existing faults to move. The compaction on each side of the fault induces shear stress changes along these faults and (Pijnenburg, 2019; van Thienen-Visser & Breunese, 2015) and when these shear stresses overcome the frictional forces of the fault, the fault can slip (van Thienen-Visser & Breunese, 2015). The energy released during this slip can then result in seismicity at the surface (Pijnenburg, 2019).

Studies have shown a relation between the gas extraction and seismic activity in Groningen (Muntendam-Bos et al., 2022; Vlek, 2019) (Figure 1.1). Due to the increasing number of seismic events and damage to buildings in Groningen the public concern has grown and due to the increased societal impact over the years, the Dutch government has changed its policy concerning gas extraction from the Groningen gas field (Vlek, 2019) and has decided the Groningen gas field will abandoned in October 2024 (Vijlbrief, J.A., Staatssecretaris van Economische Zaken en Klimaat, 2023). Despite the seismicity the Groningen gas field has provided large revenues for the Dutch government and a remainder of about 25% of the initial gas reserve will remain in place (de Jager & Visser, 2017; Pijnenburg, 2019)

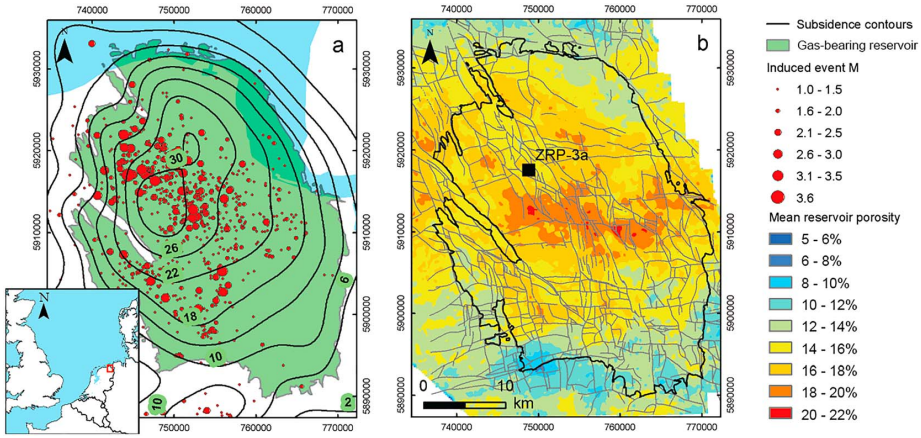

Figure 1.2: Map showing the location of the Groningen gas field. (a) Showing the extent of the gas reservoir, the contours showing the measured surface subsidence in 2013 and the location of the induced earthquakes scaled to magnitude. (b) Map showing the mean porosity of the Slochteren reservoir sandstone and the main faults cutting the top of the reservoir. (taken from Pijnenburg (2019))

1.3. STRESS SENSITIVITY

Geophysical methods can be used for monitoring seismic velocities, which provide insight into mechanical (rigidity, density, etc.) evolution (Schubnel et al., 2006). A number of geo-mechanical properties influence the propagation of elastic waves through a medium. Structural characteristics, including, rock type, mineralogy, porosity, and fluid type, but also environmental characteristics like effective stress (Hall, 2009), temperature (Snieder et al., 2002) and saturation (Grêt et al., 2006b) change the elastic moduli and thus influence the propagation (Hall, 2009). Stress changes can be quantified by

analysing the change in acoustic or seismic velocity change (Xie et al., 2018).

For intact rocks, it has been shown that seismic velocities change in response to stress, for example, due to compression of the rocks (Winkler & Nur, 1979). Increasing stresses on a rock sample cause closure of existing pore space, such as micro-cracks, this closure leads to an increase of seismic velocity, measured by the arrival time of the first P- or S-waves. The opposite, the creation of micro-fractures causes these velocities to drop (Barnhoorn et al., 2018; Sang et al., 2020). Despite the clear stress dependence of seismic velocities, inferring changes within a medium using direct waves can be ambiguous as they travel directly and hence sample the rock sample once (Figure 1.3). Research has shown that direct waves do not sample first (micro-) crack formation (Sang et al., 2020), whereas coda waves, which scatter through a medium (Figure 1.3), can detect small changes due to stress (Sang et al., 2020; Zotz-Wilson et al., 2019).

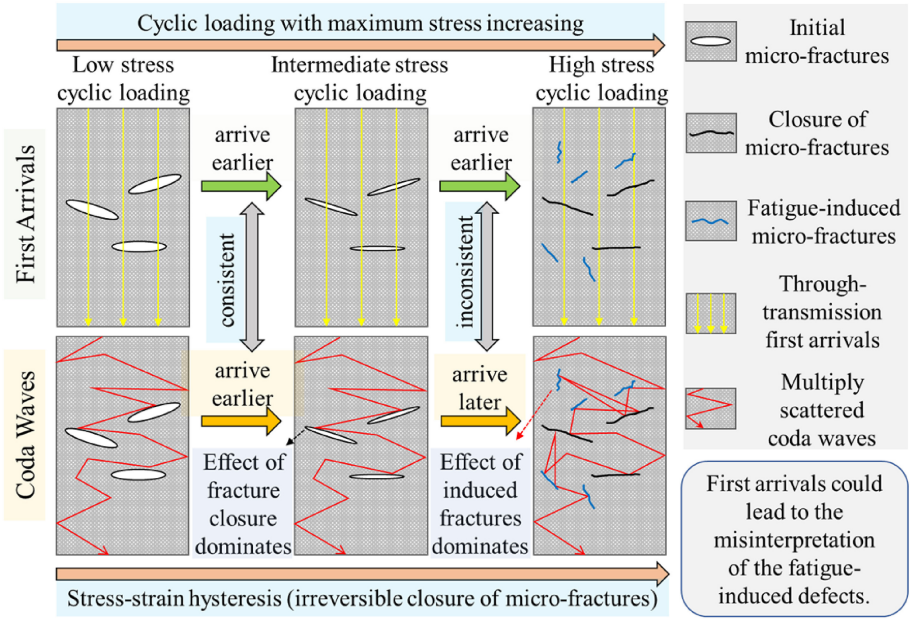

Figure 1.3: Schematic of the travel path of the first arrivals (yellow) and the scattered path of coda waves (red) under different stresses. Showing first arrivals sample the defects either once or not at all while coda waves sample the entire medium, increasing its sensitivity to small changes in the medium. (Taken from Sang et al., 2020)

1.4. CODA WAVE INTERFEROMETRY

The coda of a wave is the tail of wavelet recorded after the arrival of the direct waves (Aki & Chouet, 1975; Grêt et al., 2006b), this is visualized in Figure 1.4. The coda consists of multiply scattered waves (Snieder, 2006), by scattering within the medium it has sampled the (disturbed) medium multiple times (Figure 1.5) (Grêt et al., 2006a, 2006b; Snieder, 2006). Small changes therefore may be undetectable in direct waves but are amplified by the repeated sampling and thus detected by the coda (Grêt et al., 2006a, 2006b;

Snieder, 2006). Coda Wave Interferometry (CWI) tries tot obtain the average change in the scatter locations as a result of changes in medium. The changes in the medium are estimated by comparing the wave before and after the change (Snieder, 2006) by means of correlation.

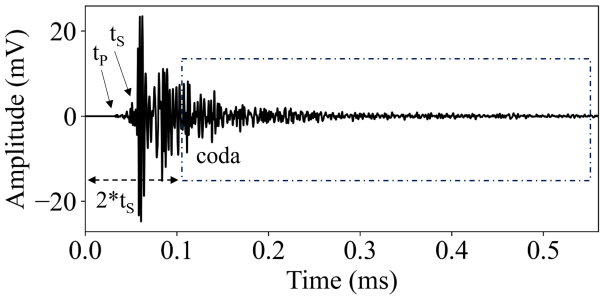

Figure 1.4: Different wave arrivals. The first arrival is the direct P-wave (t_P), followed by the direct S-wave (t_S). The tail of the wavelet is called the coda.

The theory of CWI as presented by Snieder (2006) states that the unperturbed wavefield u_u(t) can be written as a sum of all possible paths (P) the waves can travel through the medium, where t is time and A_P(t) is the wave along travel path P:

$$u_u(t) = \sum_P A_P(t). \tag{1.1}$$

Each scatterer in the medium is assumed to have stationary properties. Therefore, the scatterer does not change its size, shape, density, and velocity. Additionally, the distance between the individual scatterers is assumed to be much larger than the dominant wavelength (l » λ). The major differences between the wavefields, when the medium changes over time, are the arrival times of the waves propagating along each travel path P. The perturbed wavefield u_p(t) can thus be represented as

$$u_p(t) = \sum_P A_P(t - \delta t_P), \tag{1.2}$$

where δt_P is the travel time change along the path P. This implies that the perturbed wavefield shows only a change in time and does not change the dispersion of the wavefield. By comparing the wave fields the variations in the medium can be assessed. The cross-correlation coefficient is a common method to quantify these variations. The cross-correlation coefficient (CC) for a time window of width $2t_w$ and centered around time t_k is given by

$$CC(t_s) = \frac{\int_{t_k-t_w}^{t_k+t_w} u_u(t)u_p(t+t_s)dt}{\sqrt{\int_{t_k-t_w}^{t_k+t_w} u_u^2(t)dt \int_{t_k-t_w}^{t_k+t_w} u_p^2(t)dt}}. \tag{1.3}$$

The cross-correlation coefficient (CC) reaches its maximum if the travel time perturbation δt across all possible perturbed paths P is

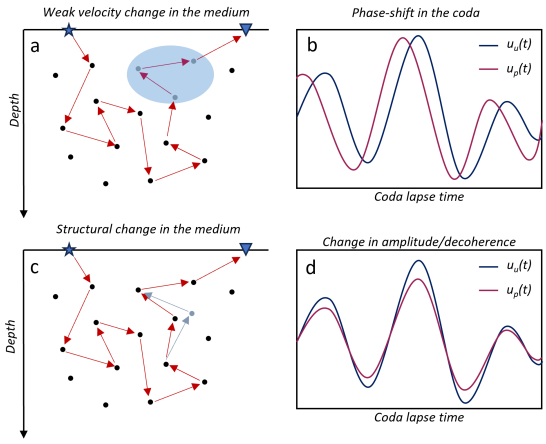

Figure 1.5: Effect of perturbation in subsurface on coda wave. (a) A small velocity change in the medium results in (b) a phase shift in the coda . (c) A structural change results in (d) a different scatterer patterns in the coda. (based at Obermann and Hillers, 2019)

$$\delta t = t_s. \tag{1.4}$$

The velocity change can be written as the average slope of δt versus t, assuming the time shift is constant in the considered time window, as follows:

$$\frac{\delta v}{v} = -\frac{\delta t}{t_s}. \tag{1.5}$$

To investigate the changes in material scattering, the decorrelation coefficient (K) is determined. The method of coda wave decorrelation (CWD) introduced by Larose et al., 2010 is based on the theory of Snieder, 2006. The decorrelation coefficient is formulated as

$$K(t_s) = 1 - CC(t_s) = 1 - \frac{\int_{t_k-t_w}^{t_k+t_w} u_{p_{j-N}}(t) u_{p_j}(t+t_s) dt}{\sqrt{\int_{t_k-t_w}^{t_k+t_w} u^2_{p_{j-N}}(t) dt \int_{t_k-t_w}^{t_k+t_w} u^2_{p_j}(t) dt}}, \tag{1.6}$$

where N is the number of measurements the reference wavefield u_{p_j-N}(t) is lagging behind the to-be-correlated wavefield u_{p_j}(t). For continuously monitoring the evolving scattering medium, a moving reference wavefield is used (c.f. Grêt et al., 2006b; Zotz-Wilson et al., 2019). The decorrelation coefficient K is related to the changes in material scattering due to the addition or removal of scatter(ers) in the medium (Planès et al., 2014, 2015). The coda waves seem random due to the complex paths they take through the medium, but the changes they are subjected to are strongly related to the position and strength of the material changes in the medium (Planès et al., 2014). The scattering

in a medium along the transport mean free path l can be described using the cross-sectional area of a single scatterer V_a and the density of scatterers ρ (Planès et al., 2014). The total scattering coefficient, as described by Aki and Chouet, 1975, is given by

$$g_0 = \rho V_a = l^{-1}. \tag{1.7}$$

Following the theory of Aki and Chouet, 1975, the coda decorrelation can be rewritten in terms of the scattering coefficient (g_0) between a perturbed (p) and unperturbed (u) medium (Zotz-Wilson, 2020).

$$K(t) = \frac{v_0}{2} t|\Delta g_{0_{p-u}}|, \tag{1.8}$$

where $K(t)$ is the theoretical decorrelation coefficient, t the time in the coda, and v_0 the velocity in the medium. Using a rolling reference (N=1), the changes in the absolute value of $|g_0|$ are monitored as a rate of change (e.g., Zotz-Wilson, 2020).

1.5. MOHR-COULOMB FAILURE CRITERION

Fractures can form due to changes in both stress states and fluid pressures. During stress increase of the sample, micro-fractures can form anywhere throughout the sample when stresses exceed the yield strength of the rock. From the onset of faulting, micro-fractures grow and start to connect in a narrow band, which can develop into a shear rupture plane (when testing with confining pressures) and leads to failure of the sample (Zhang & Li, 2019). After failure of the sample, only frictional sliding along the formed shear plane occurs (Zhang & Li, 2019).

Laboratory experiments often are performed using conventional triaxial testing where the $\sigma_1 > (\sigma_2 = \sigma_3)$. This is under the assumption σ_2 has little effect on the failure characteristics like in the Mohr-coulomb failure criteria (Haimson & Rudnicki, 2010). The Mohr-Coulombs theorem describes the compressive stress σ_1 required to cause failure at a confining stress σ_3 (Labuz & Zang, 2012). The curve enveloping all Mohr-circles, the failure envelope, corresponds to the critical stress states causing failure. The theorem describes that the intermediate principal stress σ_2 is not expected to affect the failure onset. Morh-Coulomb can also predict the angle of the formed fault plane. The normal vector of the failure plane makes an angle of β with the direction of the maximum stress (Jaeger et al., 2009). The Mohr-Coulomb criterion often used to describe shear failure in rocks is as follows (Kang et al., 2019);

$$\tau = C + \sigma_n \tan\phi \tag{1.9}$$

where τ is the shear strength, σ_n the normal stress acting on a fault, C is the cohesion, ϕ the angle of internal friction.

From the Mohr diagram the failure criterion can be derived using the principal stresses ($\sigma_1 > \sigma_3$) (Labuz & Zang, 2012):

$$\sigma_n = \frac{1}{2}(\sigma_1 + \sigma_3) - \frac{1}{2}(\sigma_1 - \sigma_3)\sin\phi \tag{1.10}$$

and

$$\tau_f = \frac{1}{2}(\sigma_1 - \sigma_3)\cos\phi \tag{1.11}$$

When a fault is present, the equation 1.9 describing Mohr-Coulomb failure can be rewritten as function of friction along the fault (Kang et al., 2019), often assuming no cohesion along the fault ($c_f = 0$).

$$\tau = \mu\sigma'_n = \mu_f(\sigma_n - P_f), \tag{1.12}$$

where μ is the friction along the fault interface, τ the shear stress, σ'_n the effective normal stress and σ_n the normal stress and P_f the pore pressure. Fault reactivation can occur when the pore pressure increases to the critical pressure, or stress change on the fault (Jaeger et al., 2009; Kang et al., 2019) (see Figure 1.6).

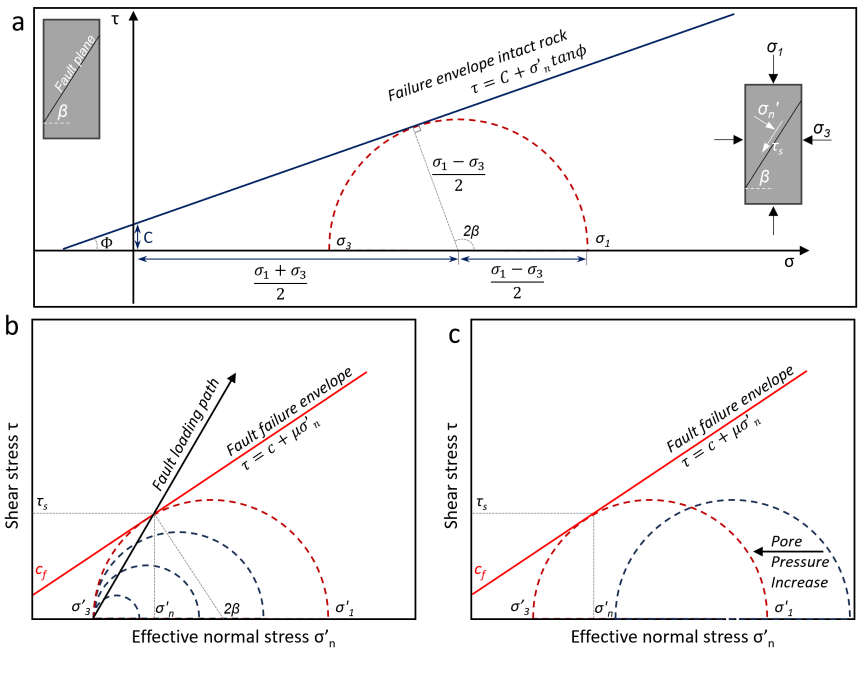

Figure 1.6: Illustrations explaining the Mohr-Coulomb theorem. a) The Mohr-Coulomb failure criterion b) Increasing stress can cause failure along fault plane as well as c) increasing pore pressure result in failure along the fault plane. Illustration is showing that, according to the Mohr-Coulomb hypothesis intermediate stress σ_2 has no influence on the onset of failure. σ_1, σ_2, and σ_3 are the principal stresses, c_f the cohesion of the fault and β the angle of the failure plane

1

1.6. OUTLINE

The thesis is composed of the following chapters:

- Chapter 2: *Forecasting of rock failure in the laboratory using active acoustic monitoring methods*
  In this chapter, I propose a traffic light forecasting system for rock failure using ultrasonic monitoring. Combining coda wave interferometry and attenuation properties to analyze the temporal evolution of the recorded ultrasonic seismic waves, the onset of rock failure can be robustly detected and upcoming failure foreseen. This system is applicable for forecasting failure at various subsurface stress conditions, aiding in the better prediction of small stress-induced changes in the subsurface and, consequently, the mitigation of failure and natural hazards.

- Chapter 3: *Precursory signals to the onset of laboratory stress-driven fault slip through acoustic monitoring*
  In this chapter, I investigate the robustness of the monitoring method to stress-driven fault reactivation and explore the differences between P- and S-wave monitoring under various subsurface stress conditions, demonstrating the sensitivity of the coda wave to the onset of fault reactivation. The precursory signals obtained from acoustic monitoring are connected to creep and pre-slip process along the fault plane before fault reactivation. A clear correlation between the stress state along the fault and the precursory signals is shown.

- Chapter 4: *Active and passive monitoring of fault reactivation under stress cycling*
  In this chapter, I combine both active and passive monitoring, demonstrating the complementary value of both methods. Active ultrasonic transmission measurements are analysed using coda wave interferometry and compared to acoustic emission recordings generated by fault reactivation and movement. This integration enhances the accuracy of monitoring and can lead to better seismic risk mitigation, particularly in monitoring faulted or critically stressed reservoirs undergoing cyclic stress behavior.

- Chapter 5: *Precursory signals to injection induced fault reactivation*
  In this chapter, fault reactivation and slip are monitored by identifying precursors from the temporal evolution of ultrasonic seismic waves and to understand the connection between precursors and mechanisms of failure. The results of injection-driven reactivation of fault experiments in combination with continuous active ultrasonic monitoring are presented. Fluid pressure is increased cyclically and stepwise to induce slip on the critically stressed saw-cut and in-situ faulted permeable Red-Felser sandstones. The various reactivation phases of the seismic reactivation cycle can be identified from the precursory signal for the reactivation of both smooth and rough fault planes.

- Chapter 6: *Monitoring stress variations in layered offset samples in a true triaxial setting.*
  In this chapter, the results of upscaled experiments are shown. By increasing the sample size, a complex geometry, including layers and an offset faulted reservoir,

can be tested. A combination of active (ultrasonic transmission measurements) and passive (acoustic emissions) monitoring is used to monitor stress changes within the sample due to cyclic stress and pore fluid variations. Coda wave decorrelation is used to show the variation in different stress directions and shows sensitivity to local stress variations along the fault plane.

- Chapter 7: *Conclusions and future outlook*
  In this chapter, a summary of the main findings presented in this thesis is given. Additionally, recommendations for future research are given.

- Appendix A: *Additional data large scale experiments*
  In this appendix, additional figures and pictures featuring the laboratory setup are shown for chapter 6.

- Appendix B: *Data availability.*
  In this appendix, the links to the data at the 4TU.ResearchData repository are listed. This data includes the loading data and waveforms acquired during experiments in the laboratory facilities at TU Delft.

REFERENCES

Aki, K., & Chouet, B. (1975). Origin of coda waves: Source, attenuation, and scattering effects. *Journal of Geophysical Research*, *80*(23), 3322–3342. https://doi.org/10.1029/jb080i023p03322

Barnhoorn, A., Verheij, J., Frehner, M., Zhubayev, A., & Houben, M. (2018). Experimental identification of the transition from elasticity to inelasticity from ultrasonic attenuation analyses. *Geophysics*, *83*(4), MR221–MR229. https://doi.org/10.1190/geo2017-0534.1

Bui, M., Adjiman, C. S., Bardow, A., Anthony, E. J., Boston, A., Brown, S., Fennell, P. S., Fuss, S., Galindo, A., Hackett, L. A., Hallett, J. P., Herzog, H. J., Jackson, G., Kemper, J., Krevor, S., Maitland, G. C., Matuszewski, M., Metcalfe, I. S., Petit, C., … Mac Dowell, N. (2018). Carbon capture and storage (CCS): The way forward. *Energy and Environmental Science*, *11*(5), 1062–1176. https://doi.org/10.1039/c7ee02342a

Burkitov, U., van Oeveren, H., & Valvatne, P. (2016). Groningen field review 2015 subsurface dynamic modelling report. *NAM Onderzoeksrapporten*. https://www.nam.nl

de Jager, J., & Visser, C. (2017). Geology of the Groningen field - An overview. *Netherlands Journal of Geosciences*, *96*(5), s3–s15.

Grêt, A., Snieder, R., & Özbay, U. (2006a). Monitoring in situ stress changes in a mining environment with coda wave interferometry. *Geophysical Journal International*, *167*(2), 504–508. https://doi.org/10.1111/j.1365-246X.2006.03097.x

Grêt, A., Snieder, R., & Scales, J. (2006b). Time-lapse monitoring of rock properties with coda wave interferometry. *Journal of Geophysical Research: Solid Earth*, *111*(3), 1–11. https://doi.org/10.1029/2004JB003354

Hadziioannou, C., Larose, E., Coutant, O., Roux, P., & Campillo, M. (2009). Stability of monitoring weak changes in multiply scattering media with ambient noise correlation: Laboratory experiments. *The Journal of the Acoustical Society of America*, *125*(6), 3688–3695. https://doi.org/10.1121/1.3125345

Haimson, B., & Rudnicki, J. W. (2010). The effect of the intermediate principal stress on fault formation and fault angle in siltstone. *Journal of Structural Geology*, *32*(11), 1701–1711.

Hall, S. A. (2009). *When geophysics met geomechanics: Imaging of geomechanical properties and processes using elastic waves* (D. Kolymbas & G. Viggiani, Eds.; VIII). Springer. https://doi.org/10.1007/978-3-642-03578-4

IPCC. (2023). Climate change 2022: Mitigation of climate change. the working group iii report provides an updated global assessment of climate change mitigation progress and pledges, and examines the sources of global emissions. https://www.ipcc.ch/report/sixth-assessment-report-working-group-3/

Jaeger, J. C., Cook, N. G., & Zimmerman, R. (2009). *Fundamentals of rock mechanics*. J. Wiley & Sons.

Kang, J., Zhu, J. B., & Zhao, J. (2019). A review of mechanisms of induced earthquakes: from a view of rock mechanics. *Geomechanics and Geophysics for Geo-Energy and Geo-Resources*, *5*(2), 171–196.

KNMI. (2023). Aardbevingen - complete catalogus voor Nederland en omgeving. *KNMI DataCentre*. https://data.knmi.nl/datasets/aardbevingen_catalogus/1

Labuz, J. F., & Zang, A. (2012). Mohr–Coulomb failure criterion. *Rock Mechanics and Rock Engineering*, *45*(6), 975–979. https://doi.org/10.1007/s00603-012-0281-7

Larose, E., Planes, T., Rossetto, V., & Margerin, L. (2010). Locating a small change in a multiple scattering environment. *Applied Physics Letters*, *96*(20), 1–4. https://doi.org/10.1063/1.3431269

Muntendam-Bos, A. G., Hoedeman, G., Polychronopoulou, K., Draganov, D., Weemstra, C., van der Zee, W., Bakker, R. R., & Roest, H. (2022). An overview of induced seismicity in the Netherlands. *Netherlands Journal of Geosciences*, *101*, e1. https://doi.org/10.1017/njg.2021.14

NAM. (2013). Technical addendum to the winningsplan groningen 2013 subsidence, induced earthquakes and seismic hazard analysis in the Groningen field.

NAM. (2016). Technical addendum to the winningsplan Groningen 2016 production, subsidence, induced earthquakes and seismic hazard and risk assessment in the Groningen field.

Obermann, A., & Hillers, G. (2019). Advances in geophysics. *Elsevier*, *60*, 65–143.

Patonia, A., & Poudineh, R. (2023). *Hydrogen storage for a net-zero carbon future*. https://www.oxfordenergy.org/publications/hydrogen-storage-for-a-net-zero-carbon-future/

Picozzi, M., Iaccarino, A. G., & Spallarossa, D. (2023). The preparatory process of the 2023 Mw 7.8 Türkiye earthquake. *Scientific Reports*, *13*(1), 1–10. https://doi.org/10.1038/s41598-023-45073-8

Pijnenburg, R. (2019). Deformation behavior of reservoir sandstones from the seismogenic groningen gas field: An experimental and mechanistic study. *Doctoral dissertation, Utrecht University*.

Planès, T., Larose, E., Margerin, L., Rossetto, V., & Sens-Schönfelder, C. (2014). Decorrelation and phase-shift of coda waves induced by local changes: Multiple scattering approach and numerical validation. *Waves in Random and Complex Media*, *24*(2), 99–125. https://doi.org/10.1080/17455030.2014.880821

Planès, T., Larose, E., Rossetto, V., & Margerin, L. (2015). Imaging multiple local changes in heterogeneous media with diffuse waves. *The Journal of the Acoustical Society of America*, *137*(2), 660–667. https://doi.org/10.1121/1.4906824

Sang, G., Liu, S., & Elsworth, D. (2020). Quantifying fatigue-damage and failure-precursors using ultrasonic coda wave interferometry. *International Journal of Rock Mechanics and Mining Sciences*, *131*(February), 104366. https://doi.org/10.1016/j.ijrmms.2020.104366

Schubnel, A., Benson, P. M., Thompson, B. D., Hazzard, J. F., & Paul Young, R. (2006). Quantifying damage , saturation and anisotropy in cracked rocks by inverting elastic wave velocities. *Pure and Applied Geophysics*, *163*, 947–973. https://doi.org/10.1007/s00024-006-0061-y

Snieder, R. (2006). The theory of coda wave interferometry. *Pure and Applied Geophysics*, *163*(2-3), 455–473. https://doi.org/10.1007/s00024-005-0026-6

Snieder, R., Grêt, A., Douma, H., & Scales, J. (2002). Coda wave interferometry for estimating nonlinear behavior in seismic velocity. *Science*, *295*(5563), 2253–2255. https://doi.org/10.1126/science.1070015

Copernicus Climate Change Service. (2023). *Summer 2023: The hottest on record. climate bulletins. implemented by ecmwf as part of the copernicus programme*. https://www.ipcc.ch/report/sixth-assessment-report-working-group-3/

TNO & Ministerie van Economische Zaken. (2020). Groningen gasveld. *NLOG*. https://www.nlog.nl/groningen-gasveld

van Thienen-Visser, K., & Breunese, J. N. (2015). Induced seismicity of the groningen gas field: History and recent developments. *The Leading Edge*, *34*(6), 664–671.

van Thienen-Visser, K., & Fokker, P. A. (2017). The future of subsidence modelling: Compaction and subsidence due to gas depletion of the groningen gas field in the netherlands. *Netherlands Journal of Geosciences*, *96*(5), s105–s116.

Vijlbrief, J.A., Staatssecretaris van Economische Zaken en Klimaat. (2023). Kamerbrief over beëindiging gaswinning Groningenveld. https://www.rijksoverheid.nl/documenten/kamerstukken/2023/09/22/36713903-kamerbrief-beeindiging-gaswinning-groningenveld

Vlek, C. (2019). Rise and reduction of induced earthquakes in the groningen gas field, 1991–2018: Statistical trends, social impacts, and policy change. *Environmental earth sciences*, *78*(3), 59.

Winkler, K., & Nur, A. (1979). Pore fluids and seismic attenuation in rocks. *Geophysical Research Letters*, *6*(1), 1–4. https://doi.org/10.1029/GL006i001p00001

Xie, F., Ren, Y., Zhou, Y., Larose, E., & Baillet, L. (2018). Monitoring local changes in granite rock under biaxial test: a spatiotemporal imaging application with diffuse waves. *Journal of Geophysical Research: Solid Earth*, *123*(3), 2214–2227. https://doi.org/10.1002/2017JB014940

Zhang, H., & Li, C. C. (2019). Effects of confining stress on the post-peak behaviour and fracture angle of fauske marble and iddefjord granite. *Rock Mechanics and Rock Engineering*, *52*(5), 1377–1385. https://doi.org/10.1007/s00603-018-1695-7

Zhubayev, A., Houben, M. E., Smeulders, D. M., & Barnhoorn, A. (2016). Ultrasonic velocity and attenuation anisotropy of shales, Whitby, United Kingdom. *Geophysics*, *81*(1), D45–D56. https://doi.org/10.1190/GEO2015-0211.1

Zotz-Wilson, R. (2020). Coda-wave monitoring of continuously evolving material properties. https://doi.org/https://doi.org/10.4233/uuid:9c0b2f03-040b-4ec8-b669-951c5acf1f3b

Zotz-Wilson, R., Boerrigter, T., & Barnhoorn, A. (2019). Coda-wave monitoring of continuously evolving material properties and the precursory detection of yielding. *The Journal of the Acoustical Society of America*, *145*(2), 1060–1068. https://doi.org/10.1121/1.5091012

2

FORECASTING OF ROCK FAILURE IN THE LABORATORY USING ACTIVE ACOUSTIC MONITORING METHODS

Predicting stress changes in the subsurface leading to failure or seismicity remains challenging. Developing a robust monitoring method can help the prediction and thus mitigation of natural hazards. Ultrasonic transmission experiments were performed on Red Felser sandstones to investigate the forecasting potential to failure at different confining pressures. The forecasting potential for failure of the energy of the direct and coda wave, the transmissivity, Q-factor, coda wave decorrelation coefficient, and velocity change by coda wave interferometry are investigated and compared. Our results show the failure of the tested samples can be forecasted from 40 to 70% of the failure point. Small differences are visible in the precursors between the tested confining pressures, but as the trends are very similar, a robust prediction of failure can be made by combining the various analysis techniques. In this chapter, we propose a traffic light forecasting system using active acoustic monitoring which is applicable for forecasting failure at various depths and or stress conditions, for a better prediction of small stress-induced changes in the subsurface and thus mitigation of failure (and seismicity) in the subsurface.

This chapter has been submitted and is accepted as Veltmeijer, A., Naderloo, M. & Barnhoorn, A. *Forecasting of Rock Failure in the Laboratory using Ultrasonic Monitoring Methods.* Geomechanics and Geophysics for Geo-Energy and Geo-Resources, a pre-print is available at ESS Open Archive. Minor modifications have been applied to keep consistency within this thesis

2.1. INTRODUCTION

Natural hazards, such as earthquakes or landslides, can cause much damage. These events often result from precursory stress changes in the medium or along fault zones. Predicting the degree of these stress changes, and as a result, the potential onset and exact location of failure or seismicity remain very challenging.

Developing a robust method that can monitor these stress changes is crucial for a better prediction and thus mitigation of failure and seismicity in the subsurface. To monitor the physical properties of the subsurface, remotely and non-destructively, geophysical methods can be used. Monitoring the seismic velocities provides insight into mechanical (rigidity, density, etc.) evolution (Schubnel et al., 2006). A number of geomechanical properties influence the propagation of elastic waves through a medium. Structural characteristics, including rock type, mineralogy, porosity, and fluid type, but also environmental characteristics like effective stress (Barnhoorn et al., 2018; Hall, 2009; Sang et al., 2020; Zhubayev et al., 2016), temperature (Snieder et al., 2002), and degree of saturation (Grêt et al., 2006b) change the elastic moduli and thus influence the wave propagation (Hall, 2009). The stress changes can be quantified by analyzing the change in acoustic or seismic velocity (Sang et al., 2020; Xie et al., 2018). Stress changes in the subsurface can cause micro-crack formation. This crack damage can lead to a decrease in elastic wave velocities (Barnhoorn et al., 2018; Sang et al., 2020), shear wave splitting (Crampin & Chastin, 2003; Peacock et al., 1988), and in the development of anisotropy (Schubnel et al., 2006; Zhubayev et al., 2016). However, the sensitivity of seismic wave velocity to stress changes in rocks is low (Barnhoorn et al., 2018; Grêt et al., 2006a, 2006b; Nur, 1971) and detection of temporal variations is therefore difficult (Grêt et al., 2006a; Niu et al., 2003). By analyzing the direct arrivals, dispersion envelope, the coda wave or attenuation (Q-factor), stress changes in the subsurface can also be monitored (Barnhoorn et al., 2018; Grêt et al., 2006b; Hall, 2009; Liu et al., 2022; Sang et al., 2020; Schubnel et al., 2006; Snieder et al., 2006; Xie et al., 2018; Zhubayev et al., 2016).

The coda wave can be used to monitor small changes in a medium, since it scatters throughout the rock and samples a disturbed region more than a direct wave (Snieder, 2006). Therefore, small changes, like micro-crack damage, which may be undetectable in direct waves, are amplified by repeated sampling and detected by the coda. Coda waves are used in many applications, such as monitoring of fault zones (Niu et al., 2008; Poupinet et al., 1984), volcanoes (Grêt et al., 2005; Snieder et al., 2006), the integrity of concrete (Deroo et al., 2010; Niederleithinger et al., 2018), temporal changes in the subsurface and in-situ stress (Grêt et al., 2006a, 2006b), or to monitor velocity changes in laboratory experiments (Hadziioannou et al., 2009; Liu et al., 2022; Sang et al., 2020; Zotz-Wilson et al., 2019) and to locate these (Larose et al., 2010; Planès et al., 2015; Rossetto et al., 2011; Snieder & Vrijlandt, 2005).

So far, laboratory studies on investigating changing rock properties have been unconfined uni-axial compressive strength experiments. Zotz-Wilson et al. (2019) and Liu et al. (2022) showed the use of coda wave interferometry to detect the yield point failure. Sang et al. (2020) did similar work, but also investigated S-waves and concluded that these showed higher sensitivity to structural changes in the rock samples. Barnhoorn et al. (2018), and Zhubayev et al. (2016) showed that attenuation factor Q can be used to describe the start of fracture formation in similar experiments. To investigate the appli-

cability of these properties under confinement, we use S-waves to monitor the structural changes within the evolving medium in triaxial experiments to show both coda wave interferometry and attenuation properties can be used for forecasting the failure of rock samples in the laboratory.

2.2. METHODS

2.2.1. EXPERIMENTAL PROCEDURE

Shear wave propagation is influenced by changes in density and elastic moduli caused by structural changes due to deformation. We show different applications of ultrasonic transmission measurements to monitor the structural changes within a Red Felser sandstone sample. These sandstones are used as an analog for Groningen reservoir rock and the properties of the individual sample are listed in Table 2.1. The porosity was determined to be between 22% and 25%, using a gas expansion (Helium) pycnometer. The samples have a fairly homogeneous composition of 89% quartz, 6% orthoclase (Eradus, 2019) (Figure 2.1h to k). Used are cylindrical core samples with a diameter of 30 ± 0.5 mm and 60 ± 2 mm length, such that the length/diameter ratio is 1:2. A total of 8 uni-axially deformation experiments are performed at different confining pressures ranging from 2.5 to 40 MPa and one UCS experiment (or 0 MPa confining pressure) (Figure 2.1a to g). Simultaneously to the loading of the rock, ultrasonic transmission measurements are done. This combined setup enables us to measure the wave properties under changing stress conditions.

The triaxial experiments are conducted using a Hoek-cel (Figure 2.2) which was placed in a homemade uniaxial loading frame with a 500 kN loadcell. Confining pressure was maintained using an ISCO pump model 100DM. The experiments are performed on vacuum-saturated samples at room temperature. First, the samples are hydrostatically brought up to the confining pressure in steps of 1 MPa. After reaching the desired confining pressure, it is then set constant for the entire experiment. The samples are deformed at a constant strain rate of 0.005 s^{-1}. The shortening of the sample is recorded with two Solartron AX/1/S linear variable displacement transducers (LVDT's) and is corrected for

Table 2.1: Summary of the Red Felser samples, confining pressure P_c, porosity ϕ, length L, diameter D, and Young's Modulus E, which is calculated from the stress-strain relationship. All samples were water-saturated.

Sample	P_c [MPa]	ϕ [%]	L [mm]	D [mm]	E [GPa]
RF610	0	23.35	60.30	29.75	8.60
RF613	2.5	23.48	60.25	29.65	9.79
RF28	5	23.44	60.60	29.65	10.83
RF23	10	24.94	61.70	29.65	12.44
RF68	20	23.82	61.65	29.65	15.94
RF614	20	22.72	60.40	29.55	13.39
RF69	40	22.20	60.35	29.70	13.74
RF615	40	23.25	60.55	29.75	13.44
AL ref	10 & 20	0	60	30	75

machine deformation. The axial stress was measured using a load cell positioned above the sample (Figure 2.2).

The ultrasonic transmission measurements are performed using two S-wave transducers, with a peak operating frequency of 1 MHz. An Agilent 33210A waveform generator generated the waveforms which were amplified by an RF Power amplifier, sent and received using Olympus 1MHz/.5" v153 transducers, and finally recorded using a Yokogawa DL9240L oscilloscope. The two axial transducers are integrated into the pistons in the loading system with a source at the top and receiver at the bottom, such that the polarization of the shear source and receiver transducers was always aligned. The ultrasonic transmission signals are recorded every 10 seconds for 100 μs and are a stack of 256 (S-) waves to increase the signal-to-noise ratio. The ultrasonic transmission monitoring started immediately after starting the deformation and continued during the whole duration of the deformation experiment.

2.2.2. DATA ANALYSIS

To monitor the onset and development of fracturing within the rock the coda wave and the attenuation of the recorded waves are investigated. The coda wave is used to monitor the change in scattering properties, while the Q-factor, energy, and transmissivity are all a proxy of attenuation. Coda Wave Interferometry (CWI) is used to monitor the velocity change between two recorded waves. Comparing the consecutive wavefields is done with a cross-correlation (CC) (Figure 2.3), for a time window of width $2t_w$ and centered around time t_k, and reaches its maximum if the travel time perturbation δt across all

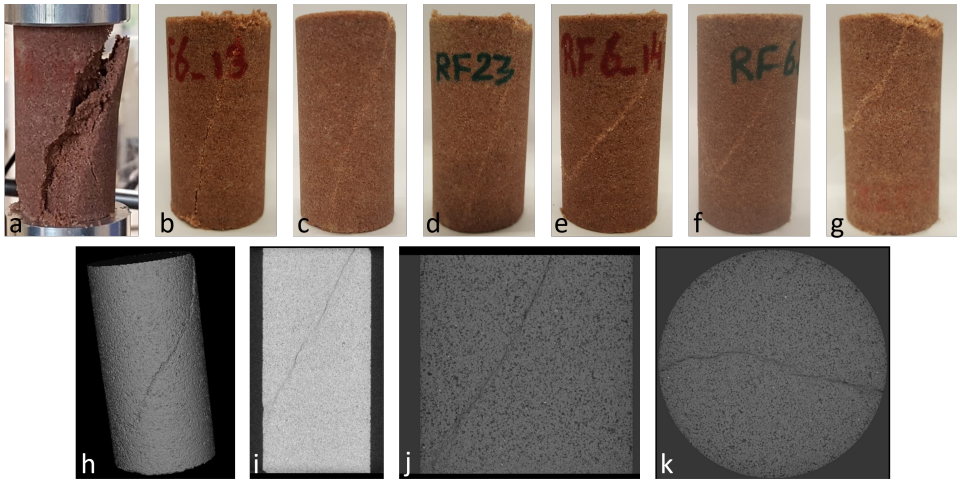

Figure 2.1: Pictures of the fractured rock samples in a to g, from left to right fractured with 0 to 40 MPa confining pressure. In a. sample RF610, b. sample RF613, c. RF28, d. RF23, e. RF14, f. sample RF68, g. sample RF69. CT images of sample RF614 in h to k made by CoreTOM microCT scanner in h a volume representation of the sample with a resolution of 73.7 µm and in i YZ slice with a resolution of 73.7 µm. j and k show a higher resolution zoom on the fracture and the grains in the sample with a resolution of 12.2 µm. In j a YZ slice, and in k a XY slice.

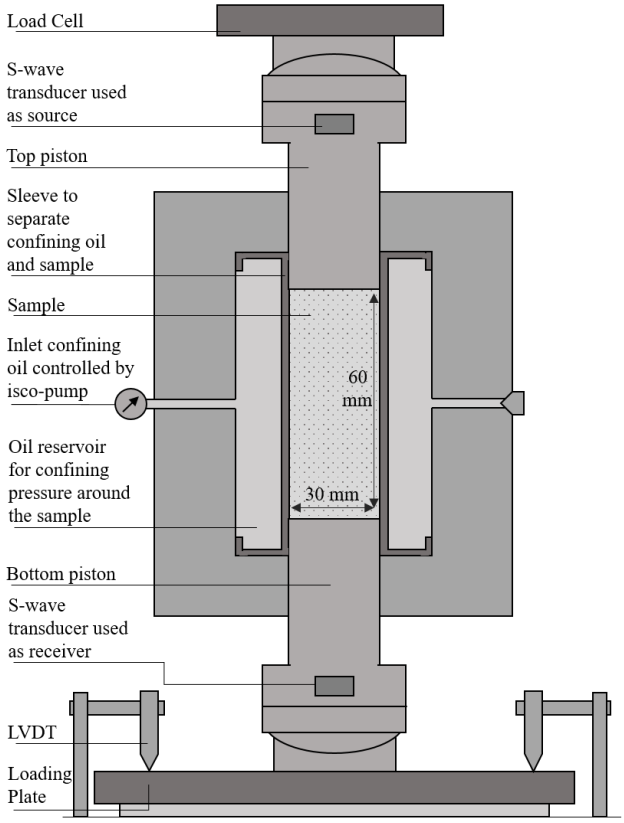

Figure 2.2: Schematic illustration of instrumented Hoek cell with S-wave transducers integrated into the pistons (not to scale). The shortening of the sample was recorded with two linear variable displacement transducers (LVDT's), which record the total (vertical) movement of the loading plate. The axial stress was measured using a load cell.

possible perturbed paths P is $\delta t = t_s$. Assuming the time shift is constant in the considered time window, the relative velocity change (dv/v) can be written as $\delta v/v = -\delta t/t$.

In addition to the velocity change, the decorrelation coefficient is determined to investigate the changes in material scattering (Planès et al., 2014, 2015). The method of Coda Wave Decorrelation (CWD) introduced by (Larose et al., 2010) is based on the theory of (Snieder, 2006). The decorrelation coefficient K between the perturbed (u_p) and unperturbed wavefield (u_u), also described in (Zotz-Wilson et al., 2019), is formulated as

$$K(t_s) = 1 - CC(t_s) = 1 - \frac{\int_{t_k-t_w}^{t_k+t_w} u_{p_j-N}(t)u_{p_j}(t+t_s)dt}{\sqrt{\int_{t_k-t_w}^{t_k+t_w} u_{p_j-N}^2(t)dt \int_{t_k-t_w}^{t_k+t_w} u_{p_j}^2(t)dt}}. \tag{2.1}$$

To monitor the changing medium, a moving reference wavefield $u_{(p_j-N)}(t)$ is used, where N is the number of measurements the reference wavefield is lagging behind the to-be correlated wavefield $u_{p_j}(t)$ (Figure 2.3B). While the coda waves seem random due to the complex paths they take through the medium, the changes they are subjected to are

strongly related to the position and strength of the changes in the medium (Planès et al., 2014). K is related to the changes in material scattering due to the addition of scatterers (Planès et al., 2014, 2015), such as the addition or removal of fractures. The scattering in a medium along the transport mean free path l can be described using the cross-sectional area of a single scatterer V_a and the density of scatterers ρ (Planès et al., 2014). The total scattering coefficient as described by (Aki & Chouet, 1975) is given by $g_0 = \rho V_a = l^{-1}$. Following the theory in (Aki & Chouet, 1975), we can rewrite the coda decorrelation in terms of the scattering coefficient (g_0) between a perturbed (p) and unperturbed (u) medium (Zotz-Wilson, 2020).

$$K(t) = \frac{v_0}{2} t |\Delta g_{0_{p-u}}|, \tag{2.2}$$

where $K(t)$ is the theoretical decorrelation coefficient, t the time in the coda and v_0 the velocity in the medium. Using a shifting reference, the changes in the absolute value of $|g_0|$ are monitored as a rate of change (Zotz-Wilson, 2020). In these deformation experiments, the change in scattering is mostly attributed to the closure or formation and growth of micro-fractures. Closure of pre-existing pore space (such as micro-fractures) and compaction of the medium cause a reduction in the scattering cross-sectional area and thus a reduction in K. During compaction and closure of pre-existing pore space, the attenuation is expected to decrease, and energy and transmissivity to increase. The formation of micro-fractures, leading to failure, results in an increase in the total scattering cross-section σ and the number density of scatterers ρ, both contributing to an increase of the total scattering coefficient.

The formation and growth of micro-fractures increase the attenuation and cause the waves to lose energy and increased arrival time. The ultrasonic attenuation is determined using the laboratory method by (Toksoz et al., 1979) also described in (Barnhoorn et al., 2018; Zhubayev et al., 2016) by comparing the rock sample to an aluminium reference. Assuming a constant Q, the spectral ratio is written as

$$\ln \frac{A_1}{A_2} = (\beta_2 - \beta_1) x f + \ln \frac{G_1}{G_2}, \tag{2.3}$$

where A_i is the Fourier amplitude, f is the frequency, x is the propagation distance and G_i is a scaling factor for spherical spreading independent of frequency. $i = 1$ refers to the aluminium reference and 2 to the rock sample. β_i is related to the quality factor by

$$Q_i = \frac{\pi}{\beta_i v}, \tag{2.4}$$

where v is the P- or S- velocity. β_1 is very small compared to β_2, due to the very low attenuation of the aluminium and is henceforth ignored. The energy of waves can be a good method for crack monitoring (Mi et al., 2006; Michaels et al., 2005) and is approximated as $E(\sigma) = \int_{t_2}^{t_1} u^2(t;\sigma) dt$, where $u(t;\sigma)$is the recorded waveform (Khazaei et al., 2015; Mi et al., 2006; Michaels et al., 2005; Sagar, 2009). The transmitted wave amplitudes are defined as $T = |A_{max}|$ (Shreedharan et al., 2021), which is the maximum amplitude of the recorded S-wave (Figure 2.3A).

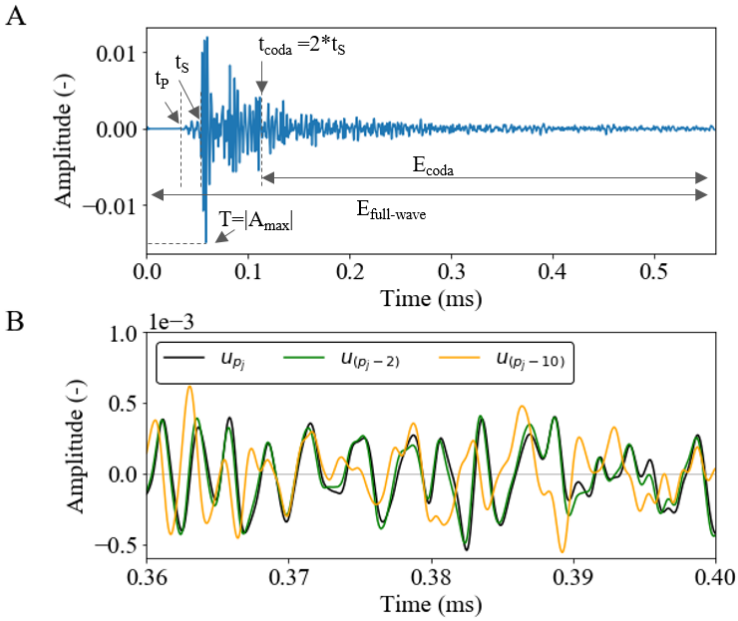

Figure 2.3: Showing recorded transmission wavelets.A showing the arrival times of P-wave (t_P), S-wave (t_S), and the start of the coda (t_{coda}). The range used for the energy calculation is indicated for the energy of the total- and coda wave as well as the maximum amplitude for the transmissivity. B shows a part of the coda of three wavelets. Where u_{p_j} is the to-be correlated wavefield and is lagging behind the reference wavefield by N=2 and N=10.

2.3. RESULTS

The deformation of rock samples in the laboratory is commonly characterized into 5 stages: crack closure, the elastic stage, stable crack growth, unstable cracking, and rock failure (Bieniawski, 1967; Eberhardt et al., 1999; Zhou et al., 2018). The stress-strain curves obtained by triaxial testing at the defined confining pressures (Figure 2.4A) show a non-linear increase at low stresses caused by the initial setting of the machine, elastic compaction of the rock, and closure of existing pore space e.g. the closure of micro-cracks pre-existing in the sample (Bieniawski, 1967; Eberhardt et al., 1999; Walsh, 1965; Zhou et al., 2018). This is followed by an elastic (reversible) deformation stage, where a linear stiffening of the rock matrix is expected, visible as a constant gradient in the stress-strain curves. After the elastic stage, the stress-strain curve shows non-linear behaviour, indicating the formation of the first micro-fractures (Barnhoorn et al., 2010). The crack formation continues until the stresses drop drastically, indicating the failure of the sample. Increasing the confining pressure leads to an expected increase in the maximum strength and Young's modulus of the sample.

During the deformation of the sample, ultrasonic transmission measurements were performed (Figure 2.5). Coda wave decorrelation (CWD) was used to monitor structural and velocity changes in the medium (Figure 2.4C,D), following the results of Zotz-Wilson

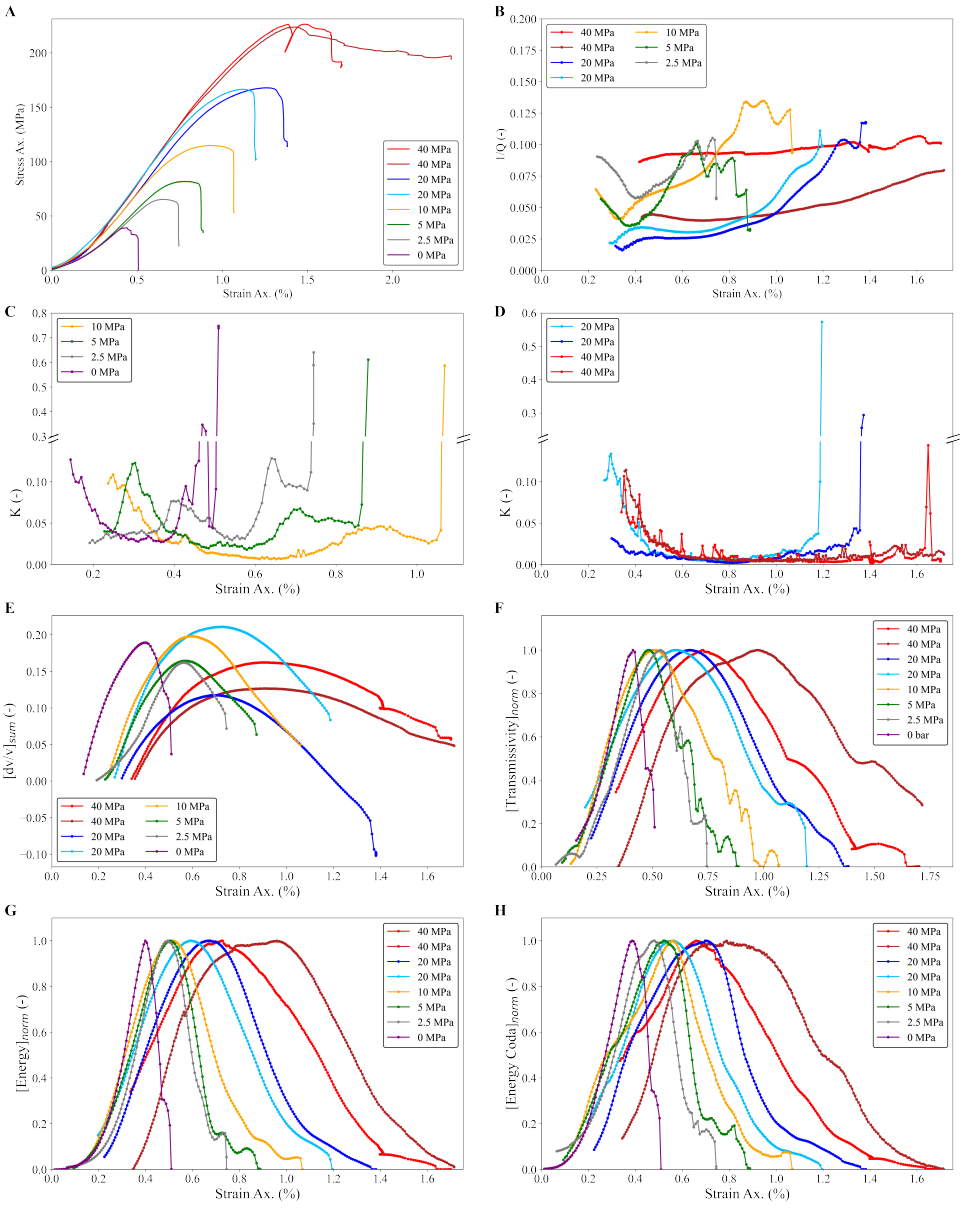

Figure 2.4: The stress - strain, and seismic parameters during deformation experiment for all confining pressures. A showing the stress-strain relations. B showing the evolution of the attenuation 1/Q during deformation. C and D show the evolution of the decorrelation coefficient K for the lower and higher confining pressures. E shows the cumulative velocity change $[dv/v]_{sum}$. F shows the evolution of the transmissivity T, normalized to the maximum of each experiment for better comparison. G and H show the energy of the full wave E_T and energy of the coda E_C, respectively. The values of each are normalized to their max for better comparison.

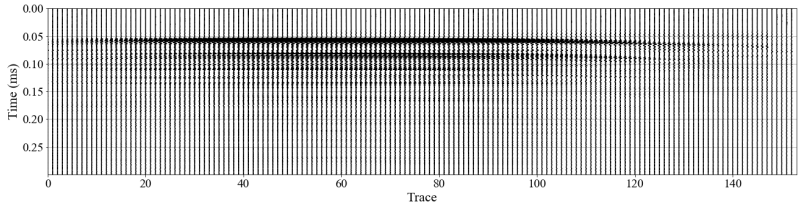

Figure 2.5: First 0.25ms of all the recorded S-waves during the uni-axial 10 MPa confining pressure compression experiment. The waveforms are recorded every 10 seconds and are a stack of 256 S-waves.

et al., 2019. K shows an average of 10 independent correlation windows (2.7I,J), with the first starting at twice the S-arrival time ($t_{coda} = 2 * t_S$) (Fehler et al., 1992; Pujades et al., 1997), in total the coda windows span 0.84ms. Using a shifting reference, the decorrelation coefficient K is a measure of change in the absolute value of $|g_0|$, therefore, a decreasing trend indicates a reduction in the scattering of the waveform compared to its previous. A reduction is visible at the start of the experiments for each tested confining pressure (Figure 2.4C,D). This reduction is followed by a plateau of limited change in K, with thereafter an increase indicating an increasing scattering coefficient, during the deformation stage of formation and growth of (micro-) fractures.

Additionally to K, the velocity change during the experiment was determined using coda wave interferometry (CWI). The CWI, using a shifting reference, gives the rate of change in velocity, by cumulative summation of the average relative velocity change, the velocity change during the experiment is obtained (Figure 2.4E). This shows a parabolic trend indicating the compaction and formation and growth of (micro-) fractures during the experiments. Similar parabolic trends can be seen in the energy and transmissivity data (Figure 2.4F,G,H)., where the initial increase can be explained by the compaction of the rock matrix and the following decrease by the formation of micro-fractures (Shah & Hirose, 2010; Zotz-Wilson, 2020; Zotz-Wilson et al., 2019). Additional to the energy and transmissivity, the evolution of the ultrasonic attenuation (Figure 2.4B) and frequency content of the waveforms provide insight into the deformation of the sandstones.

The energy of waves can be attenuated by fractures in the rock sample. Changes in the ultrasonic transmission waveforms are detected when the attenuation effects due to fracture formation are larger than the compaction and shortening effects due to loading. During loading, the samples are subjected to a constant strain rate. This results in shortening and compaction and causes a shorter direct travel path, as well as a faster path, due to increased velocity, for the transmitted waves. Together with the closure of pre-existing pore-space in the rock matrix these result in an increase in energy, transmissivity, and relative velocity (Figure 2.4E to H). The fractures induced by this continued deformation reverse this effect, decreasing the velocity of the matrix and increasing attenuation causing the waves to lose energy and arrive at an increased arrival time. The competition between these factors results in the parabolic trends of transmissivity, velocity change, and energy. The vertex of these parabolas, the change from an increasing to decreasing trend, is around the point the gradient of the stress-strain curve changes to non-linearity and shows the first indication of (micro-) fracture formation and growth. Within these parabolic trends, a more complex pattern in the S-wave am-

plitudes emerges around the peak stress, for the lower confining pressures. This pattern is also visible in the evolution of the Q-factor (attenuation) (Figure 2.4B), which is inversely related to the energy and transmissivity of the S-waves. The frequency content of the recorded wave changed during the experiment(Figure 2.7G,H). The normalized amplitude spectra of the frequency show a shift towards the lower frequencies, due to the increased presence of micro-fractures. Upon failure the high frequencies are mostly attenuated and the lower persevere.

2.4. DISCUSSION

2.4.1. ULTRASONIC MONITORING AND FORECASTING FAILURE

The first sign of permanent deformation, namely the formation of (micro-) fractures resulting ultimately in the failure of the sample, is the change to non-linearity in the slope of the stress-strain relation. However, this stress-strain relation is impossible to determine in-situ (i.e. landslides, earthquakes, etc.). To detect deformation without stress and/or strain measurements, we focused on the change in seismic response throughout deformation, using the advantage that active source methods do not rely on acoustic emission to detect any deformation, and thus can be used to monitor both aseismic and seismic deformation. The attenuation and scattering properties of the waves change due to the formation and growth of the (micro-) fractures in the samples.

Precursors to failure were determined from these waveform attributes. The evolution of the energy E, relative velocity change dv/v, and transmissivity T show a clear change in slope as the fractures formed are detected (Figure 2.4E to H). The decorrelation coefficient K shows an increase in scattering when the fractures are formed and detected by the coda (Figure 2.4C,D). Therefore, the minimum before this increasing trend in the K, and the peaks of E, dv/v, and T are used as the earliest precursor to the imminent failure of the sample. The occurrence of these precursors is plotted relative to the failure of the sample, where at 100% failure occurs according to the stress-strain relation (Figure 2.6). For the uniaxial compressive strength (UCS) experiments, the precursors obtained from coda wave decorrelation (CWD) are significantly earlier than the precursors based on attenuation properties. They range from 65% to 72% for K and dv/v and between 84% to 88% for the attenuation parameters E and T. This changes with increasing confining pressure, where the precursors based on attenuation are generally earlier. Which of the precursors to failure is the first varies and comes as early as 40% of failure for 40 MPa confining pressure. At higher confining pressures, the precursors are relatively earlier but also show a bigger spread.

To forecast the upcoming failure of the sample, we deployed a traffic light warning system (TLS) based on the interpretation of the processed waveform data and the occurrence of the precursors (Figure 2.7).

1. According to our traffic light, it is green or safe when our sample is far from its failure. The closure of pre-existing pore space, stiffening, and compaction of the rock is indicated by a decrease in scattering K, and an increase in the E, T, and $[\mathrm{dv/v}]_{sum}$.

2. The orange stage can be classified as a stage of higher alert in which failure of the sample is expected, and be used to forecast the upcoming failure. This stage starts

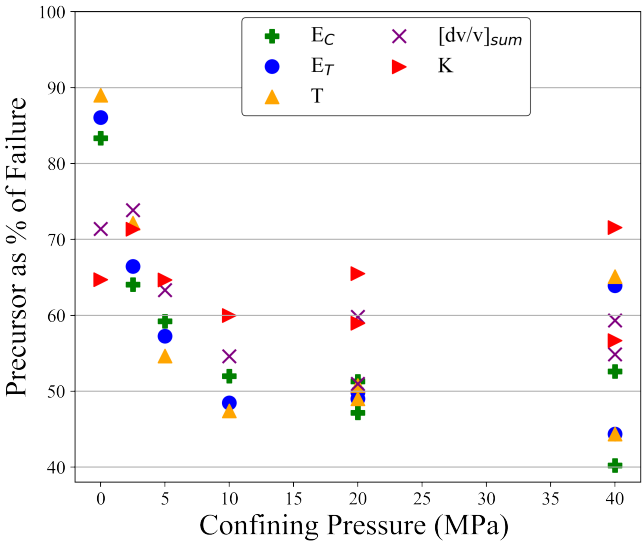

Figure 2.6: Appearance of the peak in the energy of the full wave E_T and coda wave E_C, the cumulative velocity change $[dv/v]_{sum}$, and the transmissivity T, as well as the minimum of the decorrelation coefficient K as precursor relative to the failure of the sample.

at the first occurrence of precursors of the waveform attributes. In Figure 2.7, E, $[\mathrm{dv/v}]_{sum}$, and T change to a decreasing trend indicating the attenuation effect due to newly formed (micro-) fractures is stronger than the continued compaction and shortening of the sample. This is at around 50% of the final failure point of the sample (Figure 2.6).

3. The last stage represents that failure is imminent. The warning stage starts when K shows an increase in scattering, giving a clear indication (micro-) fractures are formed. A clear indication of fracture formation and thus upcoming failure is present when the energies, transmissivity, and relative velocity change show a decreasing trend and the decorrelation coefficient starts to increase. Additionally, the frequency content of the recorded wave shifts towards the lower frequencies as the higher frequencies are attenuated, due to the increased formation and growth of (micro-) fractures.

From experiment to experiment, the first precursor varies (Figure 2.6), but for forecasting purposes, not one precursory signal is superior over the other. By combining the various analysis techniques on a single wavelet, the impact of the sensitivity of a single parameter is limited and a more robust TLS forecast can be made. Even though precursory signals vary for confining pressure, the results show that the trend in the processed data of the S-waves is very similar for all tested confining pressures. It is, therefore, suggested that these techniques could be deployed for monitoring the failure of rocks, at any depth or pressure condition. Monitoring is possible at any arbitrary point in time or stress condition, using a shifting reference, and by using the traffic light system, the fre-

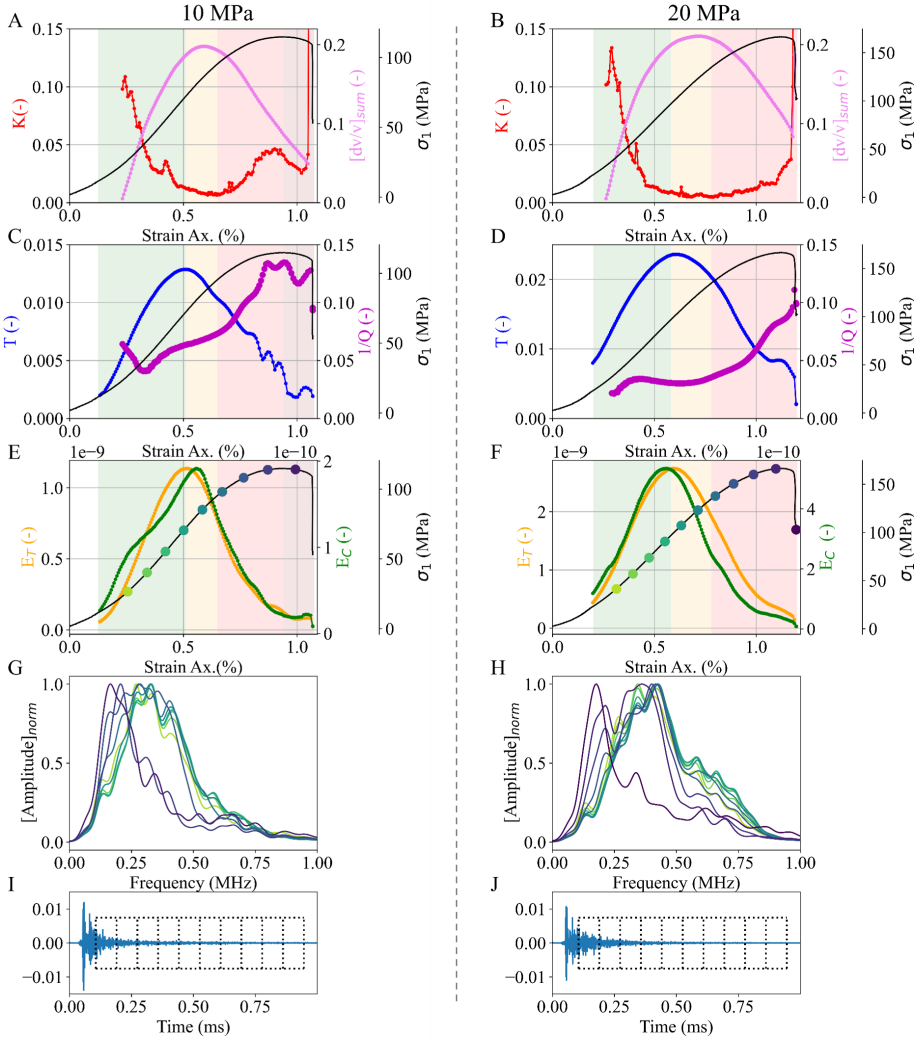

Figure 2.7: Precursory signals during the deformation in A-E at 10 (left column) and in F-J at 20 MPa (right column) confining pressure. Showing the cumulative velocity change from CWI dv/v$_{sum}$ and decorrelation coefficient K in A, F, the attenuation 1/Q and transmissivity T in B, G, and the energy of the full wave E_T and coda wave E_C in C, H together with the stress-strain relation. D, I showing the changing frequency content of the recorded waves during deformation.D and I show the stage of deformation of the frequency content plotted, corresponding to the colours of the dots in C and H. E and J show a recorded waveform during deformation, the 10 decorrelation windows are visualized, with the first starting at 2 times the S-arrival time ($t_{coda} = 2 * t_S$), and a total length of 0.84ms. The coloured zones in A-C and F-H show the three stages of the traffic light warning system (TLS).

quency of measurements can be increased near failure to obtain an even more accurate forecast.

The precursors we showed in this chapter, could be used to forecast failure at approximately 70% of the failure point. In a laboratory setting, this might be seconds or minutes, at the field scale, this could be hours, days or longer, which can provide time for mitigation measures. The application and scalability of ultrasonic monitoring from laboratory to field scale will have to be researched. However, research has shown precursory signals could be measured at a field scale. Niu et al., 2008, showed stress-induced changes in crack properties during co-seismic slip using active source cross-well experiment at the San Andreas Fault or Chiarabba et al., 2020, showed a local P-wave velocity reduction near the hypocentre for a few weeks before the mainshock using seismic tomography at the fault zone which participated in the 2016 M6.5 Norcia earthquake, Italy.

2.4.2. EFFECT OF PRESSURE

The competition between the attenuation and scattering effect of fracture formation and compaction and shortening of the sample results in a clear precursory signal for all tested confining pressures. The difference between confining pressures tested, for our purpose of forecasting failure, is of lesser importance but gives us some more insight into the process of deformation and sensitivity of the used S-waves in the detection of micro-fractures.

DEFORMATION RATE

The experiments are all performed with a loading rate of $0.005s^{-1}$, at high confining pressure, larger stresses are needed to achieve failure of the sample. As a result, these rock samples have a lengthier elastic stage and a slower fracture formation. Due to the (relative) slower deformation at high pressure, relatively more waveforms are recorded per deformation stage. Consequently, less change in the scattering in the medium from waveform to reference waveform is detected.

This also implies that, at higher confining pressures, the deformation is better monitored than at low confining pressures, as a constant sampling rate of 10 sec was used. Therefore, the deformation at 40 MPa confining pressure was sampled best. During the deformation, K shows several sharp peaks showing rapid, but short changes in the sample (Figure 2.4D). From the nature of the shifting reference, these peaks can be interpreted as the change from the signal before. Crack formation increases the amount of scattering, thus K. If, at the sampling time, no new crack is formed, no additional scattering is created, thus K goes down again. Hence, we interpret these peaks at the start of the experiment as the sharp closure of larger or a couple of pre-existing fractures present in the rock sample. During a later stage of deformation, these peaks indicate the formation of micro-cracks, large enough to be sampled by the ultrasonic waves and frequency used. When deformation is fast, crack formation follows each other in quick succession, resulting in an increase in scattering and K, without individual crack formation visible. This implies that for slow deformation and a high sampling rate, the separate crack formation can be monitored, contingent on wave sensitivity.

This relative deformation speed is also clearly visible in the velocity change during deformation, when plotted cumulative to represent the absolute velocity change the

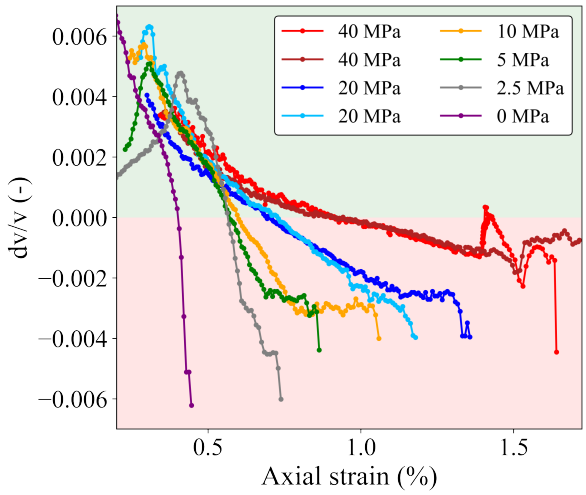

Figure 2.8: The rate of velocity change dv/v during deformation for each confining pressure tested. Showing the relative deformation rate changes with confining pressure.

graphs differ from pressure to pressure, however when we plot the rate of the velocity change, it decreases with confining pressure, showing a slower rate of deformation at higher pressure (Figure 2.8).

DEFORMATION AROUND PEAK STRENGTH

The difference in deformation due to confining pressure is also visible in the maxima of the waveform attributes (Figure 2.9). At higher pressures fractures form with small or closed apertures causing less additional scattering and attenuation opposed to open tensile fractures. The maximum value of K obtained during the failure of the sample shows a decreasing trend with increasing pressure. Opposite, the maximum energy and transmissivity measured increase with confining pressure. The source wavelet for all experiments remained constant, due to increased compaction more of the initial wave energy is preserved at higher initial confining stresses. A reduced scattering effect of the shear compared to tensile fractures results in decreasing values of K. This implies that tensile fractures or fractures with a bigger aperture are better detected, due to the higher scattering nature of the tensile fracture.

Near the failure point of the stressed rock samples, the formed micro-fractures start to connect and form larger-scale shear fractures. At lower confining pressures, a more complex pattern in the transmissivity emerges around the peak stress (Figure 2.4B,F to H). The attenuation (inverse Q-factor), energy, and transmissivity for the lower confining pressures oscillate. We suggest this oscillating behaviour observed in our data, is the detection of the connecting shear fractures near failure. The transmissivity and energy increase due to the continued shortening and compaction of the sample. The moment the fractures are formed and connected into larger ones, the attenuation increases, and the energies and transmissivity drop. While the sample is not failing yet and is still shortened

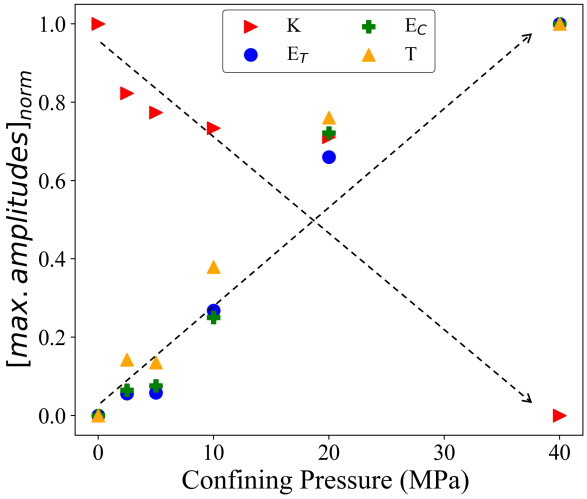

Figure 2.9: The maximum value recorded for each precursor. Showing decreasing trend with pressure in decorrelation coefficient K, and an increasing trend in the energy of the full wave E_T and coda wave E_C, and transmissivity T.

and compacted, the formed fractures (partially) close and the attenuation decreases until the next local failure forms the next larger fracture, resulting in the observed oscillations. This oscillation is only visible when the sample shows less brittle behaviour; when the sample collapses at or very close to peak strength this oscillation is not observed suggesting all the micro-fractures connect rapidly in one large shear fracture. At higher confining pressure the potential to form fractures with aperture is very small, therefore we state that this oscillation is not present due to the lack of sensitivity of the waves and less brittle behaviour of the samples at higher pressures.

2.5. CONCLUSION

Ultrasonic experiments have been conducted on Red Felser sandstones (analog to the Groningen reservoir rock) to investigate the potential of shear wave transmission measurements in forecasting the upcoming failure. Ultrasonic monitoring can monitor the changes in the subsurface, while passive acoustic emission methods could be late in detecting the upcoming failure. Our results show the failure of the tested samples can be forecasted from 40 to 70% of the failure point. A robust prediction can be made by combining the various analysis techniques, without having to do multiple measurements. Which precursor to failure first varies, and comes as early as 40% of failure at high pressure, but for forecasting purposes, not one precursory signal is superior over the other.

In this study, the stress-strain relations were available, therefore the small details in the waveforms could be explained by relating the signals to the deformation stages of the stress-strain relation. The precursors show small differences between tested confining pressures, but as the trends are very similar, we argue that the proposed traffic light forecasting system is applicable for forecasting failure at various depths and or stress condi-

tions. Monitoring can be started at any arbitrary point in time or stress condition using a shifting reference. For field measurements, additional research and feasibility studies will have to be performed, but the shown monitoring methods in this chapter can be applicable in field situations when stress-strain measurements are not possible. Contributing to a robust monitoring technique that can detect small stress-induced changes in the subsurface and use these for a better prediction and thus mitigation of failure (and seismicity) in the subsurface.

REFERENCES

Aki, K., & Chouet, B. (1975). Origin of coda waves: Source, attenuation, and scattering effects. *Journal of Geophysical Research*, *80*(23), 3322–3342. https://doi.org/10.1029/jb080i023p03322

Barnhoorn, A., Cox, S. F., Robinson, D. J., & Senden, T. (2010). Stress- and fluid-driven failure during fracture array growth: Implications for coupled deformation and fluid flow in the crust. *Geology*, *38*(9), 779–782. https://doi.org/10.1130/G31010.1

Barnhoorn, A., Verheij, J., Frehner, M., Zhubayev, A., & Houben, M. (2018). Experimental identification of the transition from elasticity to inelasticity from ultrasonic attenuation analyses. *Geophysics*, *83*(4), MR221–MR229. https://doi.org/10.1190/geo2017-0534.1

Bieniawski, Z. T. (1967). Mechanism of brittle fracture of rock. Part I-theory of the fracture process. *International Journal of Rock Mechanics and Mining Sciences and*, *4*(4). https://doi.org/10.1016/0148-9062(67)90030-7

Chiarabba, C., De Gori, P., Segou, M., & Cattaneo, M. (2020). Seismic velocity precursors to the 2016 Mw 6.5 Norcia (Italy) earthquake. *Geology*, *48*(9), 924–928. https://doi.org/10.1130/G47048.1

Crampin, S., & Chastin, S. (2003). A review of shear wave splitting in the crack-critical crust. *Geophysical Journal International*, *155*(1), 221–240. https://doi.org/10.1046/j.1365-246X.2003.02037.x

Deroo, F., Kim, J.-Y., Qu, J., Sabra, K., & Jacobs, L. J. (2010). Detection of damage in concrete using diffuse ultrasound. *The Journal of the Acoustical Society of America*, *127*(6), 3315–3318. https://doi.org/10.1121/1.3409480

Eberhardt, E., Stead, D., & Stimpson, B. (1999). Quantifying progressive pre-peak brittle fracture damage in rock during uniaxial compression. *International Journal of Rock Mechanics and Mining Sciences*, *36*(3), 361–380. https://doi.org/10.1016/S0148-9062(99)00019-4

Eradus, D. (2019). *Petrographical description and petrophysical measurements on the red felser sandstone* [BSc Thesis]. Delft University of Technology.

Fehler, M., Hoshiba, M., Sato, H., & Obara, K. (1992). Separation of scattering and intrinsic attenuation for the Kanto-Tokai region, Japan, using measurements of S-wave energy versus hypocentral distance. *Geophysical Journal International*, *108*(3), 787–800. https://doi.org/10.1111/j.1365-246X.1992.tb03470.x

Grêt, A., Snieder, R., Aster, R. C., & Kyle, P. R. (2005). Monitoring rapid temporal change in a volcano with coda wave interferometry. *Geophysical Research Letters*, *32*(6), 1–4. https://doi.org/10.1029/2004GL021143

Grêt, A., Snieder, R., & Özbay, U. (2006a). Monitoring in situ stress changes in a mining environment with coda wave interferometry. *Geophysical Journal International*, *167*(2), 504–508. https://doi.org/10.1111/j.1365-246X.2006.03097.x

Grêt, A., Snieder, R., & Scales, J. (2006b). Time-lapse monitoring of rock properties with coda wave interferometry. *Journal of Geophysical Research: Solid Earth*, *111*(3), 1–11. https://doi.org/10.1029/2004JB003354

Hadziioannou, C., Larose, E., Coutant, O., Roux, P., & Campillo, M. (2009). Stability of monitoring weak changes in multiply scattering media with ambient noise correlation: Laboratory experiments. *The Journal of the Acoustical Society of America*, *125*(6), 3688–3695. https://doi.org/10.1121/1.3125345

Hall, S. A. (2009). *When geophysics met geomechanics: Imaging of geomechanical properties and processes using elastic waves* (D. Kolymbas & G. Viggiani, Eds.; VIII). Springer. https://doi.org/10.1007/978-3-642-03578-4

Khazaei, C., Hazzard, J., & Chalaturnyk, R. (2015). Damage quantification of intact rocks using acoustic emission energies recorded during uniaxial compression test and discrete element modeling. *Computers and Geotechnics*, *67*, 94–102. https://doi.org/10.1016/j.compgeo.2015.02.012

Larose, E., Planes, T., Rossetto, V., & Margerin, L. (2010). Locating a small change in a multiple scattering environment. *Applied Physics Letters*, *96*(20), 1–4. https://doi.org/10.1063/1.3431269

Liu, S., Ma, B., Ma, Z., Sun, J., ang Wang, Q., & Liu, K. (2022). Evaluation of the compressional damage evolution of ancient fired clay bricks using coda wave analysis. *Journal of Building Engineering*, *49*(November 2021), 104071. https://doi.org/10.1016/j.jobe.2022.104071

Mi, B., Michaels, J. E., & Michaels, T. E. (2006). An ultrasonic method for dynamic monitoring of fatigue crack initiation and growth. *The Journal of the Acoustical Society of America*, *119*(1), 74–85. https://doi.org/10.1121/1.2139647

Michaels, J. E., Michaels, T. E., Mi, B., Cobb, A. C., & Stobbe, D. M. (2005). Self-calibrating ultrasonic methods for in-situ monitoring of fatigue crack progression. *AIP Conference Proceedings*, *760*(2005), 1765–1772. https://doi.org/10.1063/1.1916884

Niederleithinger, E., Wang, X., Herbrand, M., & Müller, M. (2018). Processing ultrasonic data by coda wave interferometry to monitor load tests of concrete beams. *Sensors (Switzerland)*, *18*(6). https://doi.org/10.3390/s18061971

Niu, F., Silver, P. G., Daley, T. M., Cheng, X., & Majer, E. L. (2008). Preseismic velocity changes observed from active source monitoring at the Parkfield SAFOD drill site. *Nature*, *454*(7201), 204–208. https://doi.org/10.1038/nature07111

Niu, F., Silver, P. G., Nadeau, R. M., & McEvilly, T. V. (2003). Migration of seismic scatterers associated with the 1993 Parkfield aseismic transient event. *Nature*, *426*(6966), 544–548. https://doi.org/10.1038/nature02151

Nur, A. (1971). Effects of stress on velocity anisotropy in rocks with cracks. *J Geophys Res*, *76*(8), 2022–2034. https://doi.org/10.1029/jb076i008p02022

Peacock, S., Crampin, S., Booth, D. C., & Fletcher, J. B. (1988). Shear wave splitting in the Anza Seismic Gap, southern california: Temporal variations as possible precursors. *Journal of Geophysical Research: Solid Earth*, *93*(B4), 3339–3356. https://doi.org/10.1029/JB093iB04p03339

Planès, T., Larose, E., Margerin, L., Rossetto, V., & Sens-Schönfelder, C. (2014). Decorrelation and phase-shift of coda waves induced by local changes: Multiple scattering approach and numerical validation. *Waves in Random and Complex Media*, *24*(2), 99–125. https://doi.org/10.1080/17455030.2014.880821

Planès, T., Larose, E., Rossetto, V., & Margerin, L. (2015). Imaging multiple local changes in heterogeneous media with diffuse waves. *The Journal of the Acoustical Society of America*, *137*(2), 660–667. https://doi.org/10.1121/1.4906824

Poupinet, G., Ellsworth, W. L., & Frechet, J. (1984). Monitoring velocity variations in the crust using earthquake doublets: an application to the Calaveras fault, California (USA). *Journal of Geophysical Research*, *89*(B7), 5719–5731. https://doi.org/10.1029/JB089iB07p05719

Pujades, L., Ugalde, A., Canas, J. A., Navarro, M., Badal, F. J., & Corchete, V. (1997). Intrinsic and scattering attenuation from observed seismic codas in the Almeria Basin (southeastern Iberian Peninsula). *Geophysical Journal International*, *129*, 281–291. https://doi.org/10.1016/j.pepi.2004.02.004

Rossetto, V., Margerin, L., Planès, T., & Larose, É. (2011). Locating a weak change using diffuse waves: Theoretical approach and inversion procedure. *Journal of Applied Physics*, *109*(3). https://doi.org/10.1063/1.3544503

Sagar, R. V. (2009). An experimental study on acoustic emission energy and fracture energy of concrete. *Proceedings of the National Seminar & Exhibition on Non-Destructive Evaluation*, 225–228.

Sang, G., Liu, S., & Elsworth, D. (2020). Quantifying fatigue-damage and failure-precursors using ultrasonic coda wave interferometry. *International Journal of Rock Mechanics and Mining Sciences*, *131*(February), 104366. https://doi.org/10.1016/j.ijrmms.2020.104366

Schubnel, A., Benson, P. M., Thompson, B. D., Hazzard, J. F., & Paul Young, R. (2006). Quantifying damage , saturation and anisotropy in cracked rocks by inverting elastic wave velocities. *Pure and Applied Geophysics*, *163*, 947–973. https://doi.org/10.1007/s00024-006-0061-y

Shah, A. A., & Hirose, S. (2010). Nonlinear ultrasonic investigation of concrete damaged under uniaxial compression step loading. *Journal of Materials in Civil Engineering*, *22*(5), 476–484. https://doi.org/10.1061/(asce)mt.1943-5533.0000050

Shreedharan, S., Bolton, D. C., Rivière, J., & Marone, C. (2021). Competition between preslip and deviatoric stress modulates precursors for laboratory earthquakes. *Earth and Planetary Science Letters*, *553*, 116623. https://doi.org/10.1016/j.epsl.2020.116623

Snieder, R. (2006). The theory of coda wave interferometry. *Pure and Applied Geophysics*, *163*(2-3), 455–473. https://doi.org/10.1007/s00024-005-0026-6

Snieder, R., Grêt, A., Douma, H., & Scales, J. (2002). Coda wave interferometry for estimating nonlinear behavior in seismic velocity. *Science*, *295*(5563), 2253–2255. https://doi.org/10.1126/science.1070015

Snieder, R., Prejean, S. G., & Johnson, J. B. (2006). Spatial variation in Mount St. Helens clones from coda wave analysis. *Centre for Wave Phenomena Consortium Project 2006*, 247–252. http://www.cwp.mines.edu/Meetings/Project06/cwp543.pdf

Snieder, R., & Vrijlandt, M. (2005). Constraining the source separation with coda wave interferometry: Theory and application to earthquake doublets in the Hayward fault, California. *Journal of Geophysical Research: Solid Earth*, *110*(4), 1–15. https://doi.org/10.1029/2004JB003317

Toksoz, M. N., Johnston, D. H., & Timur, A. (1979). Attenuation of seismic waves in dry and saturated rocks -I. Laboratory measurements. *Geophysics*, *44*(4), 681–690. https://doi.org/10.1190/1.1440970

Walsh, J. B. (1965). The effect of cracks on the compressibility of rock. *Journal of Geophysical Research*, *70*(2), 381–389. https://doi.org/10.1029/JZ070i002p00381

Xie, F., Ren, Y., Zhou, Y., Larose, E., & Baillet, L. (2018). Monitoring local changes in granite rock under biaxial test: a spatiotemporal imaging application with diffuse waves. *Journal of Geophysical Research: Solid Earth*, *123*(3), 2214–2227. https://doi.org/10.1002/2017JB014940

Zhou, S., Xia, C., & Zhou, Y. (2018). A theoretical approach to quantify the effect of random cracks on rock deformation in uniaxial compression. *Journal of Geophysics and Engineering*, *15*(3), 627–637. https://doi.org/10.1088/1742-2140/aaa1ad

Zhubayev, A., Houben, M. E., Smeulders, D. M., & Barnhoorn, A. (2016). Ultrasonic velocity and attenuation anisotropy of shales, Whitby, United Kingdom. *Geophysics*, *81*(1), D45–D56. https://doi.org/10.1190/GEO2015-0211.1

Zotz-Wilson, R. (2020). Coda-wave monitoring of continuously evolving material properties. https://doi.org/https://doi.org/10.4233/uuid:9c0b2f03-040b-4ec8-b669-951c5acf1f3b

Zotz-Wilson, R., Boerrigter, T., & Barnhoorn, A. (2019). Coda-wave monitoring of continuously evolving material properties and the precursory detection of yielding. *The Journal of the Acoustical Society of America*, *145*(2), 1060–1068. https://doi.org/10.1121/1.5091012

3

PRECURSORY SIGNALS TO THE ONSET OF LABORATORY STRESS-DRIVEN FAULT SLIP THROUGH ACOUSTIC MONITORING

Precursory signals to earthquakes have been observed in various forms, such as changes in fluid pressure, occurrence of small local earthquakes, or changes in apparent seismic velocity. The understanding of these changes remains an ongoing area of study. Cyclic stress-driven fault reactivation was conducted under different pore pressure conditions, while continuously monitoring ultrasonic seismic waves. Analysing the evolution of P- and S-wave velocities, transmitted amplitudes, and coda wave interferometry-derived velocity changes revealed consistent precursory signals for reactivation under varying stress conditions along the tested fault planes. The precursory signal from the transmitted amplitudes and the coda shows more lead time to fault reactivation compared to the direct first arrival S- or P-wave velocities. These precursory signals were linked to the physical processes of asperity degradation and creep during the pre-slip phase. Demonstrating a comparison to similar precursory signals observed in the field, this study highlights the feasibility of time-lapse monitoring to identify precursors to fault reactivation and establishes a connection between structural processes along the fault plane and seismic signals, contributing to the improvement of future forecasting models.

3.1. INTRODUCTION

Earthquake predictions have a long history (Dieterich, 1978; Geller, 1997; Scholz et al., 1973), and are made using reoccurrence intervals (Shimazaki & Nakata, 1980), or the relative earthquake size distribution (b-value) (Gulia et al., 2020). For induced seismicity, forecasts are made using probabilistic models (Király-Proag et al., 2016; Langenbruch et al., 2018), which can include production scenarios (Dempsey & Suckale, 2017). Before the occurrence of various earthquakes, anomalous changes in parameters, such as fluid pressure, electrical and magnetic fields, the frequency of occurrence of small local earthquakes, and apparent seismic velocity have been observed (Dieterich, 1978; Scholz et al., 1973). To try to understand the mechanisms causing these, laboratory studies have been performed, studying the micro-fracturing and changes in intact rocks under stress (Brace, 1968; Main & Meredith, 1989), but also to investigate the nucleation of faulted rocks (Latour et al., 2013), stick slip behaviour (Brace, 1968), friction laws (Marone, 1998) and characteristics (Byerlee, 1967; Kaproth & Marone, 2013; Shreedharan et al., 2019), the effects of pore pressure on slip stability (Cappa et al., 2019; Ougier-Simonin & Zhu, 2013; Rutter & Hackston, 2017) and fault gouge (Bakker et al., 2016; Hunfeld et al., 2017). But forecasting earthquakes remains a challenging task (Pritchard et al., 2020). More recent studies have included passive acoustic monitoring to fault slip and friction experiments (Dresen et al., 2020; Kwiatek et al., 2014; Noël et al., 2019; Wang et al., 2020; Ye & Ghassemi, 2018, 2020), mostly to investigate fault mechanics and to target the onset seismic slip, and moment release. Fault slip can be aseismic (McGarr & Barbour, 2018; Ye & Ghassemi, 2020), therefore active acoustic measurements could improve the understanding of both aseismic as seismic slip.

It is well known from laboratory experiments that seismic velocities vary with the level of applied stress (Birch, 1960, 1961), this is mostly attributed to micro-crack closure, opening, or formation (Nur, 1971; Walsh, 1965). Measured velocity changes hence could be related to stress and structural changes along faults, and it could be attempted to relate the precursory change in velocity to physical processes to improve forecasting of earthquakes. A limited number of studies have investigated the change in seismic velocities in direct shear setting (Kaproth & Marone, 2013; Kaproth & Marone, 2014; Scuderi et al., 2016; Shreedharan et al., 2020), mostly using ultrasonic acoustic (P-wave) monitoring. Shreedharan et al. (2021a) included an analysis of amplitude to quantify stress variations during the laboratory seismic cycle in a double-direct shear experiment, showing that seismic amplitudes are more sensitive to changes in the fault zone compared to the wave speed. However omitting the effect of pore pressure, which has a large effect on wave propagation (Winkler & Nur, 1979). It has been shown that the coda of the acoustic waves traveling through the medium is exceptionally sensitive to (stress) changes in the microstructure (Snieder et al., 2002; Stähler et al., 2011; Xie et al., 2018; Zhang et al., 2012; Zotz-Wilson et al., 2019). Utilizing coda wave interferometry, relative velocity changes can be derived (Snieder, 2002; Snieder et al., 2002) and used to predict the onset of failure of intact rocks loaded under a constant rate (Zotz-Wilson et al., 2019, chapter 2 of this thesis). Given the success of coda wave interferometry in detecting oncoming failure in intact rocks, we also test the possibilities of coda wave interferometry for detecting the onset of fault reactivation, which is characterized by fault creep and pre-slip (Figure 3.1).

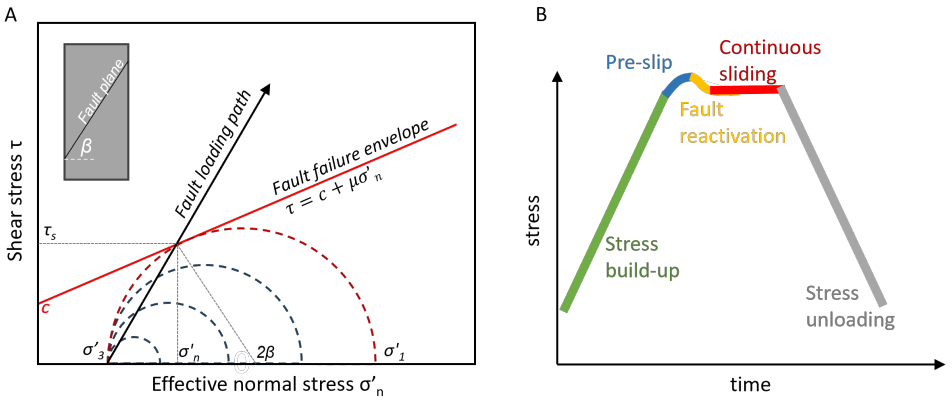

Figure 3.1: Sketch of fault reactivation. A. Mohr-Coulomb stresses visualize fault reactivation at increased axial stress. B. Loading and reactivation phase in the stress data.

In this chapter, we load saw-cut sandstone samples to reactivate the fault plane (Figure 3.1), while continuously monitoring P- or S-waves. The temporal evolution of the P- and S-wave velocities, their amplitudes, and coda are investigated to detect stress changes along a saw-cut fault plane under different pore pressure conditions. With the aim to detect the onset of fault reactivation and to find clear precursors to failure that extend across the various stress conditions in the laboratory experiments. We demonstrate the feasibility of time-lapse monitoring to identify precursors to fault reactivation and provide a link between structural processes along the fault plane and seismic signals which can improve future forecasting models.

3.2. EXPERIMENTAL PROCEDURE

3.2.1. ROCK SAMPLES

The fault reactivation experiments were performed in Red Felser sandstones. They are part of the Rotliegend formation and formed during the early Permian and are obtained from a quarry in Germany. The rock properties, lithology, porosity, and permeability, of the Red Felser are very similar to the Slochteren sandstone and are therefore used as analogous to the Groningen gas reservoir. The rock samples have an effective porosity of 20% ± 1%, obtained using a gas expansion (Helium) pycnometer, and a fairly homogeneous composition of 89% quartz, 6% orthoclase, 4% kaolinite, and 1% albite (Eradus, 2019). The samples are 30mm in diameter and 70mm in length and contain a saw-cut fault plane at an angle of 35 degrees to the vertical axis.

3.2.2. EXPERIMENTAL PROTOCOL

Prior to testing, all the samples were saturated with water, while the air was removed by creating a vacuum. The samples were loaded in a Hoek-Cell, a triaxial apparatus, which was placed in a homemade uniaxial loading frame with a 500 kN loadcell (Figure 3.2). The fluid pressure was imposed at the bottom of the sample, but measured at both

the inlet and outlet. The difference between the top and bottom was less than 0.5 bar. Both confining pressure and pore fluid pressure was maintained using an ISCO pump model 100DM. The shortening of the sample was recorded using two Solartron AX/1/S linear variable displacement transducers (LVDTs). All displacement data was corrected for elastic machine and piston deformation afterward.

The stress-driven cyclic reactivation experiments were performed with three different background fluid pressures, namely a drained experiment (0 MPa), 10 MPa, and 20 MPa while monitoring with ultrasonic transmission measurements, using P- and S- wave transducers. The experimental protocol consisted of the following consecutive steps; first, the sample was hydrostatically loaded to 30 MPa. The fluid pressure was imposed at a rate of 0.5 MPa per min and reaching the desired pressure the sample was loaded, with a vertical axial constant rate of 0.005 mm/s, until the reactivation zone was reached (Veltmeijer et al., 2023), characterized by bending of the stress-strain curve and the fault starting to slide along its plane with the velocity of 0.006 mm/s imposed by the loading of the sample (Figure 3.1 and Figure 3.2). At this point, the stress was cyclically decreased and increased in steps of 20 MP with the same rate of 0.0005 mm/s, such that the lower limit of the stress remained constant in each of the cycles. After six cycles the stress was lowered and the sample was removed from the set-up.

Ultrasonic transmission measurements were conducted on all experiments, simultaneously with the mechanical data acquisition, using either P or S-wave transducers integrated into the pistons of the loading system. The waveforms were generated using an Agilent 33210A waveform generator, amplified by an RF Power amplifier, then sent and received using Olympus 1MHz/.5" v153 (S-wave) or v103 (P-wave) transducers, and

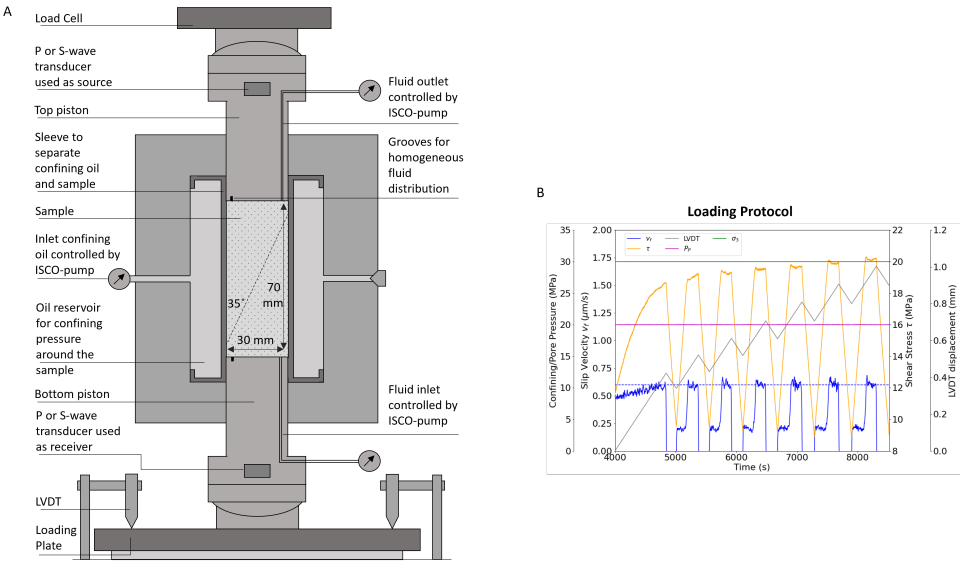

Figure 3.2: A: Scheme of Hoek-cell used for triaxial experiments (not to scale). B: Loading protocol, showing the protocol for a constant pore pressure of 20MPa.

finally recorded using a Yokogawa DL9240L oscilloscope. When using the v153 (S-wave), the transducers were placed such that the polarization of the shear source and receiver was aligned and perpendicular to the saw-cut fault (Figure 3.3). The peak operating frequency of both types of transducers is 1MHz and the acoustic signals were recorded every 3 seconds for 100 μs. To increase the signal-to-noise ratio, every recorded waveform is a stack of 128 S-waves, each sent 2 ms apart.

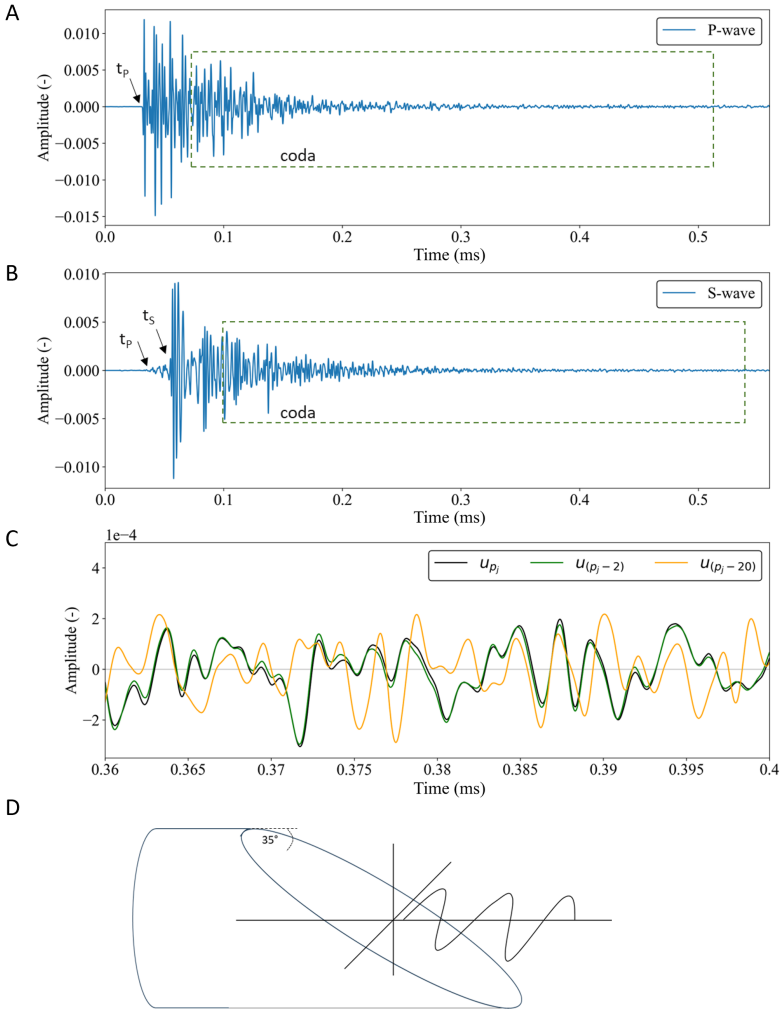

Figure 3.3: Recorded transmission wavelets with in A. P-wave and in B. S-wave transducers as source and receiver. The arrival time of the P-wave (t_P) and S-wave (t_S) are indicated as well as the length of the used coda. C. shows a part of the coda of three wavelets. Where u_{p_j} is the to-be correlated wavefield and is lagging behind the reference wavefield by N=2 and N=20 (Eq. 1.6), and D. shows the polarization of the S-wave transducers relative to the fault plane.

3.2.3. DATA ANALYSIS

Signals were logged for force (N), confining and fluid pressure (bar), displacement (mm), and wave arrival times (s) and amplitude (V). From these signals the shear stress (τ), friction coefficient (μ), and effective normal stress (σ_n) along the fault plane (Figure 3.1) are derived from the principal stresses, σ_1 (axial stress) and $\sigma_2 = \sigma_3$ (confining stress), as given by

$$\mu = \frac{\tau}{\sigma_n - P_f}, \tag{3.1}$$

with,

$$\tau = \frac{\sigma_1 - \sigma_3}{2} \sin 2\alpha, \tag{3.2}$$

and,

$$\sigma_n = \frac{\sigma_1 + \sigma_3 - 2P_f}{2} - \frac{\sigma_1 - \sigma_3}{2} \cos 2\alpha, \tag{3.3}$$

where σ_1 and σ_3 are the axial and radial stress respectively, P_f the pore pressure, and α is the fault angle with respect to the vertical (Byerlee, 1967; Wang et al., 2020). The τ and σ_n are corrected for a changing contact area of the fault due to fault slip. The fault slip (s) is mostly determined from the total axial displacement (Δl_{LVDT}), but corrected for the displacement of the loading machine (Δl_{MD}) (Wang et al., 2020), as follows:

$$s = \frac{\Delta l_{LVDT} - \Delta l_{MD}}{\cos \alpha}. \tag{3.4}$$

The displacement of the loading machine (Δl_{MD}) can be estimated using the stiffness of the machine (K_M), and the force drop (F_N), rewriting Equation (3.4) into:

$$s = \frac{\Delta l_{LVDT} - \frac{F_N}{K_M}}{\cos \alpha}. \tag{3.5}$$

We report the transmitted amplitudes as acoustic transmissivity, T (Nagata et al., 2008; Shreedharan et al., 2021a) as $T = |A_{max}|$, which is defined by the maximum amplitude of the recorded P- or S-wave. Additionally, coda wave interferometry (CWI) (Snieder, 2006; Snieder et al., 2002) is used to monitor the velocity change between two consecutive recorded waves (Figure 3.3). The theory of coda wave interferometry is described in Chapter 1.

3.3. RESULTS

3.3.1. FAULT SLIP BEHAVIOUR

Slip along the fault is induced by increasing the vertical displacement from below the sample (Figure 3.2B). The force is measured on top of the sample, therefore, it can be assessed whether this imposed displacement leads to a stress increase. Once no further increase in stress is observed, it indicates that the imposed displacement has been compensated for by the movement of the sample along the fault, hence, fault reactivation and

slip can be easily inferred from the stress curves (Figure 3.2B, Eq. 3.4). From the principal stresses (Eq. 3.1), we derived the normal and shear stress along the fault, as well as the friction coefficient μ (Figure 3.4). In general, the fault exhibits very similar behaviour throughout the cycles for each of the tested confining pressures. The main difference is the higher effective stresses on the fault in the experiments without imposed pore pressures. The stresses and friction along the fault increase with displacement, until all the imposed displacement has been compensated for by the movement along the fault, at which point the friction and stresses level out (Figure 3.2B). In these saw-cut experiments, it is assumed that the entire fault plane of the smooth saw-cut faults accommodates slip in each cycle. The slip rates along the faults are governed by the displacement

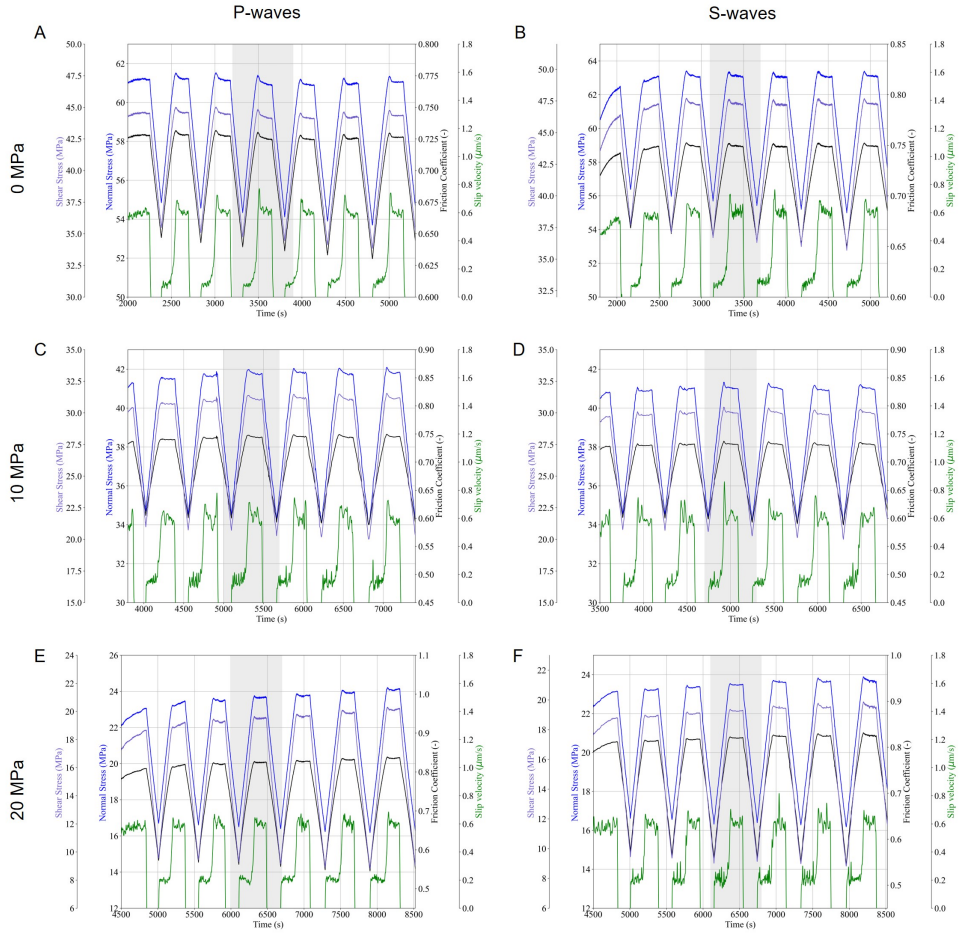

Figure 3.4: Evolution of mechanical loading parameters during stress-cycling. On the left side P-wave monitoring and on the right side S-wave monitoring was performed during the stress cycling. In A and B the experiment was performed under drained conditions (pore pressure 0 MPa) in C and D with a constant pore pressure of 10 MPa and in E and F with a constant pore pressure of 20 MPa. The grey shaded area, the third cycle is enlarged in Figure 3.6.

rate of 0.6 μm/s (projected to the fault angle). During the constant sliding phase, the slip velocities fluctuate around this rate. Stick-slip events with peak slip velocities below 1 mm/s are defined as slow stick-slip events (Wang et al., 2020). The maximum slip velocities observed are <1 μm/s, therefore all recorded slip events are slow slip. Prior to these maximum slip velocities, low velocities of about 0.2 μm/s are observed during the loading of the sample, indicating, that while most of the imposed displacement results in increasing stresses, some of it is compensated for by slight movement along the fault.

The mechanical and seismic parameters of each third cycle, representing all the cycles, are visualized in Figure 3.6. Although fault slip in these experiments is imposed by the constant displacement rate of 0.6 μm/s, at the onset of the fault reactivation, slip ve-

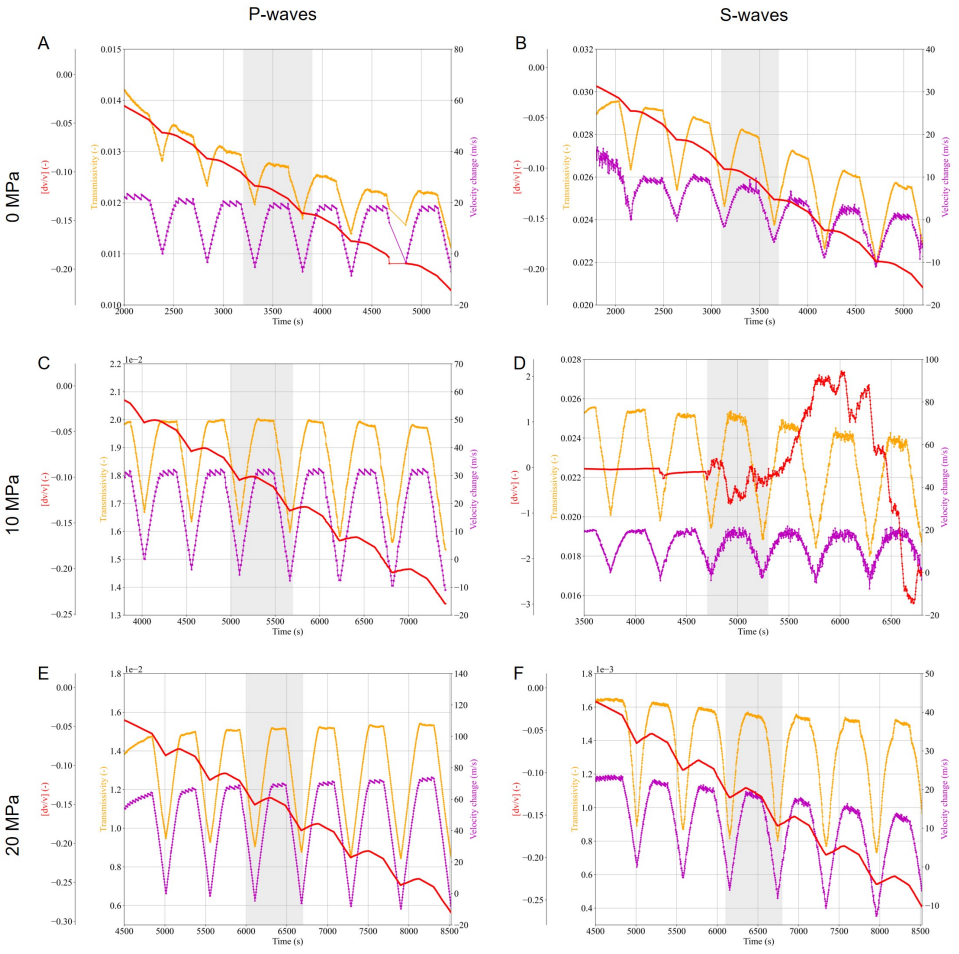

Figure 3.5: Evolution of seismic parameters during stress-cycling. On the left side P-wave monitoring and on the right side S-wave monitoring was performed during the stress cycling. In A and B the experiment was performed under drained conditions (pore pressure 0MPa) in C and D with a constant pore pressure of 10 MPa and in E and F with a constant pore pressure of 20 MPa. The grey shaded area, the third cycle is enlarged in Figure 3.6.

locities exhibit peaks exceeding this rate by up to 30%. In the setup, the force is measured on top of the sample (Figure 3.2A). Once the shear strength is reached and the fault reactivated, the top half of the sample is able to slip at a faster rate than imposed, causing a drop in stress resulting in higher slip velocities (Eq. 3.4). We infer this fault reactivation as a slow stick-slip behaviour, this is followed by a continuous slow slip phase with velocities fluctuating around 0.6 μm/s until the unloading of the sample.

The transmitted amplitude T and velocity, both the direct P- and S- wave velocity as the velocity change dv/v derived from the coda, cycle as expected along with the stress in each experiment (Figure 3.5) (Barnhoorn et al., 2018; Winkler & Nur, 1979). An overall decreasing trend is present throughout the cycles, which is most pronounced in the experiments without imposed pore pressure (Figure 3.5A, B). The experiment with 10 MPa pore pressure shows that a faulty connection of the transducer and the resulting noise

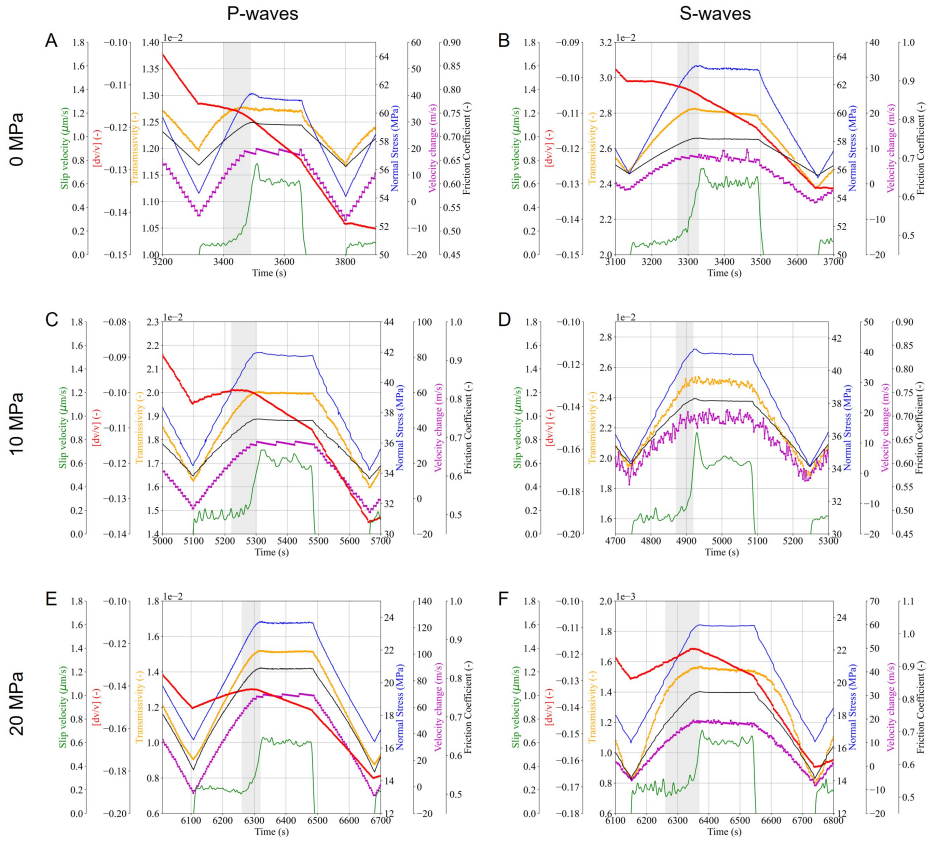

Figure 3.6: Evolution of mechanical and seismic parameters during third stress-cycle of Figure 3.4 and Figure 3.5. On the left side P-wave monitoring and on the right side S-wave monitoring was performed during the stress cycling. In A and B the experiment was performed under drained conditions (pore pressure 0 MPa) in C and D with a constant pore pressure of 10 MPa and in E and F with a constant pore pressure of 20 MPa. The grey shaded area, illustrates the areas in which the seismic parameters show a trend change indicative for the pre-slip phase.

in the signal has a big impact on the resulting analysed waveform parameters (Figure 3.5D). This is most evident in the velocity change obtained from the coda, whereas in all experiments, this shows a clear decrease over the cycles, for this 10 MPa experiment, it doesn't. Increasingly worsening of the noise obscures and masks the signals in the coda. In each slip event, both the values of T and dv/v increase due to the imposed stresses, but exhibit a reduction just before the actual fault slip (grey zone in Figure 3.6). This decline in T and dv/v is ascribed to the occurrence of fault pre-slip and dilation (Kaproth & Marone, 2013; Shreedharan et al., 2020). During the pre-slip stage, the contact area along the fault plane, the asperities, undergo gradual degradation causing this change in seismic parameters.

3.3.2. STRUCTURAL CHANGE FAULT PLANE

The saw-cut fault surface is smooth and is assumed to experience slip across its entire surface. Therefore on the macro-scale, the contact of the fault plane is considered smooth and a single contact. However, at a micro-scale, grain contacts act as asperities as visible in the CT-Image (Figure 3.7). Through this interaction, these grains can break, fracture, and be crushed due to the high stresses along the fault plane. This process results in the formation of a layer of finer-grained material along the fault plane, which increases with each cycle of increased stresses and fault slip. The amount of gouge formed depends on the shear stresses along the fault plane (Figure 3.8). Notably, the quantity of gouge formed after the experiment is highest when no imposed pore pressure is present. Additionally, it is evident that, even though the fault surface appears smooth, the saw leaves small grooves along which most asperities become locked and crushed, as seen in the pattern of formed gouge (Figure 3.8).

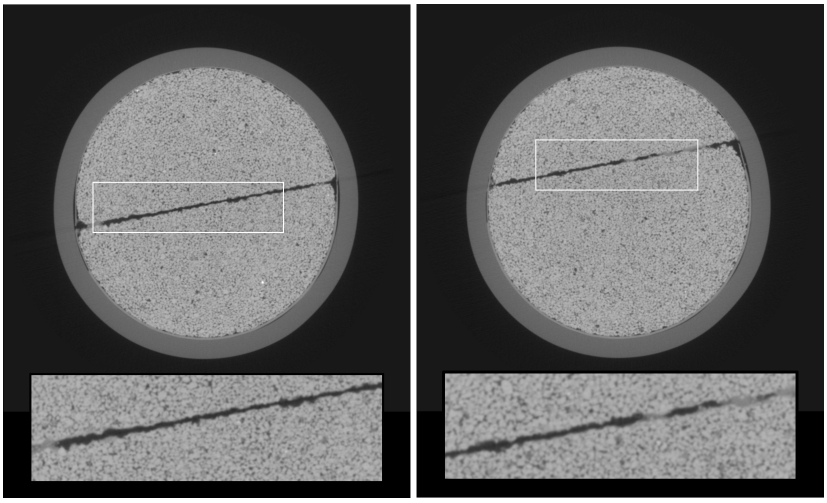

Figure 3.7: Two horizontal CT slices showing the saw-cut fault (black line) after the sliding experiment, without any pressure left on the fault plane (no contact anymore between two fault planes). Including a zoom around the fault plane showing local asperities along the fault planes and some small gouge material (blurry grey in fault plane). The scans are made in Nanotrom NF180 microCT scanner with a resolution (voxel size) of 49.1 μm

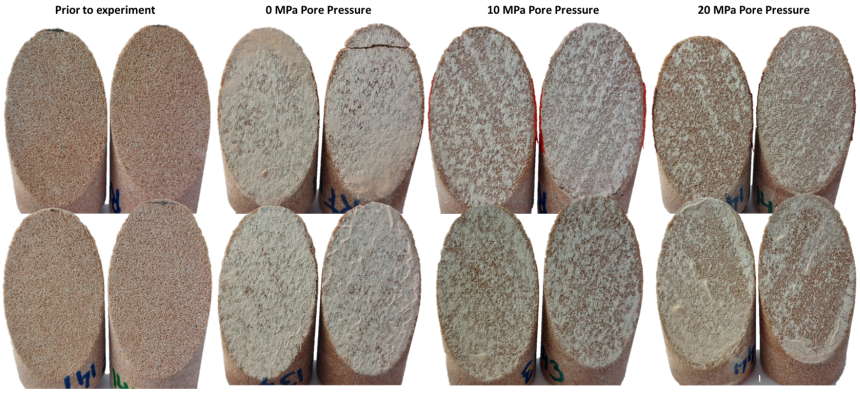

Figure 3.8: Pictures of the (dried) samples before and after the cyclic reactivation experiment. The formed gouge layer is visible as the whitish powder on the fault plane. The tip of the fault plane of the sample on top row second from left was broken during the sample extraction of the sleeve after finishing the experiment.

3.4. DISCUSSION

3.4.1. MECHANICAL BEHAVIOUR

In total 6 stress-driven reactivation cycles were performed under different confining conditions including ultrasonic monitoring with P- or S-wave transducers. Each cycle can be divided into three parts. Firstly, stress increase, including the preparatory slip and reactivation phase. Secondly, constant sliding, during which all the added imposed stress is compensated for by fault slip resulting in a more or less constant stress level and thirdly stress decrease, after which a new cycle starts. In the stress-strain data presented in Figure 3.9, it's evident that the cycles do not follow the same loading and unloading path, and higher stresses are required to reactivate the fault compared to the previous constant sliding. This suggests permanent deformation of the fault plane. A decrease in axial stress reduces the effective normal stress on the fault, facilitating relaxation and healing. On the contrary, an increase in effective normal stress leads to fault compaction and enhanced locking of asperities, strengthening the fault. This results in a slightly higher reactivation stress requirement.

Additionally to fault compaction, sliding and pressuring of the fault cause grains

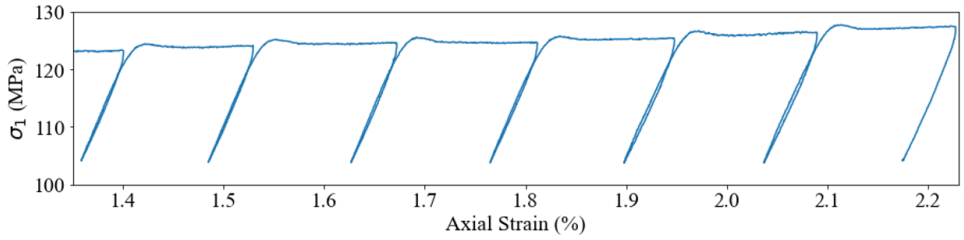

Figure 3.9: Stress cycles of drained experiment, showing increasing axial stress needed to reactivate the fault and a difference in unloading and loading paths per cycle.

along the surface to be crushed, changing the fault properties like the friction coefficient, in our quartz-rich sample. The crushed grains on the fault surface would be expected to have a frictional strengthening effect (Bakker et al., 2016; He et al., 2013), contributing to the restrengthening of the fault in each cycle. Even though the fault strengthens and potentially more energy could be released by reactivation of the fault plane, Naderloo et al., 2023; Naderloo et al., 2022 show a decreasing seismicity output due to deterioration of the fault plane. They state that the uniform reduction in roughness and asperity on the fault plane causes a decreasing (measured) seismicity output. This reduction in roughness and asperity on the fault or gouge formation can be seen in the active ultrasonic measurements as well. In each cycle the stresses are returned to the same base level in axial stress (σ_1), however, the ultrasonic parameters do not return to the same level, we infer this decrease to be due to the additional attenuation by gouge formation. This overall decrease is most prominent in the experiments without imposed pore pressure, resulting in higher effective stresses along the fault plane. This is visible on the retrieved fault planes, which show the most gouge present for these samples (Figure 3.8). Gouge formation, as evident in Figure 3.8, is a structural change. According to theory, S-waves should be more sensitive to structural changes as they travel through the matrix (Barnhoorn et al., 2018). Given the constant imposed pore pressure, any change observed in the seismic parameters is attributed to changes in the matrix. When returned to the same stress levels, the T, and velocities obtained by S-wave monitoring exhibit, cycle to cycle, more attenuation than P-waves (Figure 3.5), confirming the greater sensitivity of S-waves to gouge formation. With passive monitoring this increase in gouge formation and the resulting attenuation of the generated waves could pose a problem, as when the fault moves aseismic (we define aseismic as no recorded (micro-) seismicity) it would not be noticed. Using active monitoring a constant source signal was used, hence we can both infer the fault deterioration as the aseismic and seismic fault movement.

3.4.2. PRECURSORY SIGNALS

Kaproth and Marone, 2014, and Shreedharan et al., 2021a have shown that amplitude and direct P-wave velocity change before fault reactivation in a direct shear experiment. They didn't take into account pore pressure and high confinement to bring the experiment closer to subsurface conditions. Pressure (incl. pore pressure) has a large influence on the velocity and attenuation of the waves (Barnhoorn et al., 2018; Passelègue et al., 2018; Winkler and Nur, 1979; etc.). This chapter focuses on obtaining precursory signals to stress-driven fault reactivation under different pressure conditions, comparing P- and S-wave monitoring. We include coda wave interferometry to assess small stress variations along the fault plane.

Prior to fault reactivation and continuous sliding phase, a pre-slip is present (grey zone in Figure 3.6), in which we observe a transition from background creep velocities (around 0.2μm) during loading to continuous sliding with the imposed slip velocity of 0.6μm. During the pre-slip phase, the shear stress reaches the shear strength of the fault plane and along the fault plane asperities are destroyed (Scuderi et al., 2016; Shreedharan et al., 2021a), contributing to the gouge layer and opening of the fault causes decreasing asperity contact. These processes have a direct influence on the seismic parameters. The transmitted amplitudes T and velocity change in Vp, Vs, and dv/v exhibit

a precursory reduction, demonstrating sensitivity to pre-seismic deformation (grey zone in Figure 3.6). This reduction is a trade-off between the increasing stresses and the fault creep during the pre-slip phase. The seismic parameters follow the dominant physical process along the fault plane. The velocities and transmitted amplitude increase due to compaction and healing of the fault plane, causing new asperity contact and strengthening of the fault. They start to decrease as the effect of creep is dominant over compaction and stabilizing during continuous sliding. This is followed by a sharp decrease during unloading, releasing stress from the system. Hence the velocities and transmitted amplitudes provided a view of the fault strength evolution during the laboratory reactivation cycles and can be used to identify the pre-slip phase and act as a precursor to fault reactivation. No significant differences or trends are observed in precursory signals for the different stress conditions tested, nor does the deterioration of the fault plane limit the precursory signals, i.e. in the later cycles we observe similar signals as in the first cycle.

We can compare these precursory signals to the field study of Chiarabba et al., 2020 (Figure 3.10A) in which they observed an up to 5% increase in P-wave velocity on the part of the fault which experienced large co-seismic slip during a magnitude 6.5 earthquake in Norcia, Italy. At this hypocentre location, the initial velocity increase was followed by a decrease of about 4%, suggesting that although the (entire) fault was under elastic stiffening during the preparatory phase (Vp increase), a zone around the hypocentre experienced a seismic velocity reduction during the accelerated fault creep phase, as observed in the laboratory experiments. The velocity reduction around the main shock hypocentre area is consistent with the failure of asperity contacts within the fault zone (Chiarabba et al., 2020), similar to the creep and destruction of asperities during the pre-slip phase in laboratory reactivation cycles (Figure 3.10). This example highlights the uniformity between the field and laboratory observations. The structural processes along the fault prior to fault reactivation are similar in lab and field scale, and therefore similar precursory signals are observed, with the main difference being the time scale. In the lab we notice the first precursors seconds before reactivation; given the study of Niu et al., 2008 and Chiarabba et al., 2020, we expect to detect precursory changes in velocity weeks before the earthquake. However, to validate this statement, more field studies should be conducted, also focusing on the precursory attenuation changes before the fault reactivation.

At first glance, the precursory signals look very similar from experiment to experiment and cycle to cycle (Figure 3.11), an important factor for forecasting purposes, as this implies this monitoring method is very robust and applicable in any stress condition. In Chiarabba et al., 2020, the precursory Vp reduction was noticeable a few days before the earthquake, while in the laboratory this occurs within seconds. Taking the peak strength of the fault as the reactivation point and the bending point of the seismic parameters as the precursory signal (i.e. trend reversal, from increase to decrease), the occurrence of the precursors in seconds to reactivation is plotted, as well as the stress needed for reactivation (Figure 3.11). Whereas it is clear that, in general, the T and dv/v show more lead time to reactivation compared to the direct wave velocities Vs and Vp. This distinction is less clear for P- or S-wave monitoring, but generally, the T of the S-waves tends to show more lead time to reactivation.

The noisy waveform data recorded during the 10 MPa pore pressure experiment with S-wave monitoring demonstrates the limitations of the monitoring method using coda due to significantly increasing noise levels. In contrast to the other experiments where the noise level remained relatively constant during the timespan of the experiment, this experiment suffered from progressively increasing noise in the data. The cause, identified as a wobbly connection of the transducer, leads to a degradation of the precursory signals of the acoustic data. This shows that maintaining a relatively constant noise level is important for monitoring and obtaining precursory signals.

While pre-seismic crustal velocity anomalies have been observed for limited earthquakes (Chiarabba et al., 2020; Niu et al., 2008), upscaling the findings in this chapter remains a challenge. More work is needed to upscale the investigated simple fault geometry, considering factors such as fault zone length, fault maturity, time, and complexity. Additionally, the impact of noise levels on the application of coda wave inter-

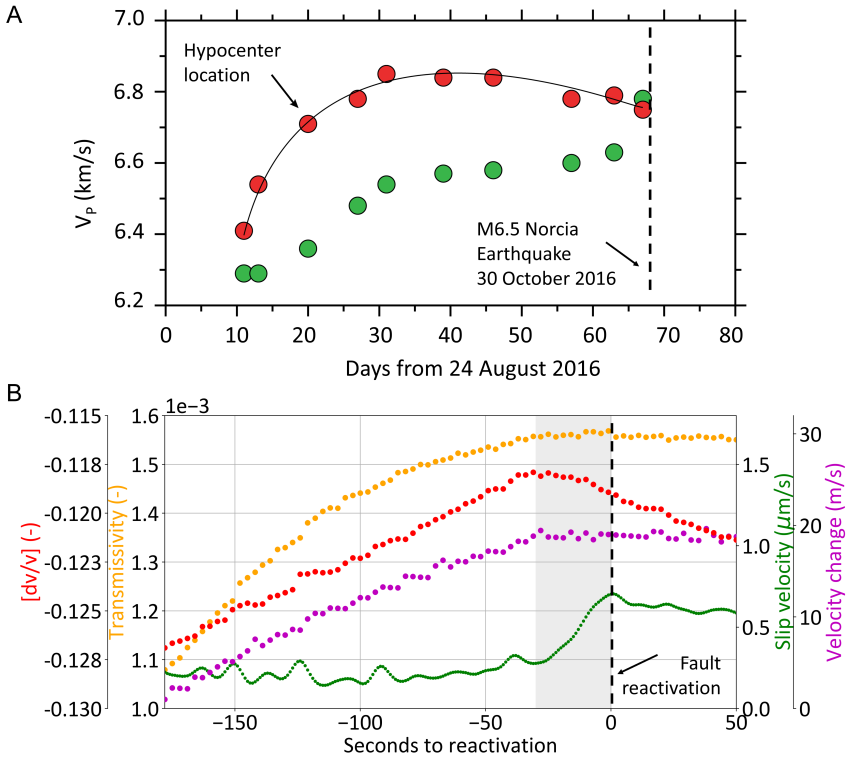

Figure 3.10: Comparing precursors from field study of Chiarabba et al. (2020) to laboratory fault reactivation in this chapter, showing similar precursory signals at lab and field scale. A. Figure modified from Chiarabba et al. (2020). Vp changes for two nodes located close to the 30 October hypocentre (red dots) and to the north (green dots). B. precursory signals to laboratory fault reactivation with 20 MPa pore pressure using S-wave monitoring.

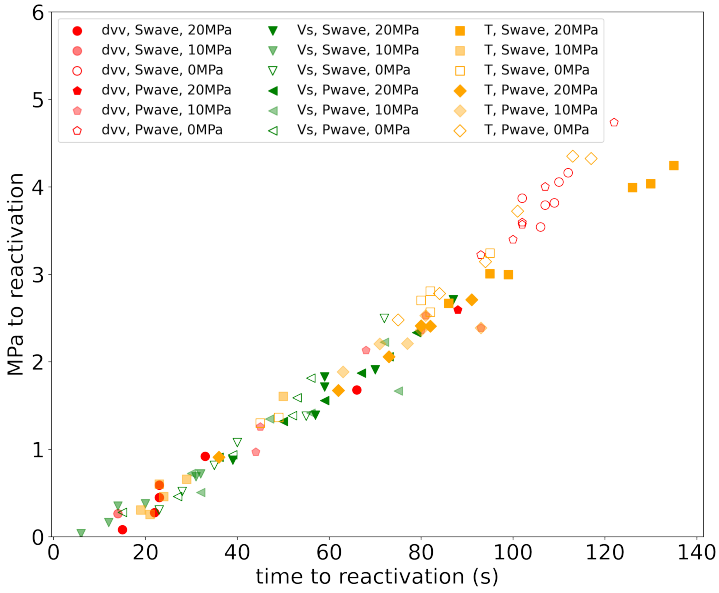

Figure 3.11: Appearance of precursors showing the lead time to reactivation and the corresponding stress needed to reactivate.

ferometry must be investigated before extending of the methodologies to field applications. In our controlled laboratory setting, we identified the pre-slip phase using parameters obtained from seismic monitoring, including the transmitted amplitudes, S- and P- wave velocity change, and the velocity change obtained by coda wave interferometry. This highlights that the transmitted amplitudes and the velocity changes, obtained from coda, offer more precision compared to the direct S- and P- wave velocities. Identifying this stage is the first step in forecasting fault reactivation and its resulting seismicity, both in laboratory and field scale. While this chapter does not include the forward time prediction of fault reactivation, recent efforts have been made to improve predictions of lab quakes using machine learning models, mostly based on acoustic emission measured in fault reactivation studies (Laurenti et al., 2022; Rouet-Leduc et al., 2017; Wang et al., 2022). Integrating the precursory signals from the transmitted amplitudes into these models has shown improvements in the prediction made by these machine learning models (Shreedharan et al., 2021b). The findings presented in this chapter suggest that including the precursory signals obtained by coda wave interferometry along with the transmitted amplitudes, into forecasting models to fault reactivation could enhance the forecasting capabilities of these models.

3.5. CONCLUSIONS

In this chapter, our objective is to monitor stress-driven cyclic fault reactivation with different effective stresses along the fault in laboratory experiments, comparing P-wave and S-wave monitoring and to improve our understanding of the connection between

seismic precursors and the mechanisms of failure.

By analysing the temporal evolution of the coda waves, seismic amplitudes, direct S- and P-wave velocities, stress changes on the fault surface can be identified, demonstrating the potential of seismic monitoring to identify the pre-slip phase of fault reactivation serving as a possible basis for forecasting stress-driven fault-slip. Our findings indicate that the velocity change from the coda wave interferometry and transmitted amplitude as precursory signal show more lead time to fault reactivation. The observed precursory reduction in transmitted amplitudes (T) and velocity changes in V_p,V_s, and dv/v highlight sensitivity to pre-seismic deformation. This reduction is indicative of the destruction of fault plane asperities, hence the formation of a gouge layer, and the opening of the fault leading to decreased asperity contact. This establishes a link between the mechanisms along the fault and the corresponding seismic parameters.

While our experiments illustrate the feasibility of active ultrasonic monitoring as a tool to identify precursors to laboratory stress-driven fault reactivation in a controlled environment, they currently do not extend to forward forecasting. The timing of the pre-phase, from detection to forward forecasting, and the additional complexity from lab to field-scale still require further study. The potential to infer aseismic stress changes indicative of seismicity could add value to monitoring and forecasting models. As a result, active techniques for monitoring and predicting stress changes have the potential to enhance seismicity predictions.

REFERENCES

Bakker, E., Hangx, S. J., Niemeijer, A. R., & Spiers, C. J. (2016). Frictional behaviour and transport properties of simulated fault gouges derived from a natural CO2 reservoir. *International Journal of Greenhouse Gas Control*, *54*, 70–83. https://doi.org/10.1016/j.ijggc.2016.08.029

Barnhoorn, A., Verheij, J., Frehner, M., Zhubayev, A., & Houben, M. (2018). Experimental identification of the transition from elasticity to inelasticity from ultrasonic attenuation analyses. *Geophysics*, *83*(4), MR221–MR229. https://doi.org/10.1190/geo2017-0534.1

Birch, F. (1960). The velocity of compressional waves in rocks to 10 kilobars: 1. *Journal of Geophysical Research*, *65*(4), 1083–1102. https://doi.org/10.1029/JZ065i004p01083

Birch, F. (1961). The velocity of compressional waves in rocks to 10 kilobars: 2. *Journal of Geophysical Research*, *66*(7), 2199–2224. https://doi.org/10.1029/JZ066i007p02199

Brace, W. F. (1968). Current laboratory studies pertaining to earthquake prediction. *Tectonophysics*, *6*(1), 75–87. https://doi.org/10.1016/0040-1951(68)90028-0

Byerlee, J. D. (1967). Frictional characteristics of granite under high confining pressure. *Journal of Geophysical Research*, *72*(14), 3639–3648. https://doi.org/10.1029/JZ072i014p03639

Cappa, F., Scuderi, M. M., Collettini, C., Guglielmi, Y., & Avouac, J. P. (2019). Stabilization of fault slip by fluid injection in the laboratory and in situ. *Science Advances*, *5*(3), 1–9. https://doi.org/10.1126/sciadv.aau4065

Chiarabba, C., De Gori, P., Segou, M., & Cattaneo, M. (2020). Seismic velocity precursors to the 2016 Mw 6.5 Norcia (Italy) earthquake. *Geology*, *48*(9), 924–928. https://doi.org/10.1130/G47048.1

Dempsey, D., & Suckale, J. (2017). Physics-based forecasting of induced seismicity at Groningen gas field, the Netherlands. *Geophysical Research Letters*, *44*(15), 7773–7782. https://doi.org/10.1002/2017GL073878

Dieterich, J. H. (1978). Preseismic fault slip and earthquake prediction. *Journal of Geophysical Research*, *83*(B8), 3940. https://doi.org/10.1029/jb083ib08p03940

Dresen, G., Kwiatek, G., Goebel, T., & Ben-Zion, Y. (2020). Seismic and aseismic preparatory processes before large stick–slip failure. *Pure and Applied Geophysics*, *177*(12), 5741–5760. https://doi.org/10.1007/s00024-020-02605-x

Eradus, D. (2019). *Petrographical description and petrophysical measurements on the red felser sandstone* [BSc Thesis]. Delft University of Technology.

Geller, R. J. (1997). Earthquake prediction: a critical review. *Geophysical Journal International*, *131*(3), 425–450. https://doi.org/10.1111/j.1365-246x.1997.tb06588.x

Gulia, L., Wiemer, S., & Vannucci, G. (2020). Pseudoprospective evaluation of the foreshock traffic-light system in ridgecrest and implications for aftershock hazard assessment. *Seismological Research Letters*, *91*(5), 2828–2842. https://doi.org/10.1785/0220190307

He, C., Luo, L., Hao, Q. M., & Zhou, Y. (2013). Velocity-weakening behavior of plagioclase and pyroxene gouges and stabilizing effect of small amounts of quartz under hydrothermal conditions. *Journal of Geophysical Research: Solid Earth*, *118*(7), 3408–3430. https://doi.org/10.1002/jgrb.50280

Hunfeld, L. B., Niemeijer, A. R., & Spiers, C. J. (2017). Frictional properties of simulated fault gouges from the seismogenic Groningen gas field under in situ P–T -chemical conditions. *Journal of Geophysical Research: Solid Earth*, *122*(11), 8969–8989. https://doi.org/10.1002/2017JB014876

Kaproth, B. M., & Marone, C. (2013). Slow earthquakes, preseismic velocity changes, and the origin of slow frictional stick-slip. *Science*, *341*(6151), 1229–1232. https://doi.org/10.1126/science.1239577

Kaproth, B. M., & Marone, C. (2014). Evolution of elastic wave speed during shear-induced damage and healing within laboratory fault zones. *Journal of Geophysical Research: Solid Earth*, *119*(6), 4821–4840. https://doi.org/10.1002/2014JB011051

Király-Proag, E., Zechar, J. D., Gischig, V., Wiemer, S., Karvounis, D., & Doetsch, J. (2016). Validating induced seismicity forecast models—induced seismicity test bench. *Journal of Geophysical Research: Solid Earth*, *121*(8), 6009–6029. https://doi.org/10.1002/2016JB013236

Kwiatek, G., Goebel, T. H., & Dresen, G. (2014). Seismic moment tensor and b value variations over successive seismic cycles in laboratory stick-slip experiments. *Geophysical Research Letters*, *41*(16), 5838–5846. https://doi.org/10.1002/2014GL060159

Langenbruch, C., Weingarten, M., & Zoback, M. D. (2018). Physics-based forecasting of man-made earthquake hazards in Oklahoma and Kansas. *Nature Communications*, *9*(1), 1–10. https://doi.org/10.1038/s41467-018-06167-4

Latour, S., Schubnel, A., Nielsen, S., Madariaga, R., & Vinciguerra, S. (2013). Characterization of nucleation during laboratory earthquakes. *Geophysical Research Letters*, *40*(19), 5064–5069. https://doi.org/10.1002/grl.50974

Laurenti, L., Tinti, E., Galasso, F., Franco, L., & Marone, C. (2022). Deep learning for laboratory earthquake prediction and autoregressive forecasting of fault zone stress. *Earth and Planetary Science Letters*, *598*, 117825. https://doi.org/10.1016/j.epsl.2022.117825

Main, I. G., & Meredith, P. G. (1989). Classification of earthquake precursors from a fracture mechanics model. *Tectonophysics*, *167*(2-4), 273–283. https://doi.org/10.1016/0040-1951(89)90078-4

Marone, C. (1998). Laboratory-derived friction laws and their application to seismic faulting. *Annual Review of Earth and Planetary Sciences*, *26*, 643–696. https://doi.org/10.1146/annurev.earth.26.1.643

McGarr, A., & Barbour, A. J. (2018). Injection-induced moment release can also be aseismic. *Geophysical Research Letters*, *45*(11), 5344–5351. https://doi.org/10.1029/2018GL078422

Naderloo, M., Veltmeijer, A., Jansen, J. D., & Barnhoorn, A. (2023). Laboratory study on the effect of stress cycling pattern and rate on seismicity evolution. *Geomechanics and Geophysics for Geo-Energy and Geo-Resources*, *9*(1), 1–18. https://doi.org/10.1007/s40948-023-00678-1

Naderloo, M., Veltmeijer, A., & Barnhoorn, A. (2022). Active and passive monitoring of fault reactivation under stress cycling. *Second International Meeting for Applied Geoscience & Energy*, 1576–1580. https://doi.org/10.1190/image2022-3750358.1

Nagata, K., Nakatani, M., & Yoshida, S. (2008). Monitoring frictional strength with acoustic wave transmission. *Geophysical Research Letters*, *35*(6), 1–5. https://doi.org/10.1029/2007GL033146

Niu, F., Silver, P. G., Daley, T. M., Cheng, X., & Majer, E. L. (2008). Preseismic velocity changes observed from active source monitoring at the Parkfield SAFOD drill site. *Nature*, *454*(7201), 204–208. https://doi.org/10.1038/nature07111

Noël, C., Passelègue, F. X., Giorgetti, C., & Violay, M. (2019). Fault reactivation during fluid pressure oscillations: transition from stable to unstable slip. *Journal of Geophysical Research: Solid Earth*, *124*(11), 10940–10953. https://doi.org/10.1029/2018JB016045

Nur, A. (1971). Effects of stress on velocity anisotropy in rocks with cracks. *J Geophys Res*, *76*(8), 2022–2034. https://doi.org/10.1029/jb076i008p02022

Ougier-Simonin, A., & Zhu, W. (2013). Effects of pore fluid pressure on slip behaviors: An experimental study. *Geophysical Research Letters*, *40*(11), 2619–2624. https://doi.org/10.1002/grl.50543

Passelègue, F. X., Brantut, N., & Mitchell, T. M. (2018). Fault reactivation by fluid injection: controls from stress state and injection rate. *Geophysical Research Letters*, *45*(23), 12, 837–12, 846. https://doi.org/10.1029/2018GL080470

Pritchard, M. E., Allen, R. M., Becker, T. W., Behn, M. D., Brodsky, E. E., Bürgmann, R., Ebinger, C., Freymueller, J. T., Gerstenberger, M., Haines, B., Kaneko, Y., Jacobsen, S. D., Lindsey, N., McGuire, J. J., Page, M., Ruiz, S., Tolstoy, M., Wallace, L., Walter, W. R., … Vincent, H. (2020). New opportunities to study earthquake precursors. *Seismological Research Letters*, *91*(5), 2444–2447. https://doi.org/10.1785/0220200089

Rouet-Leduc, B., Hulbert, C., Lubbers, N., Barros, K., Humphreys, C. J., & Johnson, P. A. (2017). Machine learning predicts laboratory earthquakes. *Geophysical Research Letters*, *44*(18), 9276–9282. https://doi.org/10.1002/2017GL074677

Rutter, E., & Hackston, A. (2017). On the effective stress law for rock-on-rock frictional sliding, and fault slip triggered by means of fluid injection. *Philosophical Transactions of the Royal Society A: Mathematical, Physical and Engineering Sciences*, *375*(2103). https://doi.org/10.1098/rsta.2016.0001

Scholz, C. H., Sykes, L. R., & Aggarwal, Y. P. (1973). Earthquake prediction: A physical basis. *Science*, *181*(4102), 803–810. https://doi.org/10.1126/science.181.4102.803

Scuderi, M. M., Marone, C., Tinti, E., Di Stefano, G., & Collettini, C. (2016). Precursory changes in seismic velocity for the spectrum of earthquake failure modes. *Nature Geoscience*, *9*(9), 695–700. https://doi.org/10.1038/ngeo2775

Shimazaki, K., & Nakata, T. (1980). Time-predictable recurrence model for large earthquakes. *Geophysical Research Letters*, *7*(4), 279–282. https://doi.org/10.1029/GL007i004p00279

Shreedharan, S., Bolton, D. C., Rivière, J., & Marone, C. (2020). Preseismic fault creep and elastic wave amplitude precursors scale with lab earthquake magnitude for the continuum of tectonic failure modes. *Geophysical Research Letters*, *47*(8), 1–10. https://doi.org/10.1029/2020GL086986

Shreedharan, S., Bolton, D. C., Rivière, J., & Marone, C. (2021a). Competition between preslip and deviatoric stress modulates precursors for laboratory earthquakes. *Earth and Planetary Science Letters*, *553*, 116623. https://doi.org/10.1016/j.epsl.2020.116623

Shreedharan, S., Bolton, D. C., Rivière, J., & Marone, C. (2021b). Machine learning predicts the timing and shear stress evolution of lab earthquakes using active seismic monitoring of fault zone processes. *Journal of Geophysical Research: Solid Earth*, *126*(7), 1–18. https://doi.org/10.1029/2020JB021588

Shreedharan, S., Rivière, J., Bhattacharya, P., & Marone, C. (2019). Frictional state evolution during normal stress perturbations probed with ultrasonic waves. *Journal of Geophysical Research: Solid Earth*, *124*(6), 5469–5491. https://doi.org/10.1029/2018JB016885

Snieder, R. (2002). Coda wave interferometry and the equilibration of energy in elastic media. *Physical Review E - Statistical Physics, Plasmas, Fluids, and Related Interdisciplinary Topics*, *66*(4), 8. https://doi.org/10.1103/PhysRevE.66.046615

Snieder, R. (2006). The theory of coda wave interferometry. *Pure and Applied Geophysics*, *163*(2-3), 455–473. https://doi.org/10.1007/s00024-005-0026-6

Snieder, R., Grêt, A., Douma, H., & Scales, J. (2002). Coda wave interferometry for estimating nonlinear behavior in seismic velocity. *Science*, *295*(5563), 2253–2255. https://doi.org/10.1126/science.1070015

Stähler, S. C., Sens-Schönfelder, C., & Niederleithinger, E. (2011). Monitoring stress changes in a concrete bridge with coda wave interferometry. *The Journal of the Acoustical Society of America*, *129*(4), 1945–1952. https://doi.org/10.1121/1.3553226

Veltmeijer, A., Naderloo, M., & Barnhoorn, A. (2023). Active and passive seismic monitoring of laboratory-based injection-driven fault reactivation. *84th EAGE Annual Conference & Exhibition*, 1–5. https://doi.org/10.3997/2214-4609.202310513

Walsh, J. B. (1965). The effect of cracks on the compressibility of rock. *Journal of Geophysical Research*, *70*(2), 381–389. https://doi.org/10.1029/JZ070i002p00381

Wang, K., Johnson, C. W., Bennett, K. C., & Johnson, P. A. (2022). Predicting future laboratory fault friction through deep learning transformer models. *Geophysical Research Letters*, *49*(19), 1–9. https://doi.org/10.1029/2022GL098233

Wang, L., Kwiatek, G., Rybacki, E., Bonnelye, A., Bohnhoff, M., & Dresen, G. (2020). Laboratory study on fluid-induced fault slip behavior: the role of fluid pressurization rate. *Geophysical Research Letters*, *47*(6), 1–12. https://doi.org/10.1029/2019GL086627

Winkler, K., & Nur, A. (1979). Pore fluids and seismic attenuation in rocks. *Geophysical Research Letters*, *6*(1), 1–4. https://doi.org/10.1029/GL006i001p00001

Xie, F., Ren, Y., Zhou, Y., Larose, E., & Baillet, L. (2018). Monitoring local changes in granite rock under biaxial test: a spatiotemporal imaging application with diffuse waves. *Journal of Geophysical Research: Solid Earth*, *123*(3), 2214–2227. https://doi.org/10.1002/2017JB014940

Ye, Z., & Ghassemi, A. (2018). Injection-induced shear slip and permeability enhancement in granite fractures. *Journal of Geophysical Research: Solid Earth*, *123*(10), 9009–9032. https://doi.org/10.1029/2018JB016045

Ye, Z., & Ghassemi, A. (2020). Heterogeneous fracture slip and aseismic-seismic transition in a triaxial injection test. *Geophysical Research Letters*, *47*(14), 1–9. https://doi.org/10.1029/2020GL087739

Zhang, Y., Abraham, O., Grondin, F., Loukili, A., Tournat, V., Duff, A. L., Lascoup, B., & Durand, O. (2012). Study of stress-induced velocity variation in concrete under direct tensile force and monitoring of the damage level by using thermally-compensated coda wave interferometry. *Ultrasonics*, *52*(8), 1038–1045. https://doi.org/10.1016/j.ultras.2012.08.011

Zotz-Wilson, R., Boerrigter, T., & Barnhoorn, A. (2019). Coda-wave monitoring of continuously evolving material properties and the precursory detection of yielding. *The Journal of the Acoustical Society of America*, *145*(2), 1060–1068. https://doi.org/10.1121/1.5091012

4

ACTIVE AND PASSIVE MONITORING OF FAULT REACTIVATION UNDER STRESS CYCLING

Increased seismicity, due to subsurface activities has led to increased interest in monitoring and seismic risk mitigation. In this study we combine passive and active acoustic monitoring methods to monitor fault sliding and reactivation in the laboratory. Acoustic emission (AE), a passive method, and ultrasonic transmission measurements, an active monitoring method, are performed during stress-cycling to monitor stress-driven fault reactivation. We show the use of the transmissivity and coda wave interferometry of the active acoustic measurements and the number of generated AE events for fault reactivation monitoring. Combining these two methods, we are able to detect the different phases of fault reactivation process under stress cycling including, early aseismic creep (pre-slip), fault slip, and continuous sliding. Combining both active and passive monitoring increases accuracy of monitoring and can lead to better seismic risk mitigation

Parts of this chapter have been published as M. Naderloo, A. Veltmeijer, & A. Barnhoorn, *Active and Passive Monitoring of Fault Reactivation under Stress Cycling.*, Second International Meeting for Applied Geoscience & Energy (2022).

4.1. INTRODUCTION

Increasing human activities in the subsurface, due to rising energy demand, and the demand for renewable energy have led to an increase in induced seismicity all over the world. Seismicity is recorded at different subsurface-related projects, such as water waste injection, gas extraction, and geothermal energy production sites. A well-known example is the M5.4 earthquake in Pohang (Kim et al., 2018), or the high number of seismicity recordings in Groningen, caused by gas extraction (van Thienen-Visser & Breunese, 2015).

Monitoring and seismic risk mitigation have received much interest over the years. Multiple studies have been conducted to improve the monitoring system of induced seismicity (Eaton, 2018; Grigoli et al., 2017; Mahani et al., 2016). Verdon et al., 2010, showed there is a correlation between the seismicity rate with injection rate and the production activities using passive monitoring. Using improved matching and locating techniques, Chen et al., 2018 showed better detection of the seismicity events and the clustering of seismic activity caused by the pre-existing faults and fractures with passive monitoring.

Monitoring induced seismicity, however, still poses a number of challenges, including the need for near-real-time monitoring and limitations associated with seismic network quality (Grigoli et al., 2017). For improving monitoring and managing system of induced seismicity, combining geophysical, geological, and hydrological data from the field with modelling is required. Potential seepage or leakage along faults or fracture zones was studied by Oye et al., 2021, using both active and passive monitoring techniques.

Similarly, active monitoring techniques are used to monitor changes in the subsurface prior to fault reactivation. Laboratory studies have shown the sensitivity of ultrasonic P-waves to the reactivation of faults for frictional sliding experiments (Kaproth & Marone, 2013; Shreedharan et al., 2021). Also at larger scale, precursory signals can be observed using active acoustic monitoring. Chiarabba et al., 2020 observed at a larger (crustal) scale an increase, and near the hypocentre, a decrease in P-wave velocity before an M6.5 in Italy.

Most of the studies in field or laboratory scale are based on either passive monitoring or active monitoring, only a limited number combine both techniques. It can be valuable and helpful for monitoring purposes to combine the active and passive acoustic methods. This study aims to shed light on using both passive and active acoustic methods for monitoring fault sliding under stress cycling on laboratory scale. We perform stress-driven fault reactivation experiments on sandstones under stress cycling.

4.2. METHOD

In this study, high porosity Red Felser sandstones were used, these are analog to the Rotliegend sandstones of the Groningen gas reservoir (in the north of the Netherlands). The cylindrical core samples were cut at an angle of 30 degree to the vertical cylinder axis to simulate a fault plane. The samples, including saw cut had dimensions of 30 ± 0.5 mm in diameter and 70 ± 2 mm in length. A gas expansion (Helium) pycnometer was used to determine the average connected porosity of the samples: 19-20%.

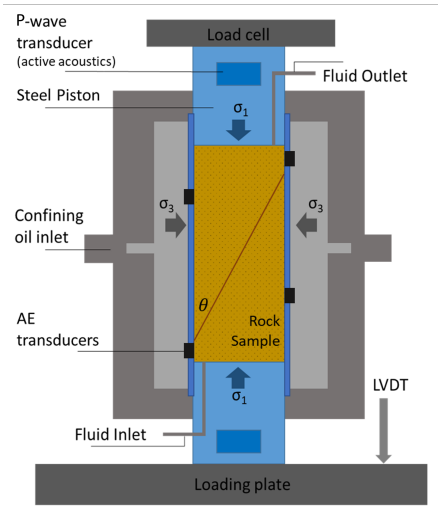

Figure 4.1: Schematic illustration of instrumented Hoek cell with AE sensors, and P-wave transducers. The shortening of the sample was recorded with two linear variable displacement transducers (LVDT's)

We used an instrumented Hoek cell in a 500kN uniaxial loading machine (Figure 4.1). A three-step stress-driven protocol for fault reactivation was performed (Figure 4.2).

1. During the first step, axial stress and confining pressure was increased hydrostatically up to the desired confining pressure of 20 MPa, while the sample was fully saturated.

2. During the second step, axial stress was increased to reach the pre-determined shear strength of the fault plane (the reactivation zone).

3. In step three, the cyclic reactivation scenario was performed in which after fault slip, axial stress (σ_1) was decreased with 12 MPa and afterwards increased again up to the previous stress (Figure 4.2).

Two sets of acoustic experiments were performed during stress-driven cyclic fault reactivation. Reactivation with passive acoustic emission (AE) monitoring and reactivation with active acoustic monitoring.

The active acoustic monitoring was performed using ultrasonic transmission measurements. Two P-wave transducers are integrated into the pistons in the loading system (Figure 4.1), with the source at the top and the receiver at the bottom of the sample. The transducers have a peak operating frequency of 1 MHz, and every 2 seconds, 512 P-waves were sent, recorded, and stacked to reduce the signal-to-noise ratio. The transmission data was analysed using the transmissivity: $T = |A_{max}|$, which is the maximum amplitude of the recorded P-wave. Additionally, coda wave interferometry (CWI) (Snieder et al., 2006) is used to monitor the change in velocity (dv/v) between two consecutive recorded waves. Using a moving reference wavefield for the CWI, the changing medium is continuously monitored (Zotz-Wilson et al., 2019).

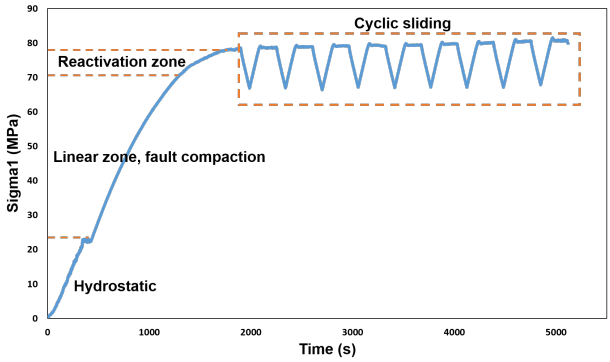

Figure 4.2: Axial stress (σ_1) as a function of time. Different phases of fault reactivation experiment; hydrostatic, linear zone, reactivation zone, and cyclic sliding.

The passive acoustic monitoring (AE) was performed using an array of 10 piezo-ceramic transducers (Figure 4.1) to detect micro-seismic events. The AE transducers are 5mm in diameter, with a dominant resonant frequency of about 1 MHz, and the signals were amplified using pre-amplifiers. The continuous recorded waveform data was cut into single waveforms (AE events) for further analysis, using a pre-defined trigger logic. These AE events were stored if, in five or more transducers, the waveforms recorded exceeds a voltage threshold of 25mV, within a time window of 480 points and a sampling rate of 2 MHz.

4.3. DISCUSSION OF RESULTS

In total, 9 stress-reactivation cycles were performed, including acoustic monitoring (Figure 4.2). The stress-driven fault reactivation cycles can be divided into three parts. 1. stress increase, consisting of pre-slip phase and the fault reactivation phase. 2. constant sliding (pure fault slip), in which the sample was continued to be stressed, but constant fault slip counteracted this increase, resulting in a more or less constant stress, and 3. stress decrease, after which a new cycle begins.

Figure 4.3 shows the AE results, the axial stress (σ_1), micro-seismic event amplitude and cumulative events are shown. A silence zone, showing zero generated AE event is caused by reducing the stress after fault slip. However, by increasing the stress, AE events start to appear before exceeding previous reached maximum stress (maximum stress from previous cycle) and before pure fault slip. AE events are generated from 97% of the maximum stress indicating the fault reactivation (Figure 4.3).

Prior to fault reactivation and pure fault slip, a pre-slip aseismic stage is present. During this pre-slip phase, the fault plane experiences creep (slow slip). During this stage the stress continues to build up, but shows a deviation from the linear increase (Figure 4.3, beige and blue colour). During this pre-slip phase (blue colour), low amplitude AE events (and a lower event rate) were recorded. After this phase, stress reaches its maximum value and then it drops, indicating fault reactivation. During reactivation (Figure 4.3, green zone), the event rate and maximum amplitude for the individual AE events increase. After reactivation, we observe continuous sliding (pure slip). During this phase

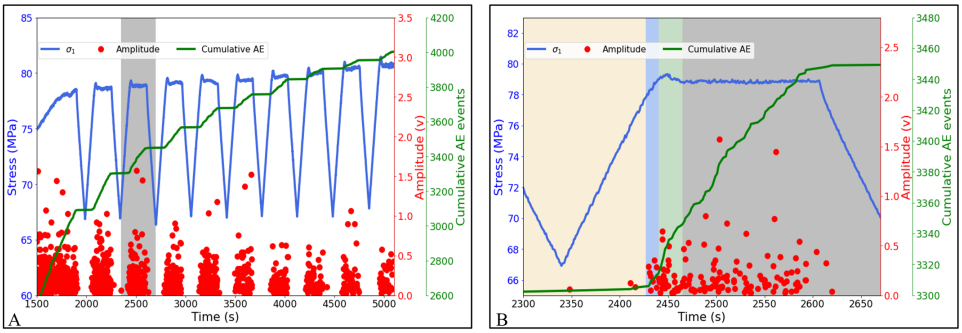

Figure 4.3: Passive acoustic data (AE) during cycling, showing axial stress (σ_1) as a function of time, and the appearance and amplitude of the single AE events and their cumulative. A. showing all the cycles, the cycle shaded grey is shown in B. B. showing the different phases of fault reactivation experiment; linear stress build-up phase in beige, the pre-slip/ early creep phase in blue, fault reactivation and slip in green, and afterwards in grey the continuous sliding.

(Figure 4.3, grey zone), continuous micro-seismic generation can be observed.

Figure 4.4 shows the data from active acoustic monitoring. Shown is the axial stress (σ_1), the cumulative velocity change ($[dv/v]_{sum}$) obtained by CWI, and the transmissivity (T). The velocity and transmissivity show an overall decreasing trend, but within each cycle the different phase of fault reactivation can be identified. $[dv/v]_{sum}$ and T, show an approximately linear increase due to the imposed increasing stress (Figure 4.4, beige zone). Before early creep phase (or before 95% of maximum stress), strain is slowly accumulating on fault plane and stress is building up, however, this stress is not enough to overcome the shear strength, thus the fault remains locked and the contact area between the two sides of fault increases (the asperities lock). This results in an constant (linear) increase of T and $[dv/v]_{sum}$ with increasing pressure and micro-seismic events are not generated.

Before fault reactivation, both $[dv/v]_{sum}$ and T show a deviation from their linear increase. This coincides with the early creep phase (aseismic stage) and this reduction is attributed to pre-slip and dilation (Kaproth & Marone, 2013; Shreedharan et al., 2021). During this aseismic phase, the contact area along the fault plane, or the asperities, are slowly destroyed, resulting in a reduction of T and $[dv/v]_{sum}$. The detection of the early creep phase using T and $[dv/v]_{sum}$ is at 95% of the maximum stress indicating the fault reactivation. After fault reactivation (stress drop) both parameters show a constant decrease, consistent with the continuous sliding and the continuous destruction of asperities along the fault plane.

Both the passive data and active data show, we can detect the early creep phase (aseismic stage), the fault reactivation (stress drop), and the continuous sliding phase. Therefore, both methods can be used as a monitoring method of pre-slip and can act as precursory signals to imminent fault slip.

The active monitoring shows precursory signal to fault slip from 95% of the failure point, whereas the passive (AE) method shows the first recorded events from 97% of the failure point. The active monitoring is independent of generated seismicity and can be deployed and used for monitoring at any stage of reactivation. Passive monitoring can

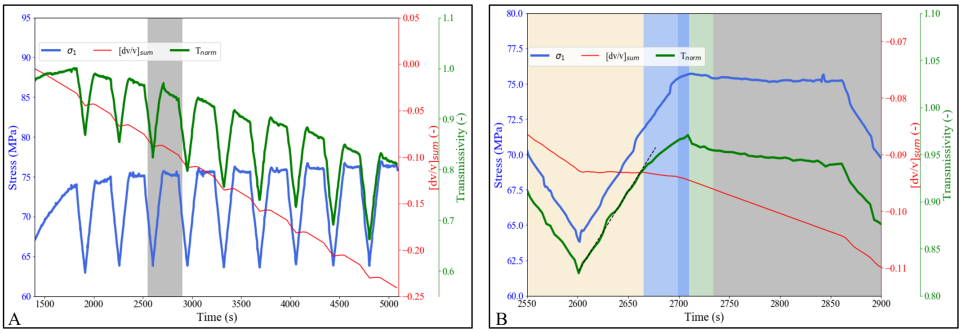

Figure 4.4: Active acoustic data during cycling, showing axial stress (σ_1) as a function of time, and the changing transmissivity (T) and cumulative velocity change$[dv/v]_{sum}$ during the cycling. A. showing all the cycles, the cycle shaded grey is shown in B. B. showing the different phases of fault reactivation experiment; linear stress build-up phase in beige, the pre-slip/ early creep phase in blue, fault reactivation and slip in green, and afterwards in grey the continuous sliding. Trend line indicates the clear reduction in transmissivity at the start of the pre-slip phase. The pre-slip/ early creep phase in blue has two shades, based on extra decrease in velocity change prior to fault reactivation.

provide valuable insight in the location and moment tensor of the fault reactivation and generated seismicity. Therefore, these methods complement each other and monitoring can be improved.

One of the most used strategies for seismicity risk mitigation is the traffic light system (TLS), in which an injection protocol is modified by flow rate or fluid pressure based on pre-defined thresholds of seismic magnitudes or other factors (Hofmann et al., 2018). The typical observable variables used for TLS decision-making are magnitude, peak ground velocity or peak ground acceleration, and the rate of events (Muntendam-Bos et al., 2022). Thus, using active acoustic analysis next to passive can greatly improve the monitoring accuracy and can benefit TLS.

4.4. CONCLUSION

In this study, we used the passive and active acoustic techniques to monitor stress-driven fault reactivation experiments under stress cycling.

1. We showed that both passive acoustic (acoustic emission) and active acoustic monitoring can be used to detect fault reactivation process under stress cycling which includes different phases; linear strain build-up, early creep (pre-slip), stress drop (main slip), and continuous sliding phase.
2. The active acoustic technique detected the early creep phase at 95% before failure, and AE at 97% before failure. The active methods are earlier and slightly more sensitive, and are independent of seismicity generated movement along the fault. Therefore, combination of both methods can be beneficial to increase accuracy of monitoring.

These results have shown that monitoring fault reactivation in the laboratory with the active and passive techniques is feasible. As a result, the combination of passive and

active techniques may be useful for monitoring faulted or critical stressed reservoirs that undergo cyclic stress behaviour.

REFERENCES

Chen, H., Meng, X., Niu, F., Tang, Y., Yin, C., & Wu, F. (2018). Microseismic monitoring of stimulating shale gas reservoir in sw china: 2. spatial clustering controlled by the preexisting faults and fractures. *Journal of Geophysical Research: Solid Earth*, *123*(2), 1659–1672. https://doi.org/10.1002/2017JB014491

Chiarabba, C., De Gori, P., Segou, M., & Cattaneo, M. (2020). Seismic velocity precursors to the 2016 Mw 6.5 Norcia (Italy) earthquake. *Geology*, *48*(9), 924–928. https://doi.org/10.1130/G47048.1

Eaton, D. W. (2018). *Passive Seismic Monitoring of Induced Seismicity*. Cambridge University Press. https://doi.org/10.1017/9781316535547

Grigoli, F., Cesca, S., Priolo, E., Rinaldi, A. P., Clinton, J. F., Stabile, T. A., Dost, B., Fernandez, M. G., Wiemer, S., & Dahm, T. (2017). Current challenges in monitoring, discrimination, and management of induced seismicity related to underground industrial activities: A European perspective. *Reviews of Geophysics*, *55*(2), 310–340. https://doi.org/10.1002/2016RG000542

Hofmann, H., Zimmermann, G., Zang, A., & Min, K.-B. (2018). Cyclic soft stimulation (CSS): a new fluid injection protocol and traffic light system to mitigate seismic risks of hydraulic stimulation treatments. *Geothermal Energy*, *6*(1), 27. https://doi.org/10.1186/s40517-018-0114-3

Kaproth, B. M., & Marone, C. (2013). Slow earthquakes, preseismic velocity changes, and the origin of slow frictional stick-slip. *Science*, *341*(6151), 1229–1232. https://doi.org/10.1126/science.1239577

Kim, K.-H., Ree, J.-H., Kim, Y., Kim, S., Kang, S. Y., & Seo, W. (2018). Assessing whether the 2017 M w 5.4 Pohang earthquake in South Korea was an induced event. *Science*, *360*(6392), 1007–1009. https://doi.org/10.1126/science.aat6081

Mahani, A. B., Kao, H., Walker, D., Johnson, J., & Salas, C. (2016). Performance evaluation of the regional seismograph network in northeast british columbia, canada, for monitoring of induced seismicity. *Seismological Research Letters*, *87*(3), 648–660. https://doi.org/10.1785/0220150241

Muntendam-Bos, A. G., Hoedeman, G., Polychronopoulou, K., Draganov, D., Weemstra, C., van der Zee, W., Bakker, R. R., & Roest, H. (2022). An overview of induced seismicity in the Netherlands. *Netherlands Journal of Geosciences*, *101*, e1. https://doi.org/10.1017/njg.2021.14

Oye, V., Anell, I., Braathen, A., Dichiarante, A. M., Evans, J., Hafner, A., Liberty, L., Midtkandal, I., Petrie, E., Sauvin, G., Skurtveit, E., Yelton, J., & Zuchuat, V. (2021). Monitoring and imaging of active and passive CO2 seepage patterns. *SSRN Electronic Journal*. https://doi.org/10.2139/ssrn.3819197

Shreedharan, S., Bolton, D. C., Rivière, J., & Marone, C. (2021). Competition between preslip and deviatoric stress modulates precursors for laboratory earthquakes. *Earth and Planetary Science Letters*, *553*, 116623. https://doi.org/10.1016/j.epsl.2020.116623

Snieder, R., Prejean, S. G., & Johnson, J. B. (2006). Spatial variation in Mount St. Helens clones from coda wave analysis. *Centre for Wave Phenomena Consortium Project 2006*, 247–252. http://www.cwp.mines.edu/Meetings/Project06/cwp543.pdf

van Thienen-Visser, K., & Breunese, J. N. (2015). Induced seismicity of the Groningen gas field: History and recent developments. *The Leading Edge*, *34*(6), 664–671. https://doi.org/10.1190/tle34060664.1

Verdon, J. P., Kendall, J.-M., White, D. J., Angus, D. A., Fisher, Q. J., & Urbancic, T. (2010). Passive seismic monitoring of carbon dioxide storage at Weyburn. *The Leading Edge*, *29*(2), 200–206. https://doi.org/10.1190/1.3304825

Zotz-Wilson, R., Boerrigter, T., & Barnhoorn, A. (2019). Coda-wave monitoring of continuously evolving material properties and the precursory detection of yielding. *The Journal of the Acoustical Society of America*, *145*(2), 1060–1068. https://doi.org/10.1121/1.5091012

5

PRECURSORY SIGNALS TO INJECTION INDUCED FAULT REACTIVATION

Induced earthquakes are still highly unpredictable, and often caused by variations in pore fluid pressure. Monitoring and understanding the mechanisms of fluid-induced fault slip is essential for seismic risk mitigation and seismicity forecasting. Fluid-induced slip experiments were performed on critically stressed faulted sandstone samples, and the evolution of the actively sent ultrasonic waves throughout the experiment was measured. Two different fault types were used: smooth saw-cut fault samples at a 35^o angle, and a rough fault created by in-situ faulting of the samples. Variations in the seismic slip velocity and friction along the fault plane were identified by the coda of the ultrasonic waves. Additionally, ultrasonic amplitudes show precursory signals to laboratory fault reactivation. Our results show that small and local variations in stress before fault failure can be inferred using coda wave interferometry for time-lapse monitoring, as coda waves are more sensitive to small perturbations in a medium than direct waves. Hence, these signals can be used as precursors to laboratory fault slip and to give insight into reactivation mechanisms. Our results show that time-lapse monitoring of coda waves can be used to monitor local stress changes associated with fault reactivation in this laboratory setting of fluid-induced fault reactivation. This is a critical first step towards a method for continuous monitoring of natural fault zones, contributing to seismic risk mitigation of induced and natural earthquakes.

This chapter has been published as Veltmeijer, A., Naderloo, M., Pluymakers, A., & Barnhoorn, A. (2024) *Precursory Signals to Injection Induced Fault Reactivation in the Laboratory using Active Acoustic Ultrasonic Monitoring Methods.* Journal of Geophysical Research: Solid Earth, **129** . Minor modifications have been applied to keep consistency within this thesis

5.1. INTRODUCTION

Forecasting earthquakes has received much interest for many years. Increasing human activities in the subsurface have caused substantial earthquakes in more densely populated areas (e.g., M3.4 Basel (2006), Switzerland, M3.6 Groningen, the Netherlands (2012), and M5.4 Pohang, South Korea (2017)), with serious consequences for subsurface use, halting a geothermal project in Basel, and onshore gas production in Groningen. Thus, effective subsurface monitoring and seismic forecasting are essential to limit the risk and mitigate seismic hazards. In general, the common mechanisms occurring during the seismic cycle are well known (Figure 5.1) (Shreedharan et al., 2021a). This involves initial stress build-up during the inter-seismic phase, during which the fault experiences creep, and fault healing. In the pre-seismic phase the first slip instabilities nucleate where the local stress exceeds the fault strength. This accelerates creep until a seismic event is generated in the co-seismic reactivation phase, during which a large slip event takes place rapidly and stress on the fault is released. In the post-seismic phase, the system will experience creep and renewed fault healing. Currently, natural earthquake forecasts are made using reoccurrence intervals of the seismic cycle, i.e. the average duration of the post-seismic phase (Shimazaki & Nakata, 1980), or using the precursor events during the pre-seismic phase, such as the average earthquake size distribution (b-value) (Gulia et al., 2020). For induced seismicity, forecasting can be done using probabilistic models (Király-Proag et al., 2016; Langenbruch et al., 2018), which can include various production scenarios (Dempsey & Suckale, 2017). In laboratory settings, frictional sliding experimental studies have been performed using passive acoustic monitoring (Cartwright-Taylor et al., 2022; Guglielmi et al., 2015; Noël et al., 2019; Ye & Ghassemi, 2020), mostly to investigate fault mechanics and often to target the onset of the first small and precursory slip events of the pre-seismic phase. However, robust, and reliable predicting of fault failure and the resulting earthquake has proven to be a challenging task (Geller, 1997; Hough, 2009; Kagan & Jackson, 1991; Pritchard et al., 2020), even for experimental faults under controlled laboratory settings (Main & Meredith, 1989).

Pore fluid pressure changes play an important role in the frictional strength and stability of faults and are considered the main trigger for induced seismicity in several real world applications such as hydrocarbon extraction or geothermal energy production (Guglielmi et al., 2015; Kaproth & Marone, 2013; Stanchits et al., 2011; Wang et al., 2020). In contrast to the natural seismic cycle, in these cases instabilities are created locally due to the local pore pressure variations. These cause perturbations in stress magnitude along the fault. Consequently, the pre-seismic phase can arise when the shear strength of the fault plane is exceeded, which then ultimately results in fast shear slip along pre-existing faults and fractures (Wang et al., 2020), i.e. the seismic phase in Figure 5.1. To date, few studies focus on predicting fluid-induced seismicity specifically, and hence, predicting the extent of these pore pressure-induced stress changes, and therefore the potential onset and exact location of failure and seismicity remains very challenging.

Generally speaking, stress changes can be inferred by analyzing the change in acoustic or seismic velocity (Cartwright-Taylor et al., 2022; Xie et al., 2018). For intact rocks, it has been shown that seismic velocities change in response to stress, for example, due to compression of the rocks (Barnhoorn et al., 2018; Winkler & Nur, 1979). In particular, it has been shown that the coda of the acoustic wave traveling through the medium is ex-

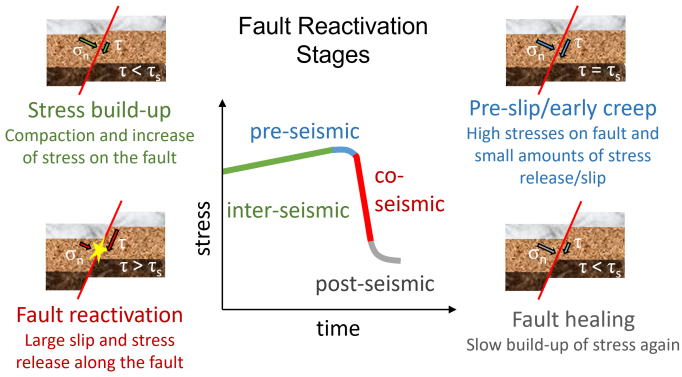

Figure 5.1: Cartoon of fault movement and the corresponding laboratory seismic/ fault reactivation stages. Fault instability and movement occur when the shear stress τ is larger than the shear strength τ_s.

ceptionally sensitive to changes in the microstructure (Snieder et al., 2002; Stähler et al., 2011; Zhang et al., 2012; Zotz-Wilson et al., 2019), where the use of coda wave interferometry can predict the onset of failure before the stress drops in intact rock loaded under a constant rate. However, only a very limited number of laboratory fault sliding studies included continuous active ultrasonic monitoring (Kaproth & Marone, 2013; Passelègue et al., 2018; Shreedharan et al., 2019, 2020, 2021a; Veltmeijer et al., 2023). Moreover, these studies focused only on the elastic wave velocity and changes in amplitude for sliding on smooth faults. Results show precursory changes in elastic wave velocity (Kaproth & Marone, 2013; Passelègue et al., 2018; Veltmeijer et al., 2023) and amplitude (Shreedharan et al., 2019, 2020, 2021a; Veltmeijer et al., 2022) during the pre-seismic phase of fault reactivation (Figure 5.1). However, the relations between these changes in the elastic wave properties and the mechanisms of precursors to failure remain poorly understood. Moreover, it is unknown if monitoring techniques based on arrival time and amplitude would still work for complex, rough fault surfaces, which can be considered more representative of natural fault zones (Frank et al., 2020). Given the success of coda wave interferometry on detecting oncoming failure in intact rocks, we also test the possibilities of coda wave interferometry for monitoring the laboratory seismic cycle with different fluid injection protocols in smooth and rough faults. This chapter aims to monitor slip by identifying precursors from the temporal evolution of ultrasonic seismic waves and to understand the connection between precursors and mechanisms of failure. We present the results of injection-driven reactivation of fault experiments in combination with continuous active ultrasonic monitoring. Fluid pressure was increased cyclically and stepwise to induce slip on the critically stressed saw-cut and in-situ faulted permeable Red-Felser sandstones

5.2. MATERIALS AND METHODS

5.2.1. ROCK SAMPLES

Red Felser sandstones were used in the experiments. These sandstones originate from the Rotliegend formation, which is the same formation as the Groningen reservoir sand-

stones, and are obtained from a quarry near Kaiserslautern, in Germany (Naderloo et al., 2023; van Uijlen, 2013). The rock properties, specifically lithology, porosity, and permeability, of the Red Felser are very similar to the Slochteren sandstone (Eradus, 2019). The intact rock samples have a porosity of 21.4% ± 0.7% and were 30+/-0.1 mm in diameter and 70+/-0.1 mm in length.

5.2.2. EXPERIMENTAL PROTOCOL

The experiments were conducted using a Hoek-cell, a triaxial apparatus (Figure 5.2) which is placed in an in-house built uniaxial loading frame with a 500 kN loadcell. Confining pressure and pore fluid pressure were maintained using an ISCO pump model 100DM. Fluid pressure was imposed at the bottom of the sample but was measured at the top and bottom of the sample. The difference in fluid pressure between top and bottom was within +/-0.2 MPa. We recorded the shortening of the sample using two Solartron AX/1/S linear variable displacement transducers (LVDTs) with a +/-0.1 μm precision. All displacement data was corrected for elastic machine and piston deformation afterward.

Four types of experiments were performed using two fluid injection protocols, namely stepwise and cyclic fluid injection, on smooth and rough faulted samples. By performing multiple repeat tests for the different configurations, the consistency of the acoustic responses has been confirmed. The first sample type has a smooth saw-cut fault, cut at an angle of 35 degrees to the vertical axis (i.e., similar to Ye and Ghassemi, 2020). The tips of the saw-cut plane were slightly rounded to prevent breaking of the edges, resulting in an approximately elliptical fault surface of 45mm +/- 0.7mm in length and 29.6mm

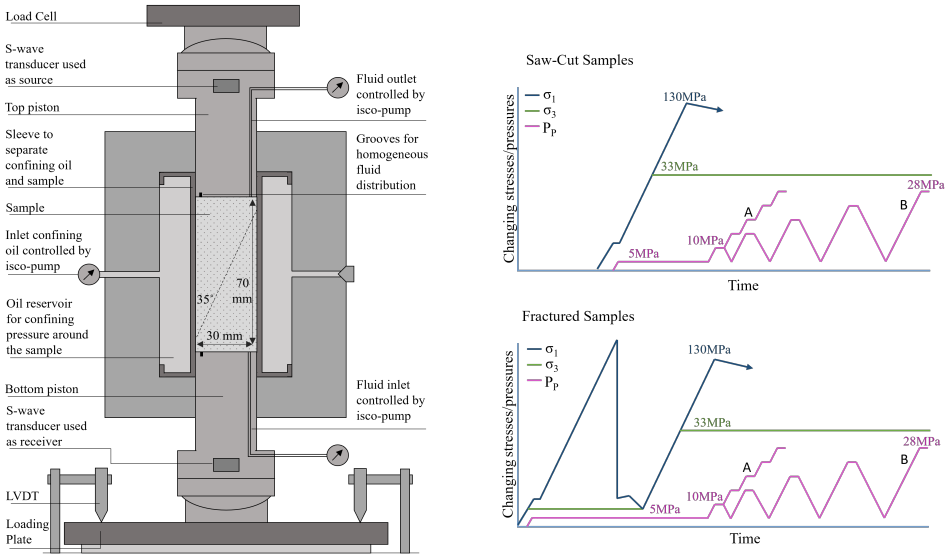

Figure 5.2: Left: Scheme of Hoek-cell used for triaxial experiments (not to scale). Right: scheme of loading and injection protocol for the saw-cut (top) and fractured (bottom) samples. In both cases, protocol A shows stepwise injection and protocol B cyclic injection. The loading plate is fixed during injection, hence the axial stress is allowed to drop during fault reactivation due to fluid injection.

+/- 0.1mm in width (Figure 5.3a). The second sample type has a rough fault created in-situ in the laboratory assembly, which is assumed to be more representative of natural rough faults. Prior to testing, all samples were vacuum-saturated with tap water. For the sample with a rough fault, prior to injection, we fractured an intact sample at 10 MPa confining and 5 MPa fluid pressure. After the fracture was formed, loading of the sample was continued in displacement control for 2 min to eliminate cohesive strength and to slightly open the fracture, to promote slip along the created fracture during the injection stage of the experiment. After creating the rough fault, the experiment proceeded with the same loading and injection protocol as the saw-cut fault samples (Figure 5.2).

Before the fluid injection protocols starts, all faulted samples were stressed to a confining pressure of 33 MPa and 5 MPa fluid pressure. Note that the confining pressure ($\sigma_3 = \sigma_2$) was held constant during the entire experiment. Then the sample was loaded with a constant vertical strain rate of $0.0005s^{-1}$ until the stress-strain curve starts to deviate from linearity (the start of fault reactivation), and reaching a critical stressed condition of the shear stress (τ) (Wang et al., 2020; Ye & Ghassemi, 2020). Here the position of the axial loading press was fixed and held constant. After 10 minutes waiting time, to allow the settling of the sample and assembly, the fluid injection started.

In the first protocol, the stepwise injection (A in Figure 5.2), the fluid pressure was increased stepwise by 5 MPa at a rate of 2 MPa/min with 5 min of waiting time in between each step until the maximum pressure of 28 MPa was reached. In the second protocol, the cyclic injection (B in Figure 5.2), the fluid pressure was returned to the initial pressure of 5 MPa after each increasing step (5 MPa above the previous pressure) of the fluid pressure, and using the same rate of 2 MPa /min but with 3 min waiting time in between each cycle. The fluid pressure was cyclically increased to the same maximum of 28 MPa.

After finishing the experiment, the sample with the created rough fault was removed from the Hoek-cell and scanned in a Nanotom NF180 microCT scanner with a resolution of (voxel size) 64 μm and processed using Avizo software.

Active ultrasonic seismic monitoring was performed on all experiments, simultaneously with the mechanical data acquisition. The waveforms were generated by an Agilent 33210A waveform generator, amplified by an RF Power amplifier, sent and received using Olympus 1MHz/.5" v153 transducers, and finally recorded using a Yokogawa DL9240L

Figure 5.3: Pictures of (dried) samples before (a) and after the experiment was finished (b and c). Note that the tips of the saw-cut are ground off <3 mm, but the overall shape is still elliptical, with dimensions [45mm +/- 0.7mm / 29.6mm +/- 0.1mm]. The middle (b) shows a sample after stepwise injection and the right (c) after cyclic injection. The formed gouge is visible as the patchy whitish powder on the saw-cut fault surface. The patterns of final gouge distribution were different after each experiment, without any relationship to experimental parameters.

oscilloscope. The transducers are integrated into the pistons of the loading system. Two S-wave transducers were used, with the source at the top and the receiver at the bottom of the samples. The transducers were placed such that the polarization of the shear source and receiver was aligned. The peak operating frequency of the S-wave transducers is 1 MHz and the ultrasonic signals were recorded every 3 seconds for 100 μs. To increase the signal-to-noise ratio, every recorded waveform is a stack of 256 S-waves, each sent 4 ms apart (Figure 5.4a).

5.2.3. DATA ANALYSIS

During the experiment, signals were logged for force (N), confining pressure (bar), displacement (μm), pore fluid pressure (bar), wave arrival time (s), and amplitude (volt). The shear stress (τ), friction coefficient (μ), and effective normal stress (σ_n) along the fault plane are determined using the principal stresses, σ_1 and $\sigma_2 = \sigma_3$, derived from the force and confining pressure data respectively, and the fluid pressure (P_f) as given by

$$\mu = \frac{\tau}{\sigma_n - P_f}, \tag{5.1}$$

with,

$$\tau = \frac{\sigma_1 - \sigma_3}{2} \sin 2\alpha, \tag{5.2}$$

and,

$$\sigma_n = \frac{\sigma_1 + \sigma_3 - 2P_f}{2} - \frac{\sigma_1 - \sigma_3}{2} \cos 2\alpha, \tag{5.3}$$

where σ_1 and σ_3 are the axial and radial stress respectively, and α is the fault angle with respect to the vertical (Byerlee, 1967; Wang et al., 2020). The τ and σ_n are corrected for a changing contact area of the fault due to fault slip. The fault slip (s) is determined from the total axial displacement (Δl_{LVDT}), corrected for the displacement of the loading machine (Δl_{MD}), and the rock matrix (Δl_{RM}) (Wang et al., 2020), as follows:

$$s = \frac{\Delta l_{LVDT} - \Delta l_{MD} - \Delta l_{RM}}{\cos \alpha}. \tag{5.4}$$

The displacement of the loading machine (Δl_{MD}) and rock matrix (Δl_{RM}) can be estimated using the stiffness of the machine (K_M) and rock matrix (K_{rock}), and the force drop (F_N), rewriting Equation (5.4) into:

$$s = \frac{\Delta l_{LVDT} - \frac{F_N}{K_M} - \frac{F_N}{K_{rock}}}{\cos \alpha}. \tag{5.5}$$

For the stiffness of the machine and that of the rock matrix we performed a series of calibration experiments using aluminium reference samples and intact rock samples. The recorded waveforms are analysed using the maximum transmitted amplitude of the recorded P- or S-wave as transmissivity $T = |A_{max}|$ (Shreedharan et al., 2020). In addition to the arriving amplitudes, coda wave interferometry (CWI) is used to monitor the velocity change between two recorded waves. The theory of CWI as presented by

Snieder, 2006 states that the unperturbed wavefield u_u(t) can be written as a sum of all possible paths (P) the waves can travel through the medium, where t is time and A_P(t) is the wave along travel path P:

$$u_u(t) = \sum_P A_P(t). \tag{5.6}$$

Each scatterer in the medium is assumed to have stationary properties. Therefore, the scatterer does not change its size, shape, density, and velocity. Additionally, the distance between the individual scatterers is assumed to be much larger than the dominant wavelength (l » λ). The major difference between the wavefields, when the medium changes over time, is the arrival times of the waves propagating along each travel path P. The perturbed wavefield u_p(t) can thus be represented as

$$u_p(t) = \sum_P A_P(t - \delta t_P), \tag{5.7}$$

where δt_P is the travel time change along the path P. This implies that the perturbed wavefield shows only a change in time and does not change the dispersion of the wavefield. By comparing the wave fields the variations in the medium can be assessed. The cross-correlation coefficient is a common measure to quantify these variations. The cross-correlation coefficient (CC) for a time window of width $2t_w$ and centered around time t_k is given by

$$CC(t_s) = \frac{\int_{t_k-t_w}^{t_k+t_w} u_u(t)u_p(t+t_s)dt}{\sqrt{\int_{t_k-t_w}^{t_k+t_w} u_u^2(t)dt \int_{t_k-t_w}^{t_k+t_w} u_p^2(t)dt}}. \tag{5.8}$$

The cross-correlation coefficient (CC) reaches its maximum if the travel time perturbation δt across all possible perturbed paths P is

$$\delta t = t_s. \tag{5.9}$$

The velocity change can be written as the average slope of δt versus t, assuming the time shift is constant in the considered time window, as follows:

$$\frac{\delta v}{v} = -\frac{\delta t}{t_s}. \tag{5.10}$$

To investigate the changes in material scattering, the decorrelation coefficient (K) is determined. The method of coda wave decorrelation (CWD) introduced by Larose et al., 2010 is based on the theory of Snieder, 2006. The decorrelation coefficient is formulated as

$$K(t_s) = 1 - CC(t_s) = 1 - \frac{\int_{t_k-t_w}^{t_k+t_w} u_{p_{j-N}}(t)u_{p_j}(t+t_s)dt}{\sqrt{\int_{t_k-t_w}^{t_k+t_w} u_{p_{j-N}}^2(t)dt \int_{t_k-t_w}^{t_k+t_w} u_{p_j}^2(t)dt}}, \tag{5.11}$$

where N is the number of measurements the reference wavefield u_{p_j-N}(t) is lagging behind the to-be-correlated wavefield u_{p_j}(t) (Figure 5.4b). For continuously monitoring the evolving scattering medium, a moving reference wavefield is used (c.f. Grêt et al.,

2006; Zotz-Wilson et al., 2019). The decorrelation coefficient K is related to the changes in material scattering due to the addition or removal of scatter(ers) in the medium (Planès et al., 2014, 2015). The coda waves seem random due to the complex paths they take through the medium, but the changes they are subjected to are strongly related to the position and strength of the changes in the medium (Planès et al., 2014). The scattering in a medium along the transport mean free path l can be described using the cross-sectional area of a single scatterer V_a and the density of scatterers ρ (Planès et al., 2014). The total scattering coefficient, as described by Aki and Chouet, 1975, is given by

$$g_0 = \rho V_a = l^{-1}. \tag{5.12}$$

Following the theory of Aki and Chouet, 1975, we can rewrite the coda decorrelation in terms of the scattering coefficient (g_0) between a perturbed (p) and unperturbed (u) medium (Zotz-Wilson, 2020).

$$K(t) = \frac{v_0}{2} t|\Delta g_{0_{p-u}}|, \tag{5.13}$$

where $K(t)$ is the theoretical decorrelation coefficient, t the time in the coda, and v_0 the velocity in the medium. Using a rolling reference (N=1), the changes in the absolute value of $|g_0|$ are monitored as a rate of change (e.g., Zotz-Wilson, 2020).

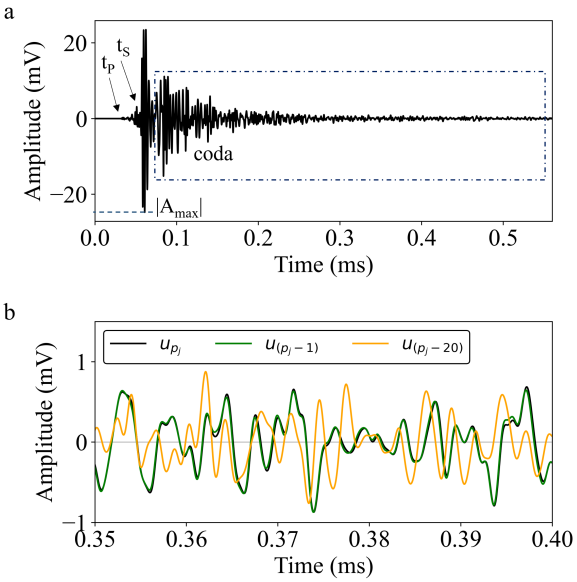

Figure 5.4: Example of a recorded waveform (a) showing the arrival time of the P-wave (t_P) and of the S-wave (t_S) as well as the maximum transmitted amplitude of the S-waves. The length of the coda is indicated by the box and starts at t = $1.5t_S$. Part of the coda is enlarged in (b) to illustrate the shift in the coda over time, showing the to-be-correlated wavefield u_{p_j} (t) and the reference wavefield u_{p_j-N}(t) with N = 1 and 20.

5.3. RESULTS

5.3.1. FAULT SLIP BEHAVIOUR

From the principal stresses, increasing fluid pressures, and area of the fault plane, the evolution of friction coefficient μ is estimated for the saw-cut samples (Eq. 5.1, Figure 5.5a, c, Figure 5.6a, c). It is assumed that the whole fault plane accommodates slip in each event (see a zoomed view of a single step in Figure 5.6a, c). As μ increases during fluid pressurization, frictional strengthening is visible for the two different injection patterns (shaded green in Figure 5.6). At the onset of fault reactivation, μ deviates from linearity (start of yellow shaded area in Figure 5.6) and drops (shaded red in Figure 5.6), simultaneously with the shear stress, when the fault slips. During each slip event (red shaded areas in Figure 5.6 and Figure 5.8), the slip velocity rapidly accelerates to a maximum sliding velocity. Stick-slip events with peak slip velocities below 1 mm/s are defined as slow stick-slip events (Wang et al., 2020). The maximum slip velocities observed are <6.5 μm/s, therefore all recorded slip events in these experiments are slow stick-slip. After reactivation of the fault, μ continues to increase with continued fluid pressurization (shaded blue in Figure 5.6). During this stage, μ is not affected by fault slip, as the fault continues to slip with low background velocities of ≈ 0.8 μm/s. At the end of each injection step, a gradual drop of μ indicates sample relaxation. During the rest in between injection periods, the slip velocity drops to creep velocities near zero ($< 0.1 * 10^{-3}$ μm/s), until a new injection stage starts. In general, the rough fault exhibits very similar behaviour during cyclic injection (Figure 5.5c, d, and Figure 5.7c, d). However, during cyclic injection, the slip events show larger and more abrupt drops in τ, μ, and peaks in slip velocity. But after the slow stick-slip event, similar low background velocities of ≈ 0.8 μm/s are recorded, and in between injection events the rates drop to near zero as well.

The exact area of slip in the rough fault and how it changes during slip is unknown, therefore the evolution of the friction coefficient on the rough fault can't be estimated. However, using the evolution of shear stress and displacement, we can still observe the following. Slow slip is observed along the fault plane with peak velocities well below the velocities observed for slip on a saw-cut fault (Figure 5.9). After the slow slip event reactivation (shaded red in Figure 5.8), sample relaxation causes the slip velocity to drop to creep velocities near zero ($< 0.1 * 10^{-3}$ μm/s) until a new injection stage starts, similar to the saw-cut faults (Figure 5.8). Also on rough faults, the slip velocities are again higher for cyclic than for step-wise injection, however, the difference is less substantial than observed for slip along the saw-cut fault (Figure 5.9). During the last stepwise injection step a large stress drop occurred, and when taking the sample out it had an additional fracture. Therefore, the last step of the stepwise injection needs to be disregarded in the fault slip analysis.

5.3.2. (MICRO-) STRUCTURAL OBSERVATIONS

The fault plane of samples shows damage after the reactivation experiments. Most of the gouge forms during fault slip, due to shear slip, significant grain size reduction took place, resulting in fault gouge formation (Figure 5.3). During sliding, the quartz grains at the surface are crushed, and the resulting fault gouge coats the fault plane upon post-experimental sample retrieval.

In the saw-cut experiments, the contact of the fault plane can be considered relatively smooth and a single contact in macro-scale. On the micro-scale, however, each single grain contact acts as an asperity. This is also shown by the gouge which is distributed heterogeneously on the fault surface, suggesting that even the relatively smooth surface of the saw-cut still has heterogeneous frictional properties across the fault (Figure 5.3). Each experiment comes out with its own distinct pattern of gouge distribution, without obvious correlation to the experimental parameters.

After finishing the experiment with a rough fault experiments, a CT image (Figure 5.11) was made to show slices of the fault plane after finishing the experiment. Along the fault plane, black areas are visible, indicating open pore space. There are also intermediately shaded grey areas, where the fault plane is harder to track. Image segmentation by simple thresholding shows the approximate 3D view of the fault plane. It shows a very irregular fault surface (Figure 5.12c), which forms a stark contrast to the simple and straight saw-cut planes.

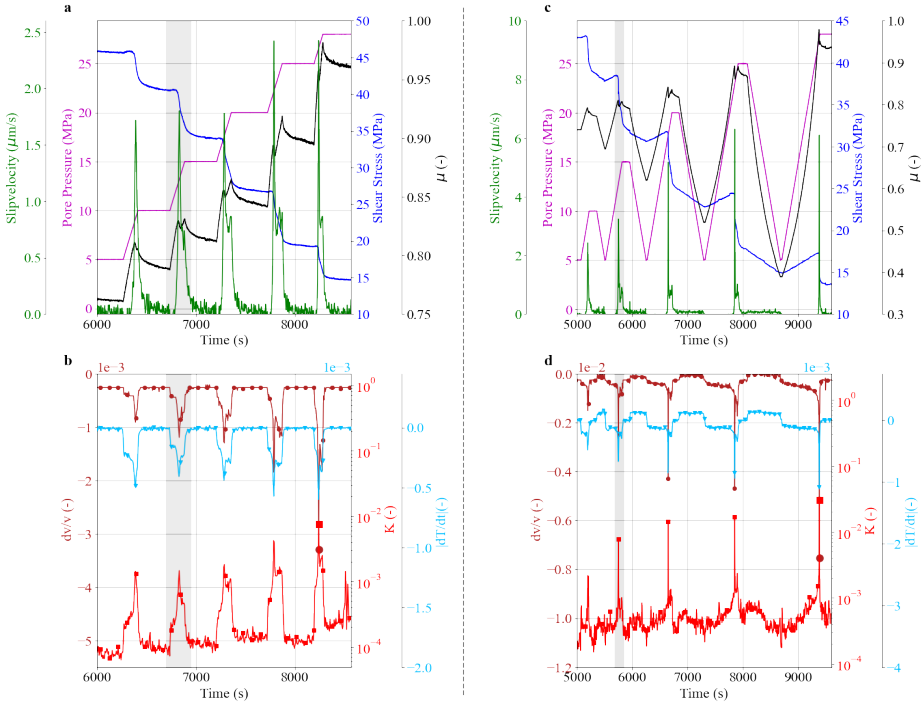

Figure 5.5: Evolution of mechanical and acoustic parameters during the reactivation of the saw-cut samples. a and b show the results of the stepwise injection experiment. c and d show the results of the cyclic injection experiment. a and c show the evolution of the shear stress τ, friction coefficient μ, and slip velocity along the fault due to increasing pore pressure. b and d show the derivative of the transmissivity T and the evolution of coda wave parameters K and dv/v. Slip event shaded in grey zoomed view visible in Figure 5.6.

5.3.3. ULTRASONIC MONITORING

We first describe the results of the saw-cut experiments. Monitoring the evolving transmissivity T, a measure of the transmitted amplitude, was previously used by Nagata et al., 2008 and Shreedharan et al., 2021a to track fault properties in direct shear experimental setting, without considering the effects of pore pressure. It is known that pore pressure has a large effect on the transmission of wave energy (Winkler & Nur, 1979). This is also observed in this set of experiments, in which was observed that transmitted amplitudes decrease and increase inversely with pore pressure. To investigate the more subtle changes due to fault reactivation, the derivative of T is plotted (Figure 5.5b, d, Figure 5.6b, d). This shows that during fault slip there is an accelerated drop in the transmitted amplitude. During each slip event the sample is shortened, decreasing the direct travel path of the wave, which should increase the amplitude. However, the transmissivity decreases with each injection step instead, and exhibits a faster rate during slip. We observed gouge formation during experiments with slip. Theoretically, a thicker gouge layer should attenuate waveforms travelling through the sample more than a thinner gouge layer. Given that the transmissivity still shows a decrease during cyclic injection, even while the pore pressure was returned to the initial pressure and including the short-

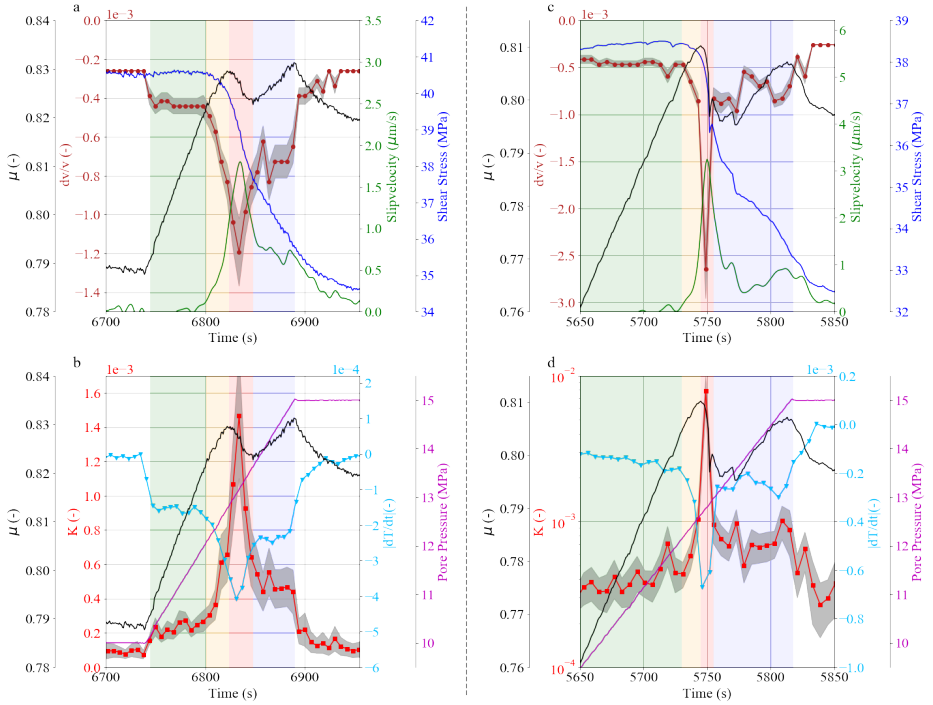

Figure 5.6: Zoom of single slip events (shaded grey in Figure 5.5) a and b showing the evolution of mechanical and acoustic parameters during the reactivation of the saw-cut samples of the second slip event induced by stepwise injection experiment and c and d the second slip event induced by cyclic injection experiment. The shaded grey around the decorrelation coefficient K shows the standard deviation and the coloured shaded areas in figures a to d indicate the four stages of fault reactivation, green: inter-seismic stage, yellow: pre-seismic stage, red: co-seismic stage, and blue: post-co-seismic stage.

ening of the sample due to slip, we infer this decrease to be due to additional attenuation by ongoing gouge formation.

The small stress variations along the fault plane are interpreted and assessed by comparing the coda of the recorded wave fields, where a moving reference wavefield was used (t_{N-1}–t_N). Therefore the decorrelation coefficient K and velocity change dv/v are monitored as a rate of change. Coda wave parameters K and dv/v respond to fluid injection, and increase and decrease in conjunction with the injection pattern, showing their sensitivity to stress perturbation on the sample scale (Figure 5.5b and d, Figure 5.6b, d). Within this background response to the change in sample stress during injection, another trend is visible. The evolution of coda wave parameters K and dv/v show a strong correlation to the slip velocity, with an accelerating increase before slip (yellow shaded areas in Figure 5.6), an obvious peak during slip (red shaded areas in Figure 5.6), and a reduction to background levels at moments of relaxation. The magnitude of these peaks increases per cycle (Figure 5.5b, d) similar to the slip velocity (Figure 5.5a, c). This indicates that dv/v and K are indeed sensitive to the slip velocity along the saw-cut fault plane. As fault slip is a result of stress changes and the resulting loss of asperity contact along the fault plane, we infer the changes in dv/v and K are results of changes in fault contact on the microscale. T shows a similar trend to dv/v, showing an equivalent

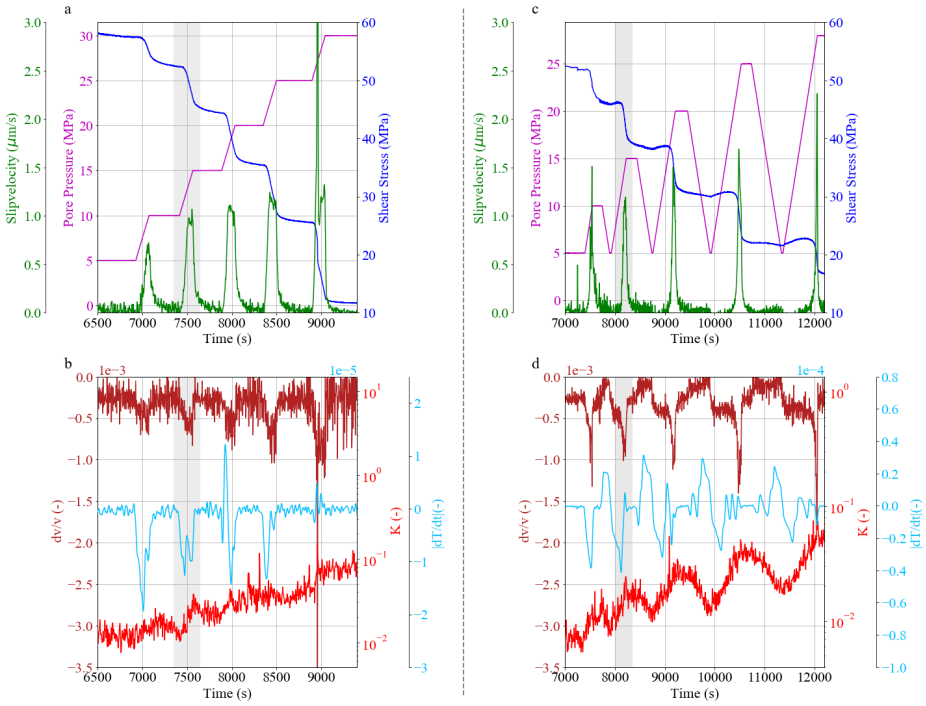

Figure 5.7: Evolution of mechanical and acoustic parameters during the reactivation of fractured samples, or rough fault. a and b show the results of the stepwise injection experiment. c and d show the results of the cyclic injection experiment. a and c show the evolution of the shear stress τ, friction coefficient μ, and slip velocity along the fault due to increasing pore pressure. b and d the derivative of the transmissivity T and the evolution of coda wave parameters K and dv/v. The slip event is shaded in grey, zoomed view visible in Figure 5.8.

sensitivity to the stress changes along a saw-cut fault.

Moving to the more complex situation of the rough fault, we observe that for the rough fault, the T pattern changes per slip event (Figure 5.7b, d). Rather than decreasing amplitudes prior to slip (Figure 5.6b, d), increasing amplitudes in the transmitted waves are observed during and just before slipping along the rough fault (Figure 5.7b, d). A similar observation can be made for coda parameter K (Figure 5.7b, d and Figure 5.8b, d). The scattering along the more uneven slip along the rough fault causes an incoherent signal from the decorrelation coefficient K (Figure 5.7b, d). While the general sample scale pattern of fluid injection is still visible (Figure 5.7d), the more subtle trend with accelerated increase during fault reactivation (observed in the saw-cut faults; shaded yellow in Figure 5.6b, d) is lost by the more complicated slip along the rough fault plane (Figure 5.7b, d). Nonetheless, the velocity change dv/v, however, is still showing the same trends with slip velocity (Figure 5.8a, c). This suggests that the velocity change obtained by the coda wave, which sampled the fault, still is a promising indicator for the pre-slip and slip phase along the rough fault plane (shaded yellow and red respectively in Figure 5.8a, c).

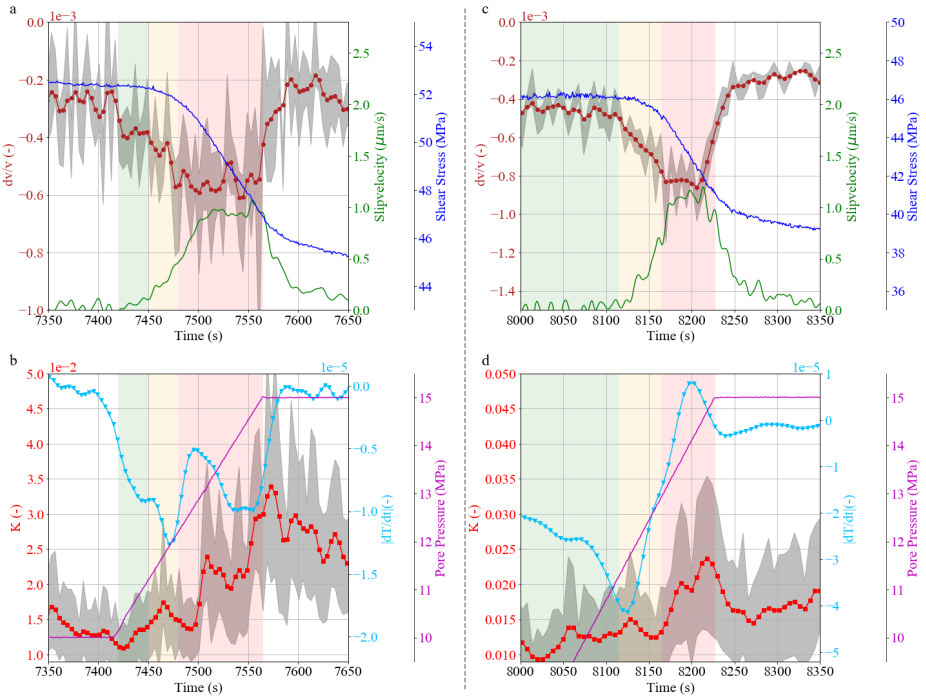

Figure 5.8: Zoom of single slip events (shaded grey in Figure 5.7). a and b showing the evolution of mechanical and acoustic parameters during the reactivation of fractured samples, or rough fault of the second slip event induced by stepwise injection experiment and c and d the second slip event induced by cyclic injection experiment. The shaded grey around the decorrelation coefficient K shows the standard deviation and the coloured shaded areas in figures a to d indicate the four stages of fault reactivation, green: inter-seismic stage, yellow: pre-seismic stage, red: co-seismic stage.

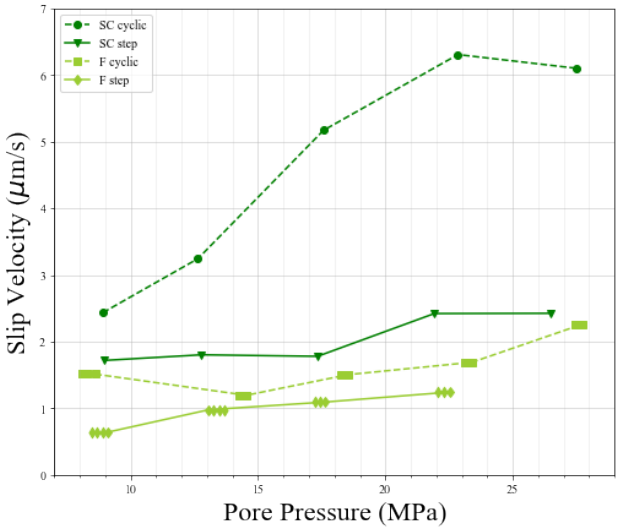

Figure 5.9: Peak slip velocity for each injection (stepwise and cyclic) step for the saw-cut (SC) and fractured (F) samples. The co-seismic phase for the rough fault (fractured samples) is more prolonged, the markers show the potential start of the co-seismic phase whereas in the SC samples the peak in velocity coincides with the co-seismic phase.

5.4. DISCUSSION

In the following, we will discuss the effect of injection pattern on fault reactivation and measured waveforms. Then we go on to discuss the difference of the effectiveness of ultrasonic monitoring for smooth versus rough faults, where we presume that the type of roughness created by the faulting procedure is more representative for in-situ roughness. Following, we will discuss the added benefit of using coda wave interferometry to determine precursors to fault reactivation, and finally, we will discuss the implications of our results for earthquake predictions.

5.4.1. EFFECT OF INJECTION PATTERN

By stepping or cycling the pore pressure, fault instability is reached multiple times. In each cycle or step, when pore pressure stops increasing, we allow the system to re-stabilize and reach a new equilibrium. By reducing the pore pressure each cycle, the fault plane can relax and build strength caused by the compaction of the fault due to an increased effective normal stress. (Figure 5.10). In cycles where pore pressure is reduced the fault compacts further, and subsequently, more energy is needed to reactivate the fault. This corresponds to an increase in the fault energy release, as observed by increasing slip velocities in cyclic injection (Figure 5.9).

In the faulted samples, the grains on the fault surface are crushed during sliding and pressuring of the fault, creating a gouge layer along the fault surface. This changes the fault properties like the friction coefficient, which in the quartz-rich Red Felser sandstone, would be expected to have a frictional strengthening effect (Bakker et al., 2016; He et al., 2013). We do observe continuous restrengthening of the fault throughout the

experiment (Figure 5.10). Most of the gouge is expected to form just prior to and during fault slip, when we expect to have the highest local stresses on the asperities and movement, causing the observed grain size reduction (Figure 5.3). Seismic waves are increasingly attenuated and scattered due to the gouge formation and due to the changes in stress and movement and repositioning of the scatterers along the fault. These changes were used as a precursor to fault reactivation during ultrasonic monitoring.

The peaks of decorrelation coefficient K, a proxy for the scattering coefficient (Eq. 5.12,5.13), during slip can be explained by an increased addition of scatterers, caused by the fracturing, crushing and movement of the grains along the surface area of the fault plane forming a progressively thicker gouge layer. The creation of this layer along with stress release during slip also causes the drop in velocity dv/v, and the transmitted amplitude T during fault reactivation. Both parameters peak during fault slip, afterward they are fluctuating around a constant rate, similar to the observed constant slow slip (Figure 5.5b, d). The slow stick-slip events induced by cyclic injection have a greater amplitude and are more abrupt than for stepwise injection due to a greater release of fault energy (Figure 5.5b, d and Figure 5.6b, d). This results in larger amplitudes in the coda wave parameters K and dv/v, but also fewer sampling points per slip event.

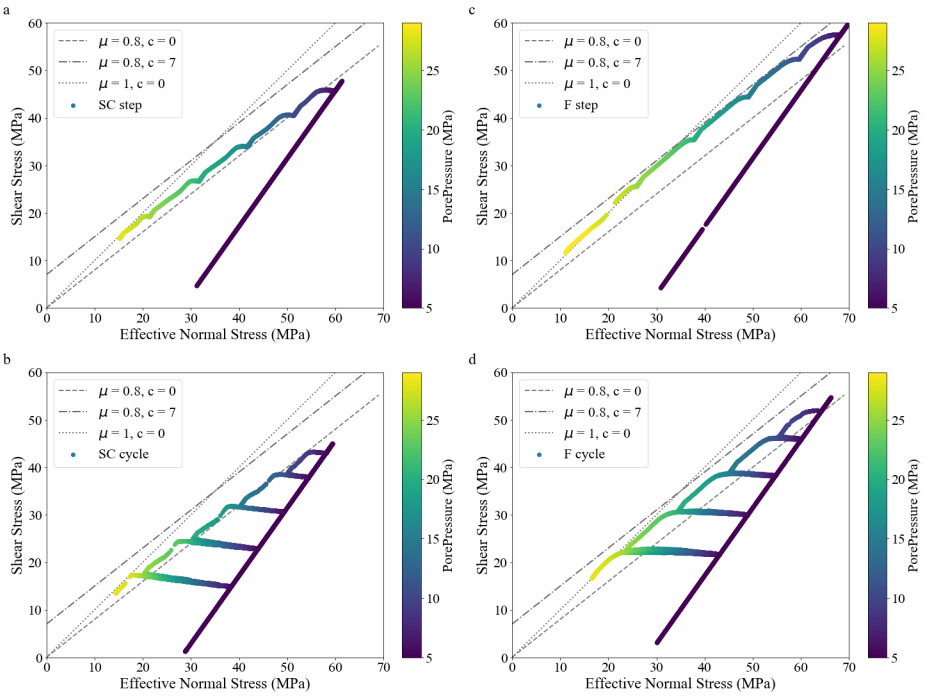

Figure 5.10: Showing the relation between the principal stresses on the fault plane 'colour coded' by the applied pore pressure; a) for the saw-cut stepwise injection experiment; b) for the saw-cut stepwise cyclic experiment; c-d; for the fractured samples stepwise and cyclic injection protocol respectively. Indicative failure envelopes are drawn for failure planes with friction coefficient μ is 0.8 or 1 and cohesion c is 0 or 7.

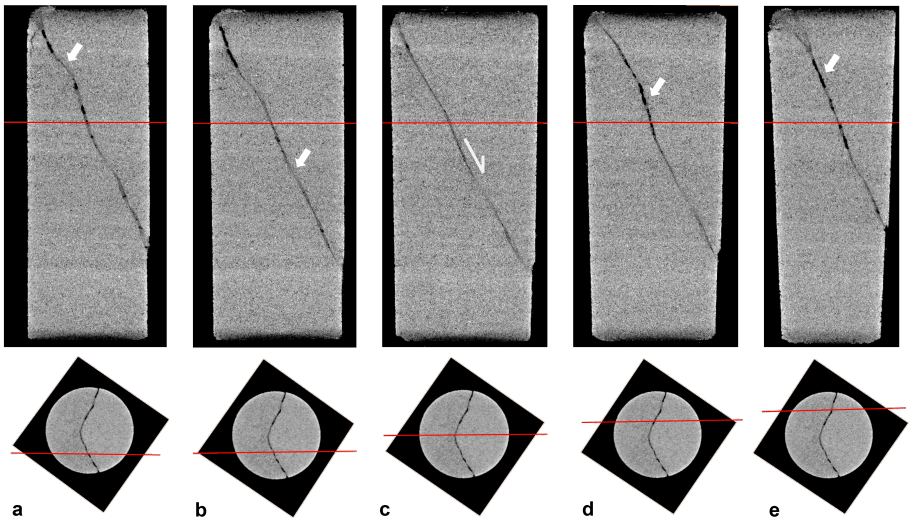

Figure 5.11: CT sections cutting through the fault plane, showing the irregular shape of the rough fault plane. Arrows point at the black areas, which indicate areas of more pore space, hence opening of the fault, and to more greyish blurry areas, which show the interlocking and compaction areas along the fault. The red lines show the horizontal and vertical position of the slices. The movement along the fault plane is caused by downward sliding of the top half of the sample. The white arrows indicate areas of compaction (a and b) and areas of opening (d and e). The direction of movement is indicated in c.

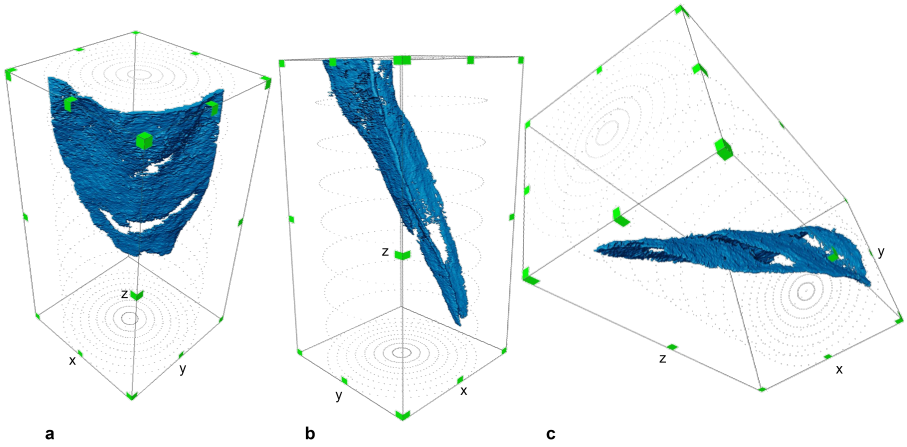

Figure 5.12: Image of the fault area, extracted from the CT images. This shows the irregular shape of the rough fault plane. The gaps are stronger compaction areas of fault, which weren't picked up in processing of the fault area in the CT scans. C shows a jump in the fault plane after an area of compaction.

5.4.2. EFFECT OF ROUGHNESS

The roughness of the fault plane illustrated by the CT image (Figure 5.11), implies the fault plane has multiple areas of compaction (Figure 5.11a, b), where interlocking of asperities can occur, and areas of opening (Figure 5.11d, e). During slip, parts of such a rough fault can lock, and the fault will locally compact, whereas it will dilate locally there where the two halves move apart. Both phenomena could enhance resistance to shear along the fault by interlocking asperities or dilatant hardening (Rudnicki & Chen, 1988). This increased cohesion of the fault (Figure 5.10b, d) and resistance to shear result in more prolonged slow slip (Figure 5.8a, c) upon reactivation until the fluid injection is stopped in which we observe fluctuating slip velocities, suggesting the overcoming of the interface locking. In contrast, the saw-cut fault is smooth and could therefore slip more easily in its entirety once fault instability is reached. Accordingly, we observe higher slip velocities (Figure 5.9) upon reactivation and a short and larger stress drop (Figure 5.6a, c), indicating short and fast reactivation with afterward continuous slow slip phase due to continued elevated pore pressure and reduced effective normal stress reducing the interface locking along the smooth fault (Alghannam & Juanes, 2020).

The effect of compaction and dilation along the rough fault can be discerned in the ultrasonic data. Compaction will cause increasing acoustic amplitudes, whereas dilation causes more attenuation of the waves and lower transmissivity. This interpretation is consistent with the systematic differences in the increasing and decreasing behaviour of T prior to fault reactivation (Figure 5.7b, d) of the rough fault. Where the decreasing behaviour of T during fault reactivation of the smooth fault (Figure 5.5b,d) suggests the detection of dilation along the fault plane, its increase suggests the detection of compaction. The scattering along the more uneven slip along the rough fault causes a more incoherent signal from the K (Figure 5.7b, d). While the general pattern of fluid injection is still visible (Figure 5.7d), the more subtle trend of fault reactivation is lost by the more complicated slip along the rough fault plane (Figure 5.8b, d). Cartwright-Taylor et al., 2022 described crack rotation with antithetic slip as an additional mechanism for local stress rotation and slip, allowing shear along more unfavourably-orientated faults, which among fracturing and crushing of the grains influence the scattering, therefore causing a more incoherent K compared to sliding along the smooth fault surface, where we won't expect this fault rotation and antithetic slip.

5.4.3. PRECURSORS TO FAULT REACTIVATION

The direct shear experiments by Shreedharan et al., 2021a suggest a physical connection between ultrasonic evolution (amplitude and direct wave velocity) and variations in healing, pre-slip driven asperity changes, and shear stiffening of wallrock. Their results, similar to ours, suggested as well that the destruction of asperities and increase in fracture density due to stress changes along the fault during and prior to fault slip is expected to result in reduction in transmitted amplitude T and P-wave velocity. However, the work done by Shreedharan et al., 2021a lacked the additional layer of complexity introduced by the presence of pore pressure variations. Research by Passelègue et al., 2018; Winkler and Nur, 1979, indicates that ultrasonic amplitude and velocity are influenced by pore pressure. In this chapter and in Veltmeijer et al., 2022, we observe that pore pressure increases have a large effect on the transmitted amplitude, emphasizing the importance

of considering relative changes in transmissivity to infer the nuance introduced by small variations in healing and interface locking along the fault.

The presented slip velocities can be categorized as slow slip (<6.5μm) or creeping velocities ($< 0.1 * 10^{-3}\mu$m) (Figure 5.5 and Figure 5.7). These velocities are commonly thought to be aseismic. However, experiments shown by Veltmeijer et al., 2023; Wang et al., 2020; Ye and Ghassemi, 2020 show recorded micro seismic events with similar slow slip velocities. Hence, some seismic energy has been released, and we will characterize the fault reactivation according to the fault reactivation stages (Figure 5.1). By analysing the temporal evolution of the coda waves, stress changes on the fault surface can be identified, demonstrating the potential of coda waves to identify the stages of fault reactivation: inter-seismic phase: linear stress build-up, the pre-seismic phase: early creep/pre-slip, the co-seismic phase: stress drop and a continuous sliding phase for the saw cut fault planes followed by a post-seismic phase at the end of injection: fault healing (i.e. following the terminology and sequence shown in Figure 5.1). Our results show that we can identify the pre-seismic phase of laboratory injection-induced fault slip. By zooming on a single step or cycle, the K, dv/v, and T can be used to identify the different stages of reactivation. dv/v reaches a new equilibrium after the start of injection (Figure 5.6 and Figure 5.8), this can also be observed in the K and T for the reactivation of the saw-cut fault. The linear stress build-up along the fault causes a constant drop in velocity following the fluid pressure identifying as the inter-seismic phase (green shaded area in Figure 5.6 and Figure 5.8). Once the fault plane starts to become unstable in the pre-slip phase (yellow shaded area in Figure 5.6 and Figure 5.8) the dv/v, K, and T show an accelerated decrease/increase in values (Figure 5.6) peaking at the co-seismic stage (red shaded area in Figure 5.6 and Figure 5.8). These early changes in values deviate from the change caused by increased pore pressure and are hence a proxy of the stress change along the fault plane. Detecting the pre-slip phase could be a first step for forecasting the upcoming fault reactivation as it is an indication of the upcoming co-seismic slip phase.

The drop in dv/v occurs over a narrow range, as well as the standard deviation indicated in grey, hence it gives a fairly accurate indication of both the preparatory phase and fault reactivation (Figure 5.6b). Due to the smooth fault, the stress release and fault reactivation are rapid, and hence the preparatory phase is short. To reactivate the rough fracture, more energy is needed, as some parts of the fracture aren't favourably oriented to move (Figure 5.11). During this extended preparatory phase, the drop in velocity remains clear and shows the same pattern (Figure 5.6d), albeit a more noisy one due to the more complex fault area. Using CWD, the decorrelation coefficient K, a proxy for grain crushing or movement, is determined. This K clearly indicated the saw-cut fault reactivation, however, when the fault plane becomes more complex, the K seems to be of little use in detecting both the preparatory phase and fault reactivation (Figure 5.8c, d). A similar conclusion can be drawn from the transmissivity. T in the rough fault initially showed patterns similar to the saw-cut fault reactivation for the first injection step/cycle, but the later steps differ. Even though monitoring of fault reactivation is more complex, and the signal is noisier for the rough fault, using the dv/v, the pre-slip and co-seismic phase of fault reactivation can still be determined. Due to the more prolonged pre-slip phase, the forecast of the co-seismic stage can be done earlier as higher differential stresses are needed to reactivate the rough fault.

After the co-seismic stage, post-slip sliding is observed in the saw-cut reactivated faults. As the fault remains prone to sliding due to continued fluid injection the fault plane continues to slowly slip until fluid injection ends (Figure 5.6). No post-slip during the injection is observed as the rough fault continues to slip slowly (Figure 5.8), rather than showing a short and rapid co-seismic phase (as happened for the smooth faults). Once injection stops, the fault is not perturbed anymore, which signifies the start of the post-seismic phase, during which the fault relaxes and can heal until the next step in the injection protocol starts.

5.4.4. IMPLICATIONS FOR INDUCED SEISMICITY

In our constrained laboratory setting, we accurately identified the pre-slip phase using a combination of parameters, including transmitted amplitude, and CWI parameters, highlighting that velocity changes obtained from coda offer more precision in complex situations compared to the amplitudes. This suggests the potential inclusion of coda wave interferometry in forecasting fault reactivation, presenting an improvement for input in forecasting models. Efforts, including machine learning models, have been made to improve predictions of lab quakes (Laurenti et al., 2022; Rouet-Leduc et al., 2017; Wang et al., 2022), also including transmitted amplitudes to the models (Shreedharan et al., 2021b).

Upscaling these findings to real reservoir remains a challenge, even though pre- seismic crustal velocity anomalies have been observed for a limited number of earthquakes (Chiarabba et al., 2020; Niu et al., 2008). More work is needed to verify the usefulness of the results for upscaled fault zone length, maturity, time, and complexity and extent of the damage zone. From the engineering perspective it would require work on placement of monitoring stations and monitoring frequency. Due to the fast nature of fault reactivation in the laboratory, with pre- and co-seismic phases lasting seconds, monitoring points during the pre-slip phase are limited due to equipment constraints. Nevertheless, assuming a one-to-one relationship between the laboratory and field scale, we do see potential in this method for monitoring fault reactivation. In the laboratory, the pre-slip phase spans only a few seconds, equivalent to a 5 MPa increase in pore pressure (or a 5 MPa decrease in effective stress). Extrapolating this to the field, a similar pore pressure change may take several days to weeks or more to build-up after which reactivation occurs. This potentially would allow more time for measurements and forecasting. Our work is performed in a carefully constrained laboratory setting, and does not take in account temperature, maturity or forward prediction of fault reactivation. We encourage future experimental research in these directions as well as upscaling and field applicability.

5.5. CONCLUSIONS

In this chapter, we aim to monitor fluid-induced fault slip in laboratory experiments more accurately and understand the connection between precursors and mechanisms of failure. By analysing the temporal evolution of the coda waves and seismic amplitudes, stress changes on the fault surface can be identified, demonstrating the potential of coda waves to identify the stages of fault reactivation as a possible basis for forecasting

injection-induced fault-slip. The precursory signals obtained by coda wave interferometry and decorrelation are compared for both a smooth saw-cut and rough fault.

It is shown that the CWI velocity change is most sensitive to the pre-slip phase and fault reactivation. However, as all the compared attributes are obtained from the same wavelet a combination of these properties shows that the stress changes along the fault can be inferred with more accuracy. As a result, the combination may be useful for monitoring faulted or critically stressed reservoirs that experience pore pressure changes.

The coda analysis and amplitudes are used to identify the different stages in the laboratory seismic cycle, as precursors to fault slip and to give insight into reactivation mechanisms. Showing ultrasonic monitoring techniques can be used to detect the different fault reactivation stages: inter-seismic phase: linear stress build-up, the pre-seismic phase: early creep/pre-slip, the co-seismic phase: stress drop and a continuous sliding phase for the saw cut fault planes followed by a post-seismic phase at the end of injection: fault healing.

Our experiments demonstrate the feasibility of active ultrasonic monitoring as a tool to identify precursors to laboratory fluid-induced earthquakes. While these experiments show the feasibility of the active monitoring method in a controlled environment in the laboratory, and its potential to infer the pre-seismic phase, it does not yet include the forward forecasting. The timing of the pre-phase, from detection to forward forecasting and the added complexity from lab to field-scale should still be studied. The potential to infer aseismic stress changes pointing toward seismicity from active ultrasonic campaigns could be of added value to monitoring and forecasting (models).

REFERENCES

Aki, K., & Chouet, B. (1975). Origin of coda waves: Source, attenuation, and scattering effects. *Journal of Geophysical Research, 80*(23), 3322–3342. https://doi.org/10.1029/jb080i023p03322

Alghannam, M., & Juanes, R. (2020). Understanding rate effects in injection-induced earthquakes. *Nature Communications, 11*(1), 1–6. https://doi.org/10.1038/s41467-020-16860-y

Bakker, E., Hangx, S. J., Niemeijer, A. R., & Spiers, C. J. (2016). Frictional behaviour and transport properties of simulated fault gouges derived from a natural CO2 reservoir. *International Journal of Greenhouse Gas Control, 54*, 70–83. https://doi.org/10.1016/j.ijggc.2016.08.029

Barnhoorn, A., Verheij, J., Frehner, M., Zhubayev, A., & Houben, M. (2018). Experimental identification of the transition from elasticity to inelasticity from ultrasonic attenuation analyses. *Geophysics, 83*(4), MR221–MR229. https://doi.org/10.1190/geo2017-0534.1

Byerlee, J. D. (1967). Frictional characteristics of granite under high confining pressure. *Journal of Geophysical Research, 72*(14), 3639–3648. https://doi.org/10.1029/JZ072i014p03639

Cartwright-Taylor, A., Mangriotis, M. D., Main, I. G., Butler, I. B., Fusseis, F., Ling, M., Andò, E., Curtis, A., Bell, A. F., Crippen, A., Rizzo, R. E., Marti, S., Leung, D. D., & Magdysyuk, O. V. (2022). Seismic events miss important kinematically governed

grain scale mechanisms during shear failure of porous rock. *Nature Communications*, *13*(1). https://doi.org/10.1038/s41467-022-33855-z

Chiarabba, C., De Gori, P., Segou, M., & Cattaneo, M. (2020). Seismic velocity precursors to the 2016 Mw 6.5 Norcia (Italy) earthquake. *Geology*, *48*(9), 924–928. https://doi.org/10.1130/G47048.1

Dempsey, D., & Suckale, J. (2017). Physics-based forecasting of induced seismicity at Groningen gas field, the Netherlands. *Geophysical Research Letters*, *44*(15), 7773–7782. https://doi.org/10.1002/2017GL073878

Eradus, D. (2019). *Petrographical description and petrophysical measurements on the red felser sandstone* [BSc Thesis]. Delft University of Technology.

Frank, S., Heinze, T., & Wohnlich, S. (2020). Comparison of surface roughness and transport processes of sawed, split and natural sandstone fractures. *Water (Switzerland)*, *12*(9). https://doi.org/10.3390/w12092530

Geller, R. J. (1997). Earthquake prediction: a critical review. *Geophysical Journal International*, *131*(3), 425–450. https://doi.org/10.1111/j.1365-246x.1997.tb06588.x

Grêt, A., Snieder, R., & Scales, J. (2006). Time-lapse monitoring of rock properties with coda wave interferometry. *Journal of Geophysical Research: Solid Earth*, *111*(3), 1–11. https://doi.org/10.1029/2004JB003354

Guglielmi, Y., Cappa, F., Avouac, J. P., Henry, P., & Elsworth, D. (2015). Seismicity triggered by fluid injection-induced aseismic slip. *Science*, *348*(6240), 1224–1226. https://doi.org/10.1126/science.aab0476

Gulia, L., Wiemer, S., & Vannucci, G. (2020). Pseudoprospective evaluation of the foreshock traffic-light system in ridgecrest and implications for aftershock hazard assessment. *Seismological Research Letters*, *91*(5), 2828–2842. https://doi.org/10.1785/0220190307

He, C., Luo, L., Hao, Q. M., & Zhou, Y. (2013). Velocity-weakening behavior of plagioclase and pyroxene gouges and stabilizing effect of small amounts of quartz under hydrothermal conditions. *Journal of Geophysical Research: Solid Earth*, *118*(7), 3408–3430. https://doi.org/10.1002/jgrb.50280

Hough, S. E. (2009). *Predicting the unpredictable*. Princeton University Press. https://doi.org/10.1515/9781400883547

Kagan, Y. Y., & Jackson, D. D. (1991). Seismic gap hypothesis: Ten years after. *Journal of Geophysical Research: Solid Earth*, *96*(B13), 21419–21431. https://doi.org/10.1029/91JB02210

Kaproth, B. M., & Marone, C. (2013). Slow earthquakes, preseismic velocity changes, and the origin of slow frictional stick-slip. *Science*, *341*(6151), 1229–1232. https://doi.org/10.1126/science.1239577

Király-Proag, E., Zechar, J. D., Gischig, V., Wiemer, S., Karvounis, D., & Doetsch, J. (2016). Validating induced seismicity forecast models—induced seismicity test bench. *Journal of Geophysical Research: Solid Earth*, *121*(8), 6009–6029. https://doi.org/10.1002/2016JB013236

Langenbruch, C., Weingarten, M., & Zoback, M. D. (2018). Physics-based forecasting of man-made earthquake hazards in Oklahoma and Kansas. *Nature Communications*, *9*(1), 1–10. https://doi.org/10.1038/s41467-018-06167-4

Larose, E., Planes, T., Rossetto, V., & Margerin, L. (2010). Locating a small change in a multiple scattering environment. *Applied Physics Letters*, *96*(20), 1–4. https://doi.org/10.1063/1.3431269

Laurenti, L., Tinti, E., Galasso, F., Franco, L., & Marone, C. (2022). Deep learning for laboratory earthquake prediction and autoregressive forecasting of fault zone stress. *Earth and Planetary Science Letters*, *598*, 117825. https://doi.org/10.1016/j.epsl.2022.117825

Main, I. G., & Meredith, P. G. (1989). Classification of earthquake precursors from a fracture mechanics model. *Tectonophysics*, *167*(2-4), 273–283. https://doi.org/10.1016/0040-1951(89)90078-4

Naderloo, M., Veltmeijer, A., Jansen, J. D., & Barnhoorn, A. (2023). Laboratory study on the effect of stress cycling pattern and rate on seismicity evolution. *Geomechanics and Geophysics for Geo-Energy and Geo-Resources*, *9*(1), 1–18. https://doi.org/10.1007/s40948-023-00678-1

Nagata, K., Nakatani, M., & Yoshida, S. (2008). Monitoring frictional strength with acoustic wave transmission. *Geophysical Research Letters*, *35*(6), 1–5. https://doi.org/10.1029/2007GL033146

Niu, F., Silver, P. G., Daley, T. M., Cheng, X., & Majer, E. L. (2008). Preseismic velocity changes observed from active source monitoring at the Parkfield SAFOD drill site. *Nature*, *454*(7201), 204–208. https://doi.org/10.1038/nature07111

Noël, C., Passelègue, F. X., Giorgetti, C., & Violay, M. (2019). Fault reactivation during fluid pressure oscillations: transition from stable to unstable slip. *Journal of Geophysical Research: Solid Earth*, *124*(11), 10940–10953. https://doi.org/10.1029/2018JB016045

Passelègue, F. X., Brantut, N., & Mitchell, T. M. (2018). Fault reactivation by fluid injection: controls from stress state and injection rate. *Geophysical Research Letters*, *45*(23), 12, 837–12, 846. https://doi.org/10.1029/2018GL080470

Planès, T., Larose, E., Margerin, L., Rossetto, V., & Sens-Schönfelder, C. (2014). Decorrelation and phase-shift of coda waves induced by local changes: Multiple scattering approach and numerical validation. *Waves in Random and Complex Media*, *24*(2), 99–125. https://doi.org/10.1080/17455030.2014.880821

Planès, T., Larose, E., Rossetto, V., & Margerin, L. (2015). Imaging multiple local changes in heterogeneous media with diffuse waves. *The Journal of the Acoustical Society of America*, *137*(2), 660–667. https://doi.org/10.1121/1.4906824

Pritchard, M. E., Allen, R. M., Becker, T. W., Behn, M. D., Brodsky, E. E., Bürgmann, R., Ebinger, C., Freymueller, J. T., Gerstenberger, M., Haines, B., Kaneko, Y., Jacobsen, S. D., Lindsey, N., McGuire, J. J., Page, M., Ruiz, S., Tolstoy, M., Wallace, L., Walter, W. R., ... Vincent, H. (2020). New opportunities to study earthquake precursors. *Seismological Research Letters*, *91*(5), 2444–2447. https://doi.org/10.1785/0220200089

Rouet-Leduc, B., Hulbert, C., Lubbers, N., Barros, K., Humphreys, C. J., & Johnson, P. A. (2017). Machine learning predicts laboratory earthquakes. *Geophysical Research Letters*, *44*(18), 9276–9282. https://doi.org/10.1002/2017GL074677

Rudnicki, J. W., & Chen, C. H. (1988). Stabilization of rapid frictional slip on a weakening fault by dilatant hardening. *Journal of Geophysical Research*, *93*(B5), 4745–4757. https://doi.org/10.1029/JB093iB05p04745

Shimazaki, K., & Nakata, T. (1980). Time-predictable recurrence model for large earthquakes. *Geophysical Research Letters*, *7*(4), 279–282. https://doi.org/10.1029/GL007i004p00279

Shreedharan, S., Bolton, D. C., Rivière, J., & Marone, C. (2020). Preseismic fault creep and elastic wave amplitude precursors scale with lab earthquake magnitude for the continuum of tectonic failure modes. *Geophysical Research Letters*, *47*(8), 1–10. https://doi.org/10.1029/2020GL086986

Shreedharan, S., Bolton, D. C., Rivière, J., & Marone, C. (2021a). Competition between preslip and deviatoric stress modulates precursors for laboratory earthquakes. *Earth and Planetary Science Letters*, *553*, 116623. https://doi.org/10.1016/j.epsl.2020.116623

Shreedharan, S., Bolton, D. C., Rivière, J., & Marone, C. (2021b). Machine learning predicts the timing and shear stress evolution of lab earthquakes using active seismic monitoring of fault zone processes. *Journal of Geophysical Research: Solid Earth*, *126*(7), 1–18. https://doi.org/10.1029/2020JB021588

Shreedharan, S., Rivière, J., Bhattacharya, P., & Marone, C. (2019). Frictional state evolution during normal stress perturbations probed with ultrasonic waves. *Journal of Geophysical Research: Solid Earth*, *124*(6), 5469–5491. https://doi.org/10.1029/2018JB016885

Snieder, R. (2006). The theory of coda wave interferometry. *Pure and Applied Geophysics*, *163*(2-3), 455–473. https://doi.org/10.1007/s00024-005-0026-6

Snieder, R., Grêt, A., Douma, H., & Scales, J. (2002). Coda wave interferometry for estimating nonlinear behavior in seismic velocity. *Science*, *295*(5563), 2253–2255. https://doi.org/10.1126/science.1070015

Stähler, S. C., Sens-Schönfelder, C., & Niederleithinger, E. (2011). Monitoring stress changes in a concrete bridge with coda wave interferometry. *The Journal of the Acoustical Society of America*, *129*(4), 1945–1952. https://doi.org/10.1121/1.3553226

Stanchits, S., Mayr, S., Shapiro, S., & Dresen, G. (2011). Fracturing of porous rock induced by fluid injection. *Tectonophysics*, *503*(1-2), 129–145. https://doi.org/10.1016/j.tecto.2010.09.022

van Uijlen, W. M. (2013). *Rotliegend geology in the Southern Permian Basin: the development of synrift sediments and its relation to seismic imaging* [MSc. Thesis]. Utrecht University. https://studenttheses.uu.nl/handle/20.500.12932/14228

Veltmeijer, A., Naderloo, M., & Barnhoorn, A. (2023). Active and passive seismic monitoring of laboratory-based injection-driven fault reactivation. *84th EAGE Annual Conference & Exhibition*, 1–5. https://doi.org/10.3997/2214-4609.202310513

Veltmeijer, A., Naderloo, M., Pluymakers, A., & Barnhoorn, A. (2022). Acoustic monitoring of laboratory induced fault reactivation. *83rd EAGE Annual Conference & Exhibition*, (April), 1–5. https://doi.org/10.3997/2214-4609.202210269

Wang, K., Johnson, C. W., Bennett, K. C., & Johnson, P. A. (2022). Predicting future laboratory fault friction through deep learning transformer models. *Geophysical Research Letters*, *49*(19), 1–9. https://doi.org/10.1029/2022GL098233

Wang, L., Kwiatek, G., Rybacki, E., Bonnelye, A., Bohnhoff, M., & Dresen, G. (2020). Laboratory study on fluid-induced fault slip behavior: the role of fluid pressurization rate. *Geophysical Research Letters*, *47*(6), 1–12. https://doi.org/10.1029/2019GL086627

Winkler, K., & Nur, A. (1979). Pore fluids and seismic attenuation in rocks. *Geophysical Research Letters*, *6*(1), 1–4. https://doi.org/10.1029/GL006i001p00001

Xie, F., Ren, Y., Zhou, Y., Larose, E., & Baillet, L. (2018). Monitoring local changes in granite rock under biaxial test: a spatiotemporal imaging application with diffuse waves. *Journal of Geophysical Research: Solid Earth*, *123*(3), 2214–2227. https://doi.org/10.1002/2017JB014940

Ye, Z., & Ghassemi, A. (2020). Heterogeneous fracture slip and aseismic-seismic transition in a triaxial injection test. *Geophysical Research Letters*, *47*(14), 1–9. https://doi.org/10.1029/2020GL087739

Zhang, Y., Abraham, O., Grondin, F., Loukili, A., Tournat, V., Duff, A. L., Lascoup, B., & Durand, O. (2012). Study of stress-induced velocity variation in concrete under direct tensile force and monitoring of the damage level by using thermally-compensated coda wave interferometry. *Ultrasonics*, *52*(8), 1038–1045. https://doi.org/10.1016/j.ultras.2012.08.011

Zotz-Wilson, R. (2020). Coda-wave monitoring of continuously evolving material properties. https://doi.org/https://doi.org/10.4233/uuid:9c0b2f03-040b-4ec8-b669-951c5acf1f3b

Zotz-Wilson, R., Boerrigter, T., & Barnhoorn, A. (2019). Coda-wave monitoring of continuously evolving material properties and the precursory detection of yielding. *The Journal of the Acoustical Society of America*, *145*(2), 1060–1068. https://doi.org/10.1121/1.5091012

6

MONITORING STRESS VARIATIONS IN LAYERED OFFSET SAMPLES IN A TRUE TRIAXIAL SETTING

UPSCALED LABORATORY EXPERIMENTS

The induced seismicity in Groningen has prompted much research on fault reactivation over the years. Both analytical and numerical models suggest that fault reactivation in Groningen is initiated by the growth of small slip patches, which nucleate on the corners of offset faults. However, these models have yet to be verified by laboratory studies. To address this gap, a layered sample with an offset fault, designed to mimic the faults in Groningen, is used to investigate slip nucleation in a laboratory setting. This experiment tests the limits of the available laboratory equipment and demonstrates that the ultrasonic monitoring method, employing coda wave decorrelation, can be used to infer local stress variation along the offset fault induced by increased vertical stress (σ_1) and pore pressure variations.

The experiment described in this chapter has been a joint effort between Milad Naderloo and myself. The experiments resulted in two datasets, this thesis focuses on the active acoustic dataset and the thesis of M. Naderloo focuses on the mechanical dataset.

6.1. INTRODUCTION

Induced seismicity, particularly in densely populated areas, can have a significant societal impact. An example of this is the gas production in Groningen which has induced much seismicity over the years (Muntendam-Bos et al., 2022), causing damage to houses. Knowledge about fault nucleation and rupture is needed to make hazard assessments. Gas production over the years has led to pressure depletion (reduction of pressure) and compaction, studies have shown that the decrease in pressure causes stress changes within and around the reservoir (Hettema et al., 2000; Segall, 1989; Segall, 1992; Segall & Fitzgerald, 1998). These poroelastic stress changes on pre-existing faults in the reservoir can cause the fault to become unstable and slip, and possibly seismicity (Buijze et al., 2019; Segall, 1989). Analytical (Cornelissen & Jansen, 2023; Jansen et al., 2019; Jansen & Meulenbroek, 2022) and geomechanical modelling studies (Buijze et al., 2019; Buijze et al., 2017) have shown reservoir offset by faults can enhance local stresses and promote slip. These studies show that in a reservoir along an offset fault, two aseismic slip patches form at the inner corners of the reservoir, grow and merge, and become unstable resulting in nucleation of seismic slip (in Figure 6.1d the inner corners are indicated by a triangle). They show offset has a big influence on where the slip nucleates as well as whether the reservoir experiences depletion or injection. To visualize, Figure 6.1 shows an example from Buijze et al. (2019), showing simulated stresses, and slip on the fault during depletion along an offset fault, showing in Figure 6.1d, slip initiates from the inner corners of the two reservoir compartments (where SCU > 1), whereas for injection, this would be the outer corners (Jansen et al., 2019).

To our knowledge, at the time of writing, no experiments with an offset fault under subsurface conditions have been performed to verify these models. In chapter 2 the stress dependency on the ultrasonic recordings is shown as well as sensitivity to fault reactivation in chapters 3, 5. The complementary use of the active and passive monitoring methods has been shown in Chapter 4. Laboratory experiments allow systematic investigation of fault slip nucleation, by including both passive (acoustic emission) and active acoustic (ultrasonic transmission) monitoring methods both the aseismic and seismic part of fault reactivation can be detected and monitored. Upscaling to a 30 by 30 cm sample size allows for the inclusion of layers offset by a fault. It serves as an intermediate step between small-scale focused laboratory experiments and the field. Coda wave decorrelation analysis is used to investigate the effect of added complexity and scale on the presented monitoring technique in the previous chapters and to monitor local stress changes induced by stress and pore pressure cycling.

6.2. METHOD

6.2.1. SAMPLE

For these experiments, a layered sample is designed that incorporated a reservoir with an offset fault (Figure 6.2). The sample consists of layers of mortar and sandstone, where the fault offsets the sandstone reservoir by half of its thickness at a 70-degree angle to the vertical axis (Figure 6.2A). The mortar is specifically selected to serve as a homogeneous impermeable layer within the sample to maximize the contract between the sandstone reservoir and the top and bottom layer and for its desirable stiffness. The mortar has

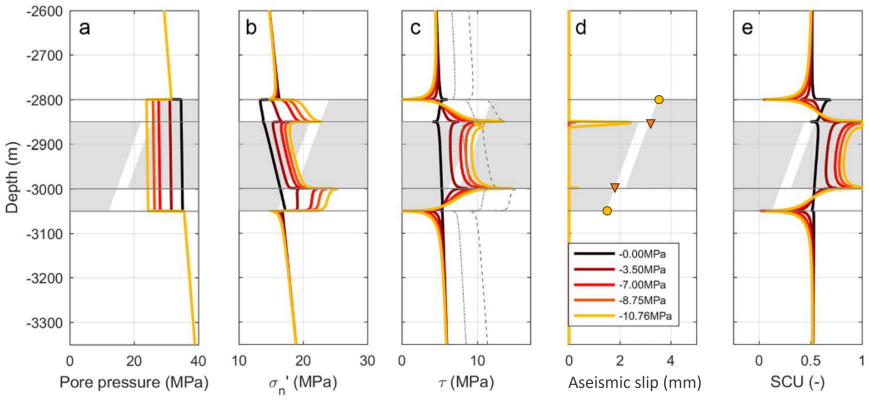

Figure 6.1: Simulated stresses, and plastic slip on the fault during depletion of two reservoir compartments with a 50-m offset taken from Buijze et al. (2019). The gray areas indicate the two reservoir compartments offset by a fault. a) Pore pressure depletion in the fault, b) effective normal stress σ'_n, c) shear stress τ, d) aseismic shear slip, triangles indicate the inner, and circles the outer corners of the offset reservoir and e) the Shear Capacity Utilization, when SCU exceeds 1, slip is promoted.

approximately 3 percent porosity and virtually zero permeability. To ensure a hermetic seal, which could hold up to 10 MPa pore pressure, the entire setup is enclosed within an aluminium resin. Furthermore, an outer mortar layer is added to securely fit the assembly into the experimental apparatus and aid the sealing resin layer in preventing pore fluid outbreak from the reservoir layer (Figure 6.2). Each cast of mortar is followed by a month in a curing room to prevent dehydration and crack formation in the mortar layers. The properties of each material used are listed in Table 6.1. After finalizing the sample assembly, the injection and depletion lines are drilled and a groove was cut out to accommodate the fluid lines (Figure 6.2C, D). The Red Felser sandstones used are from the Rotliegend formation formed during the early Permian and are from the same formation as the Groningen reservoir (Naderloo et al., 2023; van Uijlen, 2013). The sandstones used in our experiments are from a quarry in the Palatine forest near Kaiserslautern, Germany. The Red Felser sandstone is homogeneous and isotropic at the scale of a large block (several decimetres in size), with an average porosity of 19%.

Material	ϕ (%)	E (GPa)	ν (-)	μ (-)
Sandstone	19	17	0.3	0.61
AL resin	0	5.2	0.34	-
Mortar	3	19.8	0.115	0.67
Sandstone-mortar	-	-	-	0.62

Table 6.1: Material properties of the different layers in the sample, showing the porosity ϕ, Youngs modulus E, poisons ratio ν, and friction coefficient μ

6.2.2. LOADING AND ACQUISITION SYSTEM

The experiments have been performed in an in-house built true triaxial loading frame (Figure 6.3). Each of the three directions consists of a side with a hydraulically driven piston with a load cell integrated and a so-called door preventing any movement. The pistons are load-controlled with a maximum capacity of 3500kN. Pore fluid pressure was maintained using two ISCO pumps, model 500D, and the differential pressure was measured using an Endress + Hauser Deltabar, 0-4 bar range. Displacement is measured using 6 in-house built linear variable displacement transducers (LVDT) with a range of 15 mm, each of the directions is measured using 2 LVDTs mounted at opposite corners of the loading plates. These plates are in contact with the sample and are lined with Teflon sheets. Holes into the plates leave space for ultrasonic transducers and their cables. A spring system is included behind the transducers to protect the transducers from

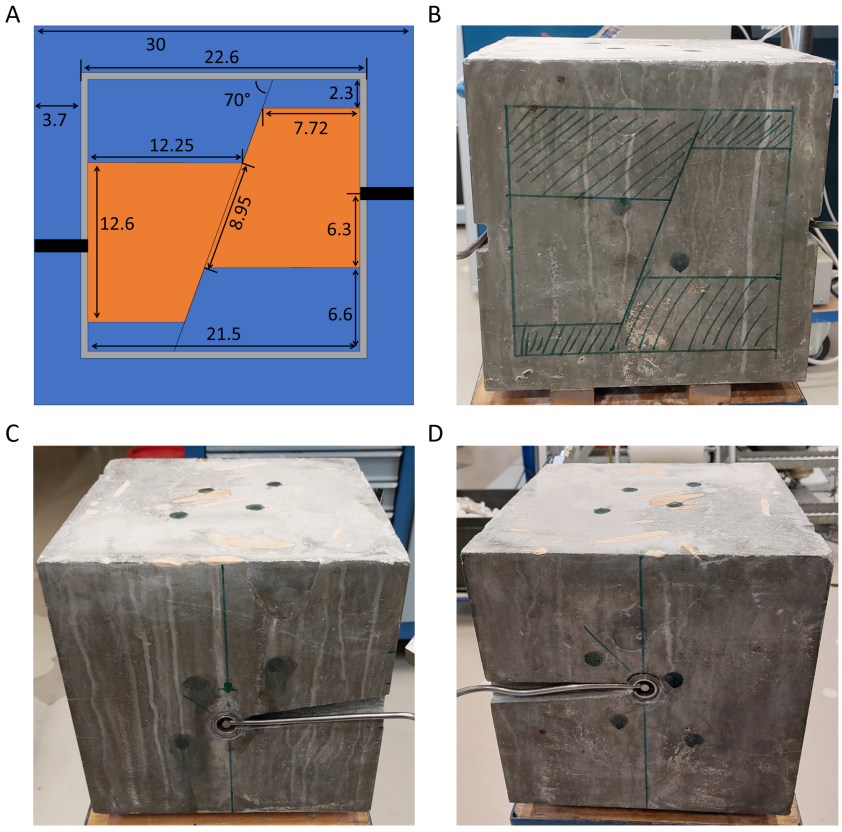

Figure 6.2: Sample design. In A the geometry and B to D pictures of the finished sample just before the test. In B a front view of the sample including a rough sketch of the orientation of the fault and layers (Not to scale and not on the exact position of the layers inside). In C and D the sides of the sample showing the pore fluid lines into the reservoir. The estimated location of the transducers is spray-painted on the sample in B to D.

the applied loads and ensure constant continuous coupling to the sample (Figure 6.4). To improve the wave propagation and coupling between transducers and the sample, a thin layer of Echo Ultrasonics, LLC wave coupling agent was applied. In total 20 Olympus 1MHz/.5" ultrasonic piezoelectric transducers were used, of which 8 v153 (S-wave) and 12 v103 (P-wave) transducers, which are arranged over the six sides of the sample (Figure 6.5).

A Richter acoustic emission system is used to acquire the passive and active acoustic data. The Richter system is a 20-channel, 16-bit acquisition system. For the acoustic emission (AE) it provides simultaneous and synchronous sampling of all 20 input channels. The AE channels were pre-amplified by 40 DB amplifiers. Using the ExStream software, the (pre-amplified) continuous waveforms are recorded at a sampling rate of 2 MHz, and input impedance of 50 Ω for 1 min, after every min the software initiates an active survey. The pulser amplifier system sends out a pulse with 45 V iterative through the transducers, such that each of them acts as a source once while the other records for 1.0 ms, this active survey takes about 6 seconds, after which the ExStream will measure continuous again for 1 min. This sequence of 1 min passive recording and 6 seconds active survey was continued throughout the entire experiment. Afterwards, the continuous waveform data was managed by the Insite Seismic Processing software and data was converted to single waveforms, or events, using a predefined trigger logic. An event was recorded if 2 or more transducers per plate exceeded a voltage threshold of about 150mV, within a window length of 480 sample points.

6.2.3. EXPERIMENTAL PROTOCOL

Two experiments were conducted on the same sample, with a slightly different protocol (Figure 6.7). Both protocols include stress cycling and pore pressure cycles to reactivate the faulted reservoir several times. The protocol was designed to verify the numerical and analytical models of Buijze et al. (2019) and Jansen et al. (2019) to identify the slip initiation on the corners of the faulted reservoir, leading to slip along the fault. The first protocol is based on a numerical model using the open-source multiphysics numerical simulator GEOS, see Figure 6.6. The initiation of slip and growth of the slip patches is analysed using Coulomb stress σ_c , which is defined as the difference between the shear stress σ_{shear} along the fault plane and its shear strength $\sigma_{strength}$ as $\sigma_c = \sigma_{shear} - \sigma_{strength}$. When the $\sigma_c > 0$, the stresses along the fault exceed it strength and slip is initiated. According to these results, slip patches should start to form under $\sigma_{1,2,3}$ = 10 MPa and P_p = 5 MPa stress conditions at the top and bottom corners of the reservoir. No micro-seismicity, or acoustic emission was recorded during this experiment when 10 MPa and 5 MPa pore pressure was reached, therefore the loading protocol was adjusted and higher pressures are imposed, but repeating the last two cycles of the first protocol (Figure 6.7). Throughout the experiment, σ_2 and σ_3 are kept equal and constant at 10 MPa. During stress cycling the pore pressure was kept constant at 5 MPa, and when the reservoir was depleted to 3 MPa the stress σ_1 was kept constant.

Both loading protocols start with hydrostatically ($\sigma_1 = \sigma_2 = \sigma_3$) loading the sample to 7 MPa, and the pore pressure increased to 3 MPa. Then the hydrostatic loading continued to 10 MPa after which the pore pressure was increased to 5 MPa. Then the cyclic loading and unloading starts.

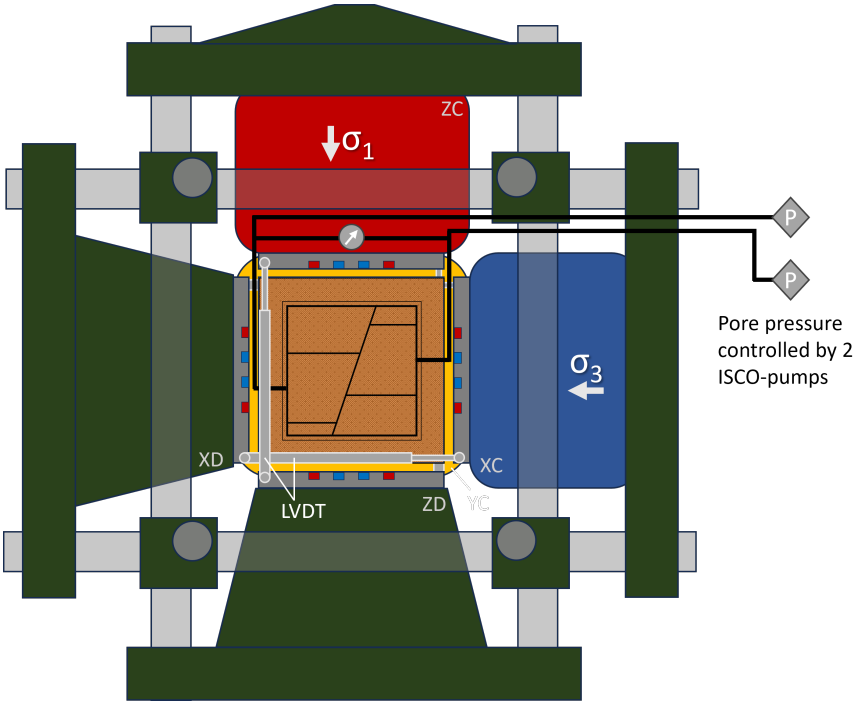

Figure 6.3: Schematic of true triaxial loading frame (not to scale). Each loading direction has 2 LVDT on opposite corners, (i.e. Z-direction or σ_1, 1 LVDT is shown vertically in this scheme on the left of the block, the other is situated on the back of the sample on the right side). The viewing direction is the Y-direction, or σ_2, with the pump at the back of the frame. The arrows show the loading direction of σ_1 and σ_3. The cylinder side of each loading direction are labeled XC, YC, ZC these push against the fixed side, which are labelled XD, YD, ZD. Each plate contains P- and/or S-wave transducers for acoustic monitoring visible in Figure 6.5. Pictures of laboratory setup in Appendix A, Figures A.10 to A.12.

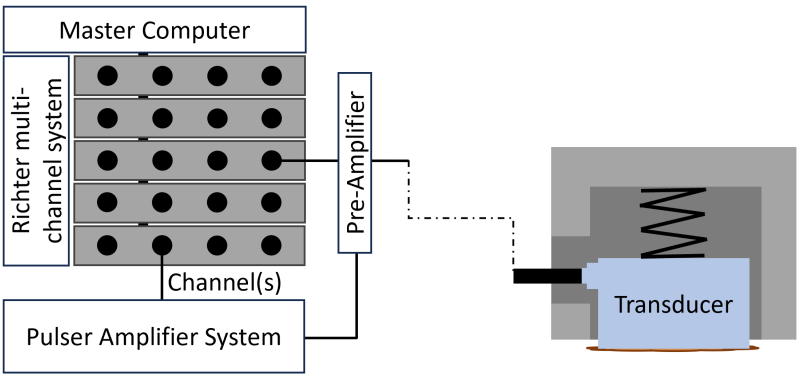

Figure 6.4: Schematic of acoustic monitoring system (not to scale). On the left the Richter system preamplifying the outgoing and incoming signals. On the right the transducer in the loading frame, which is protected from additional load by a spring and good coupling was ensured using a coupling agent. Picture of laboratory setup in Appendix A, Figure A.13.

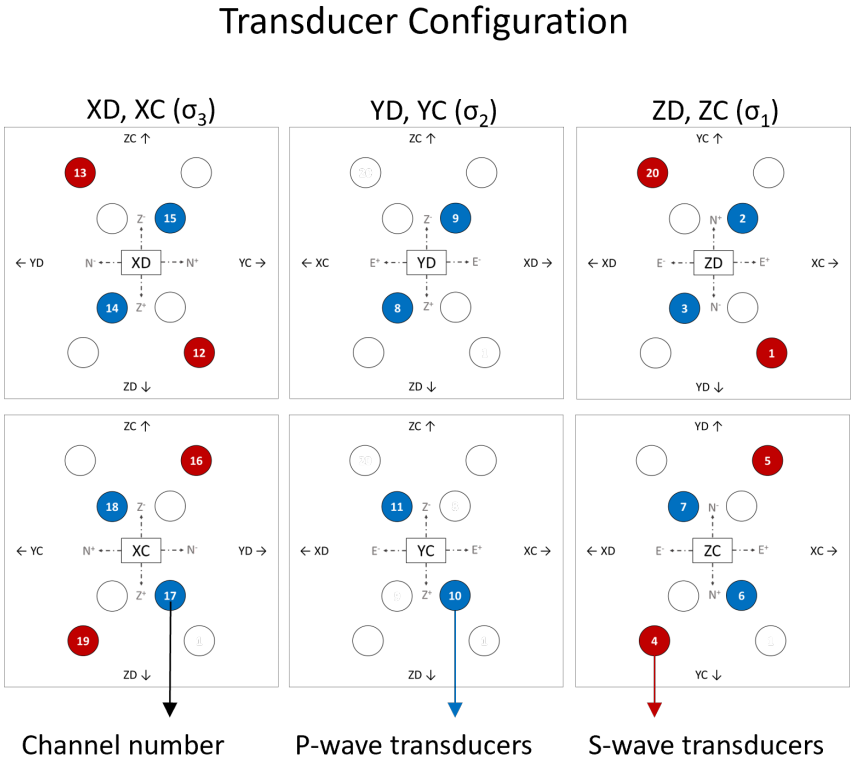

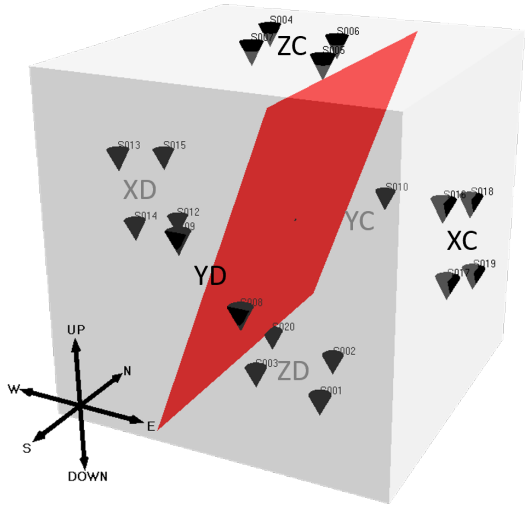

Figure 6.5: Transducer configuration per side of the true triaxial loading frame, with in red the S-wave transducers and in blue the P-wave transducers, each direction (X, Y, or Z) is a mirror image. The cylinder sides of each loading direction are labeled XC, YC, ZC these push against the fixed sides, which are labelled XD, YD, ZD. Picture of laboratory setup in Appendix A, Figure A.13.

In the first protocol (Figure 6.7) three cycles to 10 MPa with a rate of 1 kN/s, are performed, with after each stress cycle a depletion cycle, decreasing the pore pressure to 3 MPa with a rate of 5 bar/min. After three cycles an extra increase in σ_1 was added to increase the differential pressure on the fault and increase the possibility of slip patches formation. The pressure of this last cycle is significantly higher than what the modelled pressure needed to induce local slip patches. The σ_1 was increased to 17 MPa, upon reaching this the pore pressure was released by opening the outlet valve creating a 5 MPa to 1 bar difference between in and outlet, after unloading the sample and stopping the acoustic data acquisition.

The second protocol (Figure 6.7), repeats the last two stress and pore pressure cycles of the first protocol, afterwards, the stress is cyclically increased by steps of 5 MPa. The cycles in pore pressure are performed at the peak stresses of each stress cycle, but the same in magnitude, the pore pressure is decreased to 3 MPa and increased to 5 MPa, with a rate of 5 bar/min. Similarly, to the first protocol, the outlet valve was opened of the pore pressure at the last stress cycle, after the pore pressure was increased to 8 MPa. This was repeated 4 times, after which the sample was unloaded and the acoustic data acquisition stopped.

During the first experiment, signals were only logged for wave arrival time (s), and amplitude (volt), due to a software glitch. The first loading protocol is reconstructed by

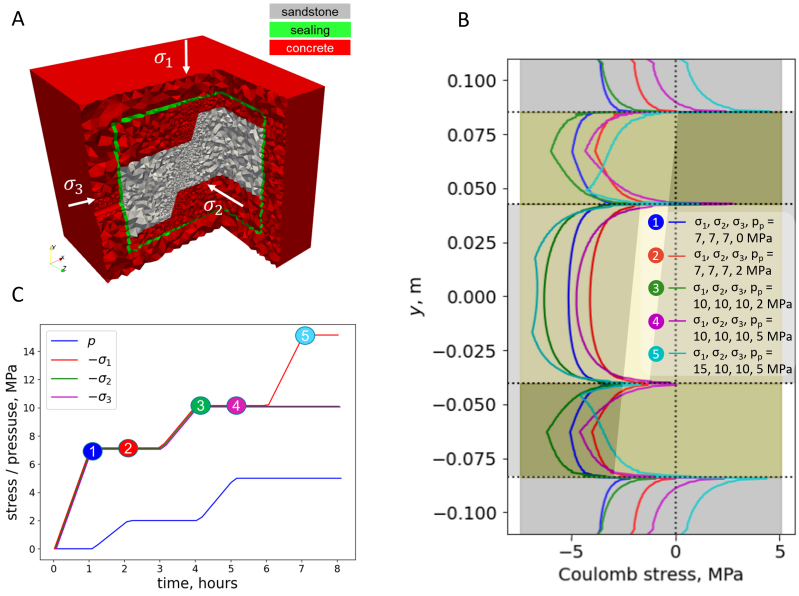

Figure 6.6: Results of numerical modelling, (courtesy of Alek Novikov). Showing the model in A and the coulomb stresses along the the fault in B for different loading steps. The corresponding loading of σ_1, σ_2 and σ_3, and the pore pressure P_P is shown in C. When the Coulomb stresses exceed 0, the fault slip is locally promoted and slip patches are able to nucleate. In the last last two loading steps, Coulomb stress is larger than 0, starting at the outer corners of the fault, growing outwards.

extensive notes, but the displacement measurements aren't available. During the second experiment, signals were logged for three directions of force (N), confining pressure (bar), all directions of displacement (μm), pore fluid pressure (bar), and wave parameters arrival time (s), and amplitude (volt).

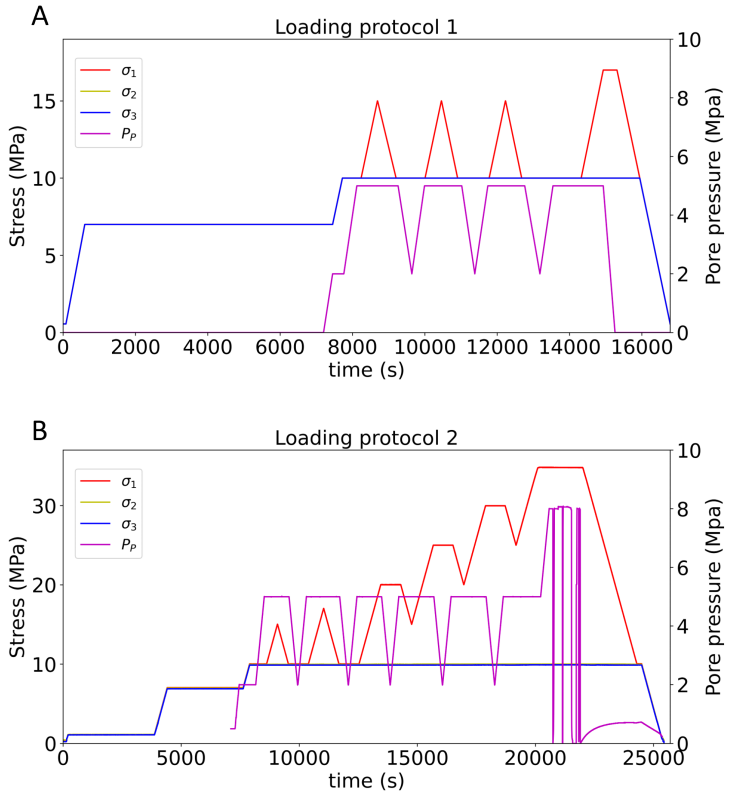

Figure 6.7: Loading protocols. In A protocol 1 and in B protocol 2, showing the three principal stresses σ_1, σ_2 and σ_3, and the pore pressure P_P.

6.3. DISCUSSION OF RESULTS

No acoustic emission was recorded during the first experiment, with the loading protocol based on modelling results (Figure 6.6 and 6.7A). Therefore, either no micro- seismicity was generated or the generated energy was too low or too attenuated to be recorded and detected above the noise levels. Additionally to passive acoustic emission recording, every minute active transmission measurements were performed. One recorded wavelet of the three transmission pairs, with the highest signal-to-noise ratio (SNR), in each loading direction, is visualized in Figure 6.8. To detect stress changes from the recorded waveforms using coda wave decorrelation, a sufficient SNR is needed, oth-

erwise, the stress changes might fall below the resolution of the data, as noted by Niu et al. (2008), who using a similar approach using monitoring doublet near the San Andreas fault, didn't detect an M2.6 event, but with better SNR data did detect a smaller M1 event. All the recordings on the X-plates show very high noise levels. The presence of the fluid lines on these sides of the sample (Figure 6.2) causes reverberations and vibrations during fluid depletion or injection, increasing the noise levels and overpowering the waveforms in the σ_3 direction (Figure 6.8C). Therefore, time-lapse analysis to analyse the stress changes within the reservoir is only performed for the recorded waveforms of the transmission pairs in σ_1 and σ_2 directions.

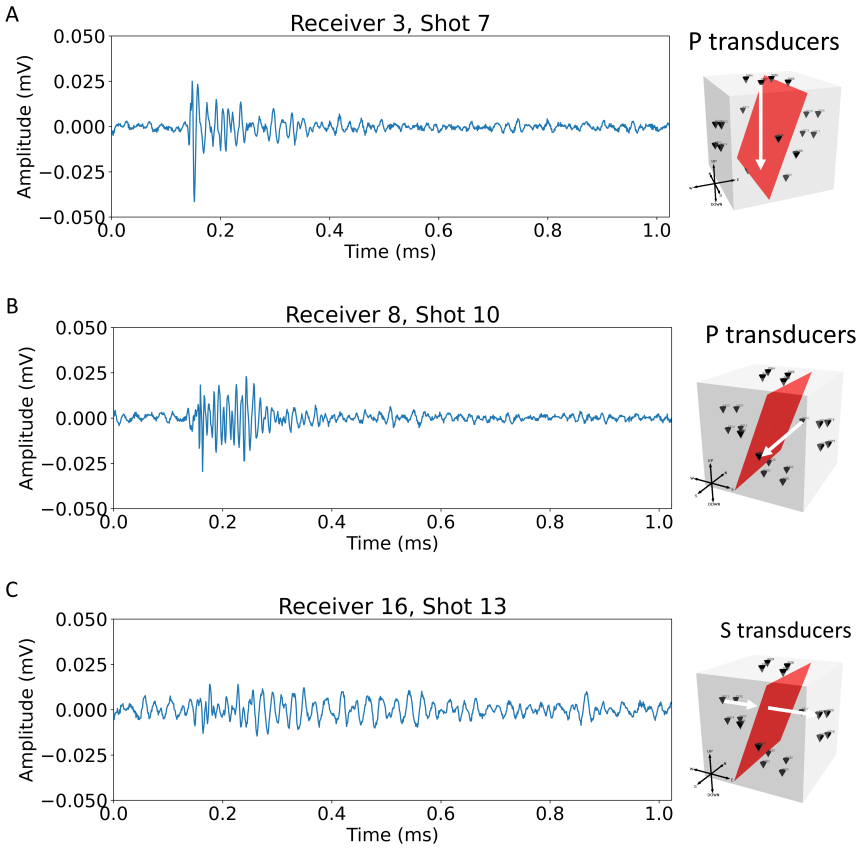

Figure 6.8: Recorded wavelets of survey 57 (at time 9938 sec), a transmission pair of each loading direction. A. recorded wavelet from a P-wave transducer pair for σ_1 direction. B. recorded wavelet from a P-wave transducer pair for σ_2 direction. C. recorded wavelet from a S-wave transducer pair for σ_3 direction.

To assess the changing stresses within the sample coda wave decorrelation is used (Eq. 1.6). The evolution of the decorrelation coefficient K (Eq. 1.8) throughout the stress and pore pressure cycles is visualized in Figure 6.9 (this data including the standard de-

viation and the evolution of the transmitted amplitudes can be found in Appendix A, Figures A.9 and A.7). For the transmission pair receiver 3 and shot 7 (Figure 6.9A), which measures in the σ_1 direction, the K follows the σ_1 stress cycles by increasing with decreasing stress and decreasing with increasing stress, similarly it follows the pore fluid depletion and injection cycles. K shows sensitivity to the stress direction and monitoring direction as σ_2 has been constant throughout the experiment, and in this monitoring direction (Figure 6.9B), K remains constant during the σ_1 cycles but decreases with depletion. Additionally, some hysteresis effects (i.e. the dependence of the state of a system on its history) can be observed in this data (Figure 6.9). In the first depletion cycle, K decreases simultaneously with the pore pressure, while in the next two cycles, K decreases at a later time when more depletion has already occurred. Such a hysteresis effect can be observed for the last stress cycle (Figures 6.9A). During a longer hold time with constant stresses, the sample is allowed to relax and settle, consequently, an increased amount of σ_1 is needed before K drops, indicating some hysteresis effect and the presence of permanent (inelastic) deformation has occurred within the sample.

In chapter 5 fault reactivation is indicated by a large and sharp increase in K (Figure 5.5). The absolute change in value of K in this first experiment is very small (Figure 6.9), hence no significant perturbations within the sample have been detected by the ul-

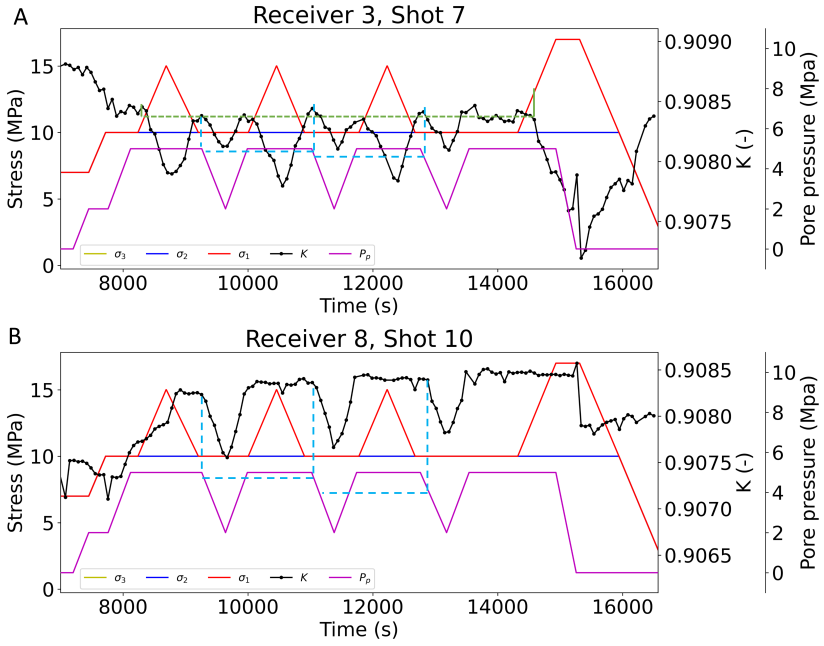

Figure 6.9: The evolution of decorrelation coefficient K for a (P-wave) transmission pair during the first experiment. A. in Z- or σ_1 direction and B. in Y- or σ_2. The blue line in A and B indicates the hysteresis effect observed by K, due to depletion. The green line in A shows the hysteresis effect in the last stress cycle after a longer holding time.

trasonic transmission measurements. This can be explained in various ways, either the monitoring isn't sensitive enough to pick up any stress variation induced along the fault. By upscaling the sample and adding layers, a large complex geometry has been created. The sent and recorded waves will likely not sample the entire sample anymore, hence local stress perturbation could more easily be missed. Another explanation would be the limited measurement points. In the previous chapter it can be seen that the stages of fault reactivation occur in seconds, in which K peaks before and during fault reactivation and returns to a stable level afterwards, by measuring every minute, these rapid changes before and during local fault reactivation can be easily missed. It can be concluded that no significant stress changes have occurred along the fault plane. The numerical model is based on laboratory-derived properties, but the modeled slip patches are small and might not have been created under the current imposed stress levels. While K clearly shows sensitivity to the imposed stress changes, the evolution of K shows no clear signs of fault reactivation. Additionally, no acoustic emission was recorded, hence, it is unlikely that the fault within the sample has moved or had local slip patches formed under the imposed stress conditions of the first loading protocol.

During the second loading protocol, the vertical stress (σ_1) was increased until the limits of the machine to maximize the slip potential. Additionally, the software glitch was resolved which resulted in the recording of displacement by the LVDTs (Figure 6.10). This data does not show clear jumps or other signs of fault reactivation, but it is important to note that this displacement is over the entire sample, hence it includes the displacement of the sealing and mortar encasing. The total permanent deformation recorded by the LVDTs is 0.6 mm (Figure A.8). Similar to the first experiment the transmission pairs showing the highest signal-to-noise ratio in each stress direction (σ_1, σ_2, and σ_3) are chosen for time series analysis (Figure 6.11). Compared to the first experiment, the recorded waveforms show higher recorded amplitudes due to higher imposed stresses, and a single transmission pair in the X-direction exhibits a reasonable signal-to-noise ratio, hence this pair is included in the coda wave decorrelation analysis.

Three acoustic emission (AE) events were detected during this second experiment. These AE events, were recorded by transducers on single plates (Figure 6.12), within a time span of 6 minutes during the last increase in σ_1. Unfortunately the nucleation point of the AE event could not be located due to an insufficient number of recordings. Most of the events are recorded on the left side of the fault, suggesting most of the generated seismic energy was propagated towards the left side. The fault plane seems to have acted as an attenuating barrier for the waves traveling through. Additionally, the AE events weren't recorded by the transducers in the Z-plates. In this σ_1-direction, generated AE has to propagate through multiple layers (concrete and reservoir) (Figure 6.2A), introducing reflecting layers, and attenuating the AE energy, potentially resulting in insufficient AE energy to exceed the recorded noise levels. The timing of these events is included in Figures 6.13 to 6.15, which show the evolution of K and the maximum transmitted amplitude T of the recorded waves of a transmission pair in each loading direction.

Similar to the first experiment, the coda wave decorrelation coefficient K cycles throughout the experiment following the stress and pore pressure changes in the σ_1-direction (Figure 6.13). Compaction due to increased σ_1 leads to a decreasing trend in decorre-

lation while the reverse, the opening of pore space, by creating fractures, increasing the pore pressure or release of stress increases the decorrelation coefficient. It can be seen that, while having a significant standard deviation, this trend is mostly followed throughout the experiment.

The Kaiser effect is the effect in which new AE events are generated for stresses higher than previous imposed stress levels, indicating new permanent deformation is formed only when reaching new stress levels (Holcomb, 1993; Li & Nordlund, 1993). A Kaiser-like effect can be observed in K and the transmitted amplitudes (T). These two parameters remain relatively stable during these two cycles, changing with the imposed stress change, but returning to their original levels. After these two cycles, an overall decreasing trend can be observed in K, and increasing in T. The first two cycles are a repeat of the first loading protocol, hence, the sample was already exposed to these stresses. This suggests any new permanent deformation is induced in the later cycles.

A similar directional dependence of imposed stress direction and monitoring dependence is visible in K in the σ_2 monitoring direction (Figure 6.14A), but less so for K in the σ_3 monitoring direction (Figure 6.15A). During depletion and injection, the K shows a trough and the T a peak, this effect is reversed in the σ_3 direction after the two repeat cycles. As this direction is perpendicular to the fault, this reversed effect could be explained by opening or dilation of the fault due to increased pore pressure. The opening of the fault would be towards the lowest stress direction σ_3, while σ_2 would remain the same, as this is parallel to the fault plane.

Whereas in the first experiment, the absolute changes in K are very small, in this second experiment some anomalies within the cyclic trend can be spotted. In Figures 6.13 to 6.15, yellow arrows indicate small jumps in K and T, at the same time as the recorded AE events. This suggests that something happened along the fault plane. A local slip-patch or audible creep has been induced by the high-induced stresses in the last cycle. This local stress change along the fault led to a jump in the monitoring of K and T. Track-

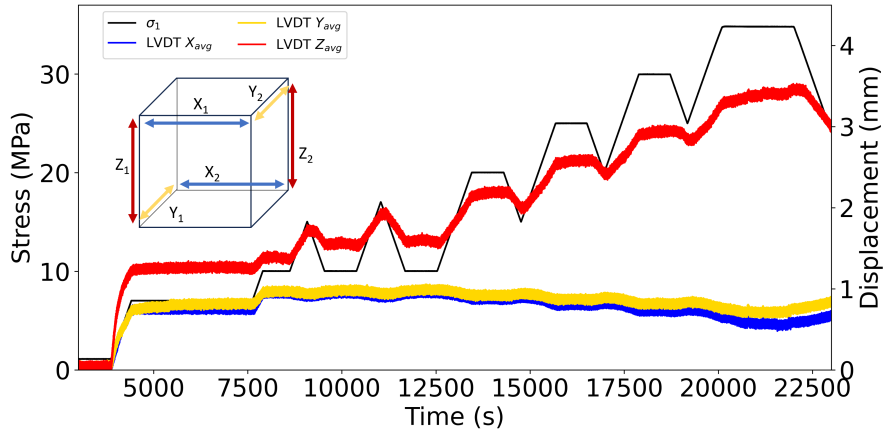

Figure 6.10: Average displacement in each of the three principal directions Z = σ_1, Y = σ_2, and X = σ_3 for the second loading protocol. The average is of two LVDTs in opposite corners of the sample.

ing back from this anomaly during the last cycle, other anomalies can be detected in the evolution of K and T (one example is indicated by a blue arrow in Figures 6.13 and 6.14), suggesting more local stress changes along the fault plane are detected by the active data. This can not be confirmed by micro-seismicity as no AE events are recorded at this time, but these could be aseismic slip patches.

In the previous chapters, the samples were relatively small, and it was assumed that the coda wave scattered through the sample and thereby samples the entire sample. By upscaling the sample and a creating more complex geometry, this assumption is no longer valid. The recorded waves are from a certain band around the direct transmission (ray) path, hence they will not have sampled the entire sample/ fault, which in the previous chapter was assumed. This implies that local perturbations in the sample will be detected by only the transmission pairs crossing this perturbed zone. Not all the transmission pairs or measurement directions show an anomaly at the same timing, such as the anomaly indicated by the blue arrow in Figure 6.13. The other two pairs, do not show

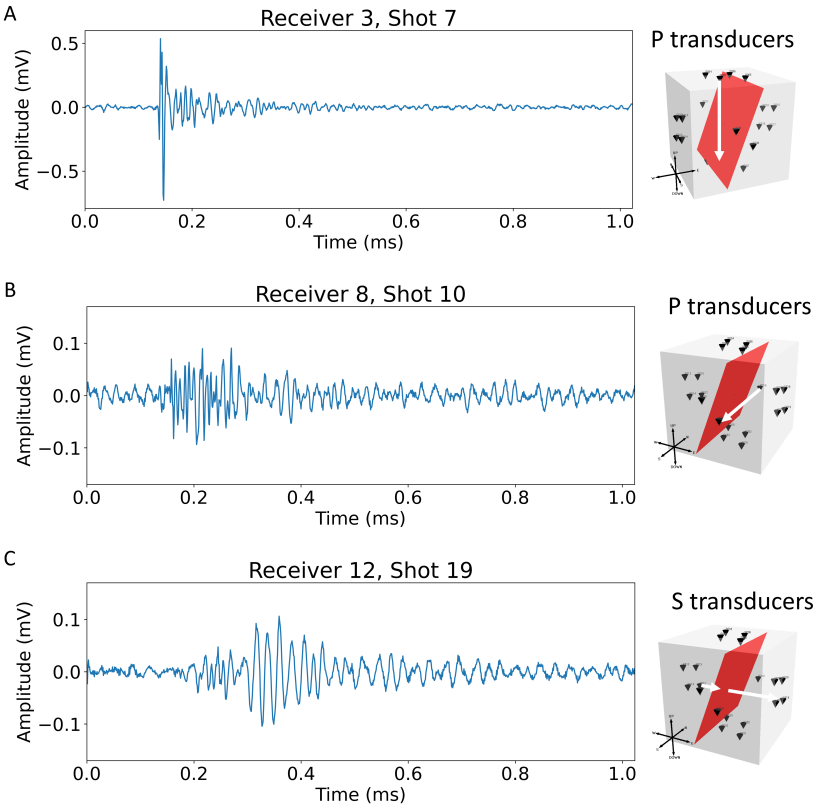

Figure 6.11: Recorded wavelets of survey 170 (at time 20287 sec, during last cycle), a transmission pair of each loading direction. A. recorded wavelets from a P-wave transducer pair for σ_1 direction. B. recorded wavelet from a P-wave transducer pair for σ_2 direction. C. recorded wavelets from a S-wave transducer pair for σ_3 direction.

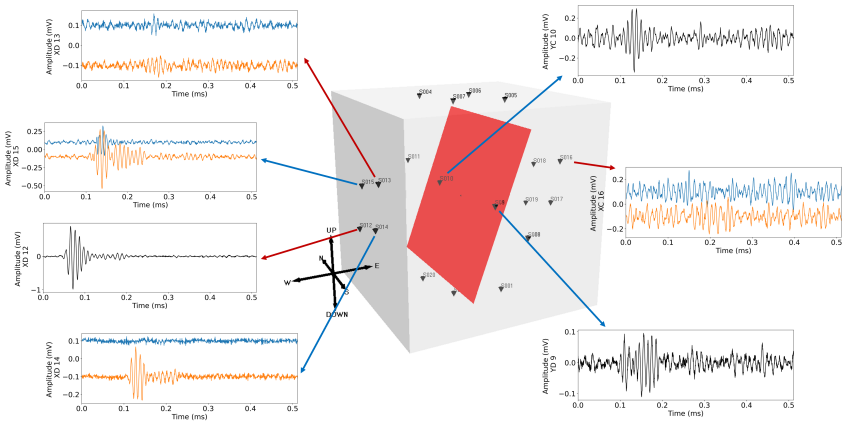

Figure 6.12: Recorded acoustic emission. Blue wavelets at 15:28:48, black at 15:34:58, and orange at 15:35:07. The other receivers didn't record any wavelet detectable above the noise level.

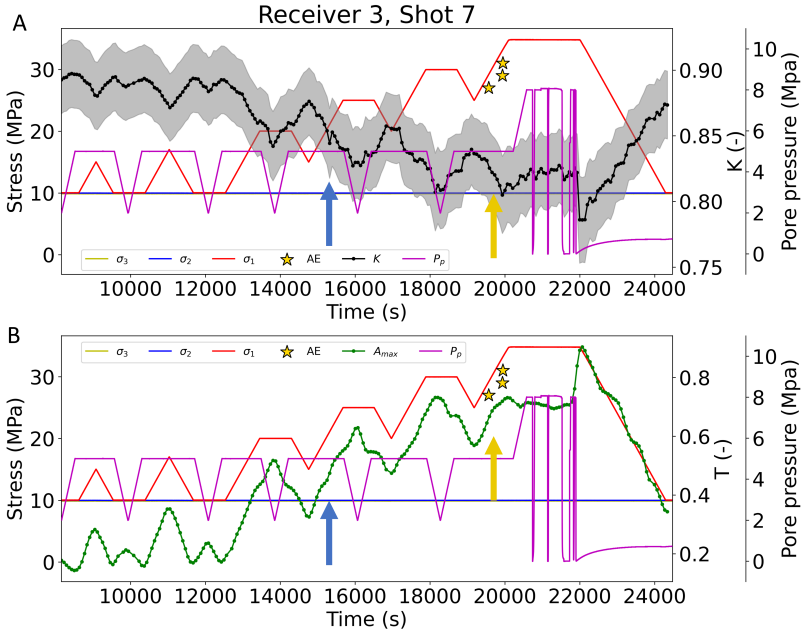

Figure 6.13: The evolution of decorrelation coefficient K, and the transmitted maximum amplitude T for the duration of the second experiment in the Z-direction (σ_1 direction). Note the amplitude of the AE events can be seen in Figure 6.12. Yellow arrow indicates anomaly in K or T at the time the AE events are recorded. Blue arrows shows another anomaly in K or T, however no AE was recorded at this time.

a clear anomaly in K and T at the same timing, implying this anomaly is a result of a stress perturbation along the transmission path of this pair only.

Due to the lack of AE events recorded, the localization of possible slip patches and the conclusion of slip formation around the corners of the reservoir is hard to draw. The active acoustic survey for the second experiment shows multiple signs of possible slip, but all but one cannot be verified by any AE recordings. These anomalies could very well be aseismic, hence no AE would be generated, but due to the high noise levels recorded, the K values show a rather large standard deviation, and some caution should be taken, especially since due to this noise localization of the perturbation in the coda, as in Larose et al. (2010) and Rossetto et al. (2011) was not possible.

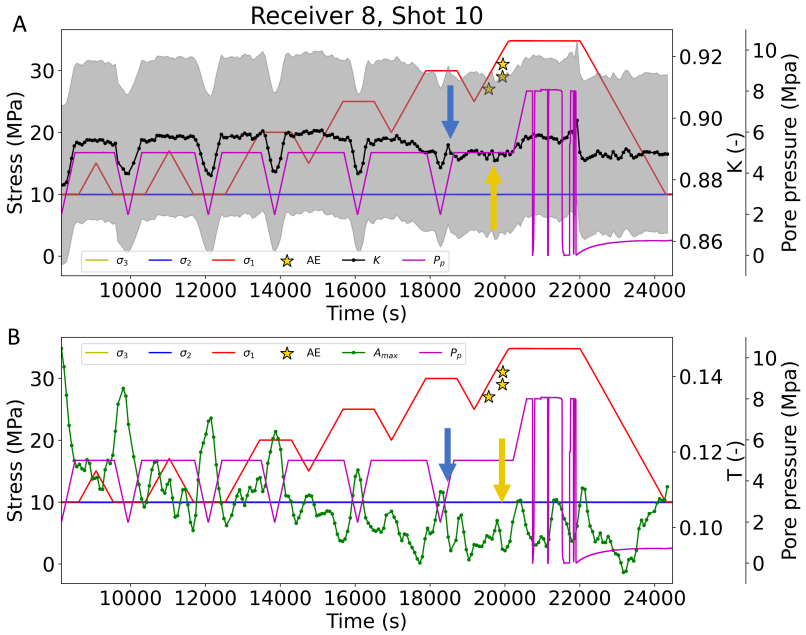

Figure 6.14: As Figure 6.13, but for an experiment in the Y-direction (σ_2 direction).

The possibility of monitoring stress changes on a larger scale, even inferring the imposed stress direction from the data, could be of added benefit in subsurface monitoring. Local stress measurement directions in the subsurface are very scarce and these could contribute to a better understanding of local stress distribution and variations in the subsurface. In addition to induced stress change in the subsurface, the monitoring method can be used to infer permanent deformation or hysteresis. In cyclic operations, such as gas or hydrogen storage, permanent deformation should be detected as these could result in less storage capacity or even leakage paths due to formed (micro-) fractures.

These experiments have been a crucial first step in upscaling. However, upscaling these findings to real reservoir scale remains a challenge. Only limited field studies,

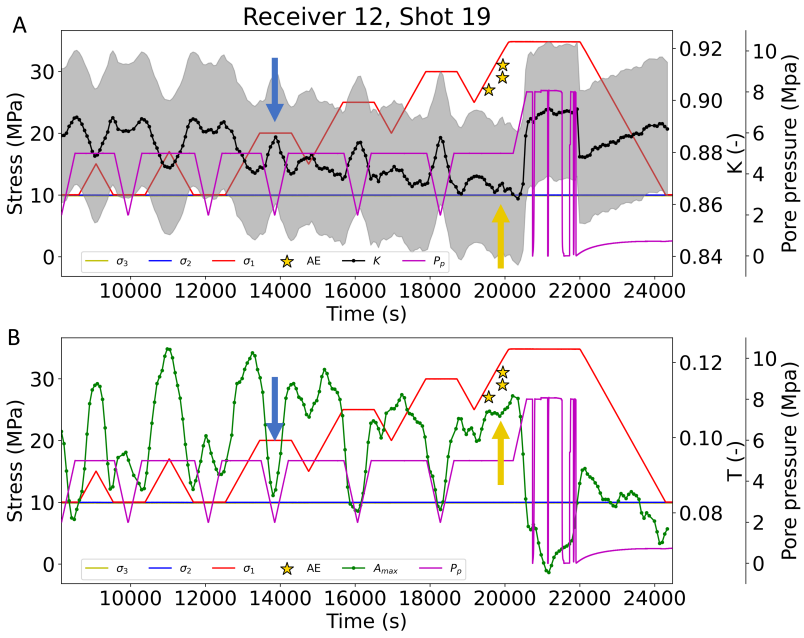

Figure 6.15: As Figure 6.13, but for an experiment in the X-direction (σ_3 direction). Blue arrow indicates the change in trend during depletion.

showing precursory signals to earthquakes, have been performed (Chiarabba et al., 2020; Niu et al., 2008). Therefore more work is needed to address the resolution and scale differences between laboratory and field. While detection of the exact damage zone, gouge formation, or micro-crack could be of lesser importance on the grand scale of forecasting earthquakes, these signals from laboratory measurements could improve the understanding of signals measured in the field. The transition from detecting stress changes to accurately forecasting the timing and extent of fault rupture remains an ongoing task. Additionally, efforts are needed to optimize the placement of monitoring stations and determine the ideal monitoring frequency. Future experimental research in these directions as well as upscaling and field applicability is encouraged.

The active data demonstrates its added value by effectively monitoring stress changes and potential aseismic slip, even though the data acquired from these experiments weren't as initially hoped for, i.e. the verification of slip patches as modeled by Buijze et al. (2019) and Jansen et al. (2019) in this laboratory setting was not possible.

6.4. CONCLUSIONS AND RECOMMENDATIONS

Large true triaxial experiments are conducted on a layered sample containing a displaced normal fault. Stress cycles and depletion cycles were conducted to induce fault instability to prove analytical and numerical models on fault reactivation. While the objectives of monitoring and possibly predicting the local induced slip patches along the fault plane were not met, the results show:

1. A large-scale experiment with depletion was successfully conducted.
2. Using active transmission measurements, stress changes, and the direction of these can be monitored as well as hysteresis induced by stress and pore pressure cycling.
3. Three acoustic emission (AE) events were recorded on a limited number of transducers.
4. At similar timing, anomalies in the decorrelation coefficient K and the transmitted amplitudes T can be observed suggesting detection of local stress changes along the fault plane and possibly a slip patch.
5. Other anomalies in K and T can be observed when no AE events are detected. Suggesting active monitoring detects (a)-seismic slip patches induced by local stress changes along the fault, highlighting the added benefit of active monitoring.

The experiments performed in this chapter had in hindsight some shortcomings and could be greatly improved. Hence a future attempt to prove the analytical and numerical models in the laboratory could benefit from the following recommendation for improvements of the experiment and sample.

1. Both the passive and active acoustic monitoring during this experiment were very much affected by the placement of the fluid lines. By designing the inlet and outlet in a different place, taking the placement and proximity of the transducers into account, or including the fluid lines into loading plates, similarly to the ultrasonic transducers and its wire, the interference with the acoustic measurements could be minimized.
2. A step back, and a simplification is also recommended. By removing the outer sealing layers, possible movement along the fault plane is not hindered by the encompassing sealing layers. One could induce fault reactivation solely by stress cycling and would be able to measure displacement using the LVDTs and small strain gouges which can be mounted along the fault plane. Removing the sealing layers also reduces the number of attenuating and reflecting layers for wave propagation, improving the odds of recording AE events, and improving the signal-to-noise ratio of the active transmission measurements.
3. By improving the signal-to-noise ratio within the recordings of the active transmission survey, localization using the perturbation of the coda wave would be possible. This set-up provides illumination all around the sample, hence, the areas of perturbations could be located, and even without AE recording an attempt of localizing the (a-seismic) slip patches could be attempted.
4. While models had shown slip patches were to be formed under certain stress regimes, the second experiment shows only limited AE was recorded under much higher imposed stresses. Measurements or investigations on how much of these stresses imposed on the outside of the sample are transferred on the fault planes are recommended. Modification to the loading protocols could be necessary, the maximum stress can not be changed due to the machine limits but loading rates or holding times could improve the experiment.

REFERENCES

Buijze, L., van den Bogert, P. A., Wassing, B. B., & Orlic, B. (2019). Nucleation and arrest of dynamic rupture induced by reservoir depletion. *Journal of Geophysical Research: Solid Earth, 124*(4), 3620–3645. https://doi.org/10.1029/2018JB016941

Buijze, L., Van Den Bogert, P. A., Wassing, B. B., Orlic, B., & Ten Veen, J. (2017). Fault reactivation mechanisms and dynamic rupture modelling of depletion-induced seismic events in a Rotliegend gas reservoir. *Geologie en Mijnbouw/Netherlands Journal of Geosciences, 96*(5), s131–s148. https://doi.org/10.1017/njg.2017.27

Chiarabba, C., De Gori, P., Segou, M., & Cattaneo, M. (2020). Seismic velocity precursors to the 2016 Mw 6.5 Norcia (Italy) earthquake. *Geology, 48*(9), 924–928. https://doi.org/10.1130/G47048.1

Cornelissen, P., & Jansen, J. D. (2023). Steady-state flow through a subsurface reservoir with a displaced fault and its poro-elastic effects on fault stresses. *Transport in Porous Media, 150*(3), 709–734. https://doi.org/10.1007/s11242-023-02029-w

Hettema, M. H., Schutjens, P. M., Verboom, B. J., & Gussinklo, H. J. (2000). Production-induced compaction of a sandstone reservoir: The strong influence of stress path. *SPE Reservoir Evaluation and Engineering, 3*(4), 342–347. https://doi.org/10.2118/65410-PA

Holcomb, D. (1993). General theory of the Kaiser effect. *International Journal of Rock Mechanics and Mining Sciences & Geomechanics Abstracts, 30*(7), 929–935. https://doi.org/10.1016/0148-9062(93)90047-H

Jansen, J. D., Singhal, P., & Vossepoel, F. C. (2019). Insights from closed-form expressions for injection- and production-induced stresses in displaced faults. *Journal of Geophysical Research: Solid Earth, 124*(7), 7193–7212. https://doi.org/10.1029/2019JB017932

Jansen, J. D., & Meulenbroek, B. (2022). Induced aseismic slip and the onset of seismicity in displaced faults. *Geologie en Mijnbouw/Netherlands Journal of Geosciences, 101*. https://doi.org/10.1017/njg.2022.9

Larose, E., Planes, T., Rossetto, V., & Margerin, L. (2010). Locating a small change in a multiple scattering environment. *Applied Physics Letters, 96*(20), 1–4. https://doi.org/10.1063/1.3431269

Li, C., & Nordlund, E. (1993). Experimental verification of the Kaiser effect in rocks. *Rock Mechanics and Rock Engineering, 26*(4), 333–351. https://doi.org/10.1007/BF01027116

Muntendam-Bos, A. G., Hoedeman, G., Polychronopoulou, K., Draganov, D., Weemstra, C., van der Zee, W., Bakker, R. R., & Roest, H. (2022). An overview of induced seismicity in the Netherlands. *Netherlands Journal of Geosciences, 101*, e1. https://doi.org/10.1017/njg.2021.14

Niu, F., Silver, P. G., Daley, T. M., Cheng, X., & Majer, E. L. (2008). Preseismic velocity changes observed from active source monitoring at the Parkfield SAFOD drill site. *Nature, 454*(7201), 204–208. https://doi.org/10.1038/nature07111

Rossetto, V., Margerin, L., Planès, T., & Larose, É. (2011). Locating a weak change using diffuse waves: Theoretical approach and inversion procedure. *Journal of Applied Physics, 109*(3). https://doi.org/10.1063/1.3544503

Segall, P. (1989). Earthquakes triggered by fluid extraction. *Geology*, *17*(10), 942–946. https://doi.org/10.1130/0091-7613(1989)017<0942:ETBFE>2.3.CO;2

Segall, P. (1992). Induced stresses due to fluid extraction from axisymmetric reservoirs. *Pure and Applied Geophysics PAGEOPH*, *139*(3-4), 535–560. https://doi.org/10.1007/BF00879950

Segall, P., & Fitzgerald, S. D. (1998). A note on induced stress changes in hydrocarbon and geothermal reservoirs. *Tectonophysics*, *289*(1-3), 117–128. https://doi.org/10.1016/S0040-1951(97)00311-9

7

CONCLUSIONS AND FUTURE OUTLOOK

This chapter summarizes the most important findings of the previous chapters in relation to the research objectives. The main aim of this thesis is to detect stress changes before failure occurs using ultrasonic transmission measurements. This chapter will also discuss future research recommendations based on the findings presented in this thesis.

7.1. CONCLUSIONS

In Chapter 2, ultrasonic transmission measurements during the failure of Red Felser sandstones are presented. By loading these sandstones until they break, the changing ultrasonic parameters can be analysed. This is done at various confining pressures, mimicking different subsurface stress conditions. The coda of the time series of recorded ultrasonic transmission wavelets is analysed using coda wave interferometry and also the attenuation throughout the experiments is analyzed by looking at the changing energy and Q-factor of the transmitted waves. These results show a clear dependence on stress changes and crack growth in the samples. Hence, these results can be used as precursors to detect upcoming failure in the samples from 40 to 70% of the failure point. Small differences are observed in the precursors between the tested confining pressures, but as the trends are very similar, a robust prediction of failure can be made by combining the various analysis techniques. In this chapter, a traffic-light forecasting system is proposed using ultrasonic transmission monitoring which is applicable for forecasting failure at various depths and or stress conditions, for a better prediction of small stress-induced changes in the subsurface and thus mitigation of failure (and seismicity) in the subsurface.

In Chapter 3, the monitoring method presented in Chapter 2 is extended to monitoring fault reactivation. Local stress variations along a fault plane can cause fault reactivation, ultrasonic transmission monitoring of both P- and S- waves is used to detect stress changes along the fault prior to reactivation and to improve the link between seis-

mic precursors and the mechanisms of fault reactivation. Sandstone samples, including a saw-cut fault, are cyclically reactivated by increasing the stresses on the sample. By using different background pore pressures, different subsurface stress conditions are tested. Analysing the evolution of P- and S-wave velocities, transmitted amplitudes, and coda wave interferometry-derived velocity changes shows consistent precursory signals for reactivation under varying stress conditions along the tested fault planes. The pre-slip phase of fault reactivation is identified and linked to the physical processes of asperity degradation and creep. Demonstrating a comparison to similar precursory signals observed in the field, this chapter highlights the feasibility of time-lapse monitoring to identify precursors to fault reactivation and establish a connection between structural processes along the fault plane and seismic signals, contributing to the improvement of future forecasting models.

In Chapter 4, active and passive acoustic monitoring are combined in cyclic stress-driven fault reactivation experiments. Acoustic emission (AE) and ultrasonic transmission measurements are compared and combined to identify the different phases of stress-driven fault reactivation, early aseismic creep (pre-slip), fault slip, and continuous sliding. The precursory signals obtained from ultrasonic transmission analysis show in the creep phase at 95% before failure, while the first AE signals are recorded at 97% before failure. The precursory signal from the active method shown earlier is slightly more sensitive to reactivation than the passive method, with the biggest advantage of being independent of seismicity-generated movement along the fault. The chapter concludes that combining both active and passive monitoring increases the accuracy of monitoring and can lead to better seismic risk mitigation.

In Chapter 5, the ultrasonic transmission method is extended to fluid injection-driven fault reactivation. Stress variations in the subsurface are often caused by variations in pore fluid pressure. By increasing pore pressure in faulted sandstones fault movement is imposed and monitored by ultrasonic transmission measurements. A comparison between smooth saw-cut faults and rough faults created by in-situ faulting of the samples is made. By analysing the temporal evolution of the coda waves and seismic amplitudes, stress changes on the fault surface can be identified, and the stages in the laboratory seismic cycle inferred as a possible basis for forecasting injection-induced fault-slip:

- inter-seismic phase: linear stress build-up
- pre-seismic phase: early creep/pre-slip
- co-seismic phase: stress drop
- continuous sliding phase: constant stresses
- post-seismic phase: fault healing

A link between seismic precursory signal and mechanisms of failure is made. The precursory signals are indicative of the destruction of fault plane asperities (gouge formation), and the opening of the fault leading to decreased asperity contact. The CWI velocity change is most sensitive to these processes during the pre-slip phase and fault reactivation, especially when the fault plane is more complex (in the case of the rough fault). However, as all the compared attributes are obtained from the same wavelet a combination of these properties shows that the stress changes along the fault can be inferred with more accuracy. As a result, the combination may be useful for monitoring faulted

or critically stressed reservoirs that experience pore pressure changes. The results of this chapter show the feasibility of active ultrasonic monitoring as a tool to identify precursors to laboratory fluid-induced earthquakes, contributing to seismic risk mitigation of both induced and natural earthquakes.

In Chapter 6, two large-scale experiments are performed as a first step in up-scaling the monitoring method of the previous chapters and to verify analytical and numerical models. These models suggest that fault reactivation in Groningen is initiated by the growth of small slip patches, which nucleate on the corners of offset faults. A layered sample with a displaced normal fault, designed to mimic the faults in Groningen, is used to investigate slip nucleation in a laboratory setting. Both stress and depletion cycles are conducted to induce fault instability and reactivation while monitoring both actively (ultrasonic transmission measurements) and passively (acoustic emission monitoring). The changing stresses, and the direction of these, within the sample are observed in the temporal evolution of the decorrelation coefficient K and the transmitted amplitudes T as well as hysteresis induced by stress and pore pressure cycling. Only three acoustic emission (AE) events were recorded on a limited number of transducers in the second experiment. At similar timing small anomalies in the evolution of K and T are observed, hinting at the detection of local stress changes along the fault plane. While no other AE events are detected in the experiments, the active transmission measurements indicate possible aseismic stress changes along the fault plane, highlighting the added benefit of active monitoring.

In conclusion, this thesis demonstrates the monitoring potential of ultrasonic transmission measurements. The method proves to be robust, effectively detecting different stages leading to sample failure under various subsurface stress conditions. The sensitivity of coda waves is highlighted throughout this thesis, revealing that by using coda wave interferometry precursory signals can be obtained that might otherwise be overlooked when solely focusing on direct arrivals. Moreover, this thesis emphasizes the significance of attenuation as a strong indicator of stress variations. The combination of these precursors enhances the robustness and overall effectiveness of the monitoring method. Identifying stress changes in the samples from the precursors and linking them with physical processes within the sample improves the understanding of the relation between precursors and mechanisms of failure. Thus in this thesis the following has been shown:

- The signals are very sensitive to induced stress changes. These precursors can form the basis for a traffic-light warning system to failure.
- The precursory signals to stress-driven fault reactivation are very consistent under varying stress conditions along tested fault planes and can be linked to physical processes, such as asperity contact and degradation during the pre-slip phase.
- When fluid pressure variations are involved, the temporal evolution provides more insight into stress changes along the fault surface than absolute change in value for both rough and smooth fault surfaces.
- Combining passive and active monitoring methods enhances accuracy and aids

in better seismic risk mitigation. However, the active method exhibits precursory signals earlier and has the added benefit of monitoring possible precursors before generated seismicity or aseismic movement.

- The attempt at upscaling and validating various analytical and numerical models, while not entirely achieving the set objectives, sheds light on the complexity of upscaling, especially in the context of complex geometry. Nevertheless, the monitoring of stress changes, and potentially local changes, showcases the method's considerable potential, even in challenging scenarios.

7.2. FUTURE OUTLOOK

This research was prompted by the increasing number of induced earthquakes in the Groningen area (the Netherlands). If technically feasible, the implementation of early warning systems for seismicity could have significantly improved public perception and societal acceptance of subsurface activities. Detecting stress changes before seismicity generation allows for the timely implementation of mitigation measures. The present inability to provide early warnings to failure underscores the urgent need for advancements in monitoring and forecasting techniques. The ability to warn in advance, and/or implement appropriate mitigation is crucial, not only for the Groningen region but also for subsurface operations globally. This becomes particularly relevant as the subsurface plays a pivotal role in the ongoing energy transition (IPCC, 2023), encompassing geothermal energy, CO2 storage, hydrogen production, and radioactive waste disposal. Proactive monitoring can ensure the safe and responsible use of subsurface resources, especially when these activities (e.g. geothermal energy) are situated in proximity of densely populated areas. Experiences, such as in Basel, Switzerland M3.4 (2006) (Terakawa et al., 2012), Pohang, South Korea M5.4 (2017) (Kim et al., 2018), or even Californië, the Netherlands M1.7 (2018) (Muntendam-Bos et al., 2022), where induced seismicity recorded by passive monitoring has led to operational halts, shows the need of a proactive monitoring approach. Active monitoring would not only aid in (perceived) safety but could also ensure the uninterrupted operation of geothermal facilities or underground CO2 storage, essential aspects of the transition from fossil fuels to renewable energy.

This research provides valuable insights into the relationship between precursory signal and reactivation mechanisms and holds promise for monitoring seismicity. Future investigations are needed and should especially explore the broader applicability of the monitoring method across different geological settings. Additionally, advancements in upscaling the methodology for large-scale applications and refining prediction models can further contribute to the field. Research in this direction will ensure the continuous improvement of monitoring techniques and their adaptability to diverse subsurface scenarios.

On the upscaling part to field scale, Chiarabba et al., 2020 have shown velocity precursors to an M6.5 earthquake in Italy, using tomography using a classic seismic processing technique to obtain velocity differences between the measurement times. Niu et al., 2008 obtained pre-seismic velocity changes from the coda along the San Andreas fault. Both Chiarabba et al., 2020 and Niu et al., 2008 show the potential of active moni-

toring on the field scale. This thesis highlights the precursory signals from both the coda waves and amplitude changes to fault reactivation observed in a laboratory setting. Future research should delve into incorporating these additional parameters for a more comprehensive upscaling approach. Resolution and scale differences between the laboratory and the field should also be studied. Whereas in the lab very small stress changes and structural changes, like gouge formation can be detected by active monitoring, on field scale it is not expected to. The extent of stress differences on a fault measured, and whether the resolution of the active monitoring is sufficient for forecasting, is an important factor to be studied. Additionally, attention should be paid to the practical application of upscaling. This thesis focuses on transmission measurements, which is similar to the research of Niu et al., 2008. But in the foreseeable future, it is not feasible to drill monitoring wells everywhere, hence research into the ideal monitoring set-up is also recommended, especially into the possibility of using existing wells in reservoir and geothermal applications. On a slightly smaller scale, active monitoring of failure could be applied to monitoring the structural integrity of critical infrastructures like bridges. An example of this is Epple et al., 2022, in which they measured the integrity of the Gänstorbrücke bridge in Ulm, Germany for a year.

Another point of recommended research is forward forecasting. This thesis monitors and shows the precursory signals to failure in hindsight, similar to what is often still done in earthquake science (Picozzi et al., 2023). Current earthquake predictions are often probabilities describing the chance of an earthquake occurring in a certain region over a certain time span. By using the increasingly improving computational capabilities, improvements in forecasting can be made. Efforts, using machine learning models, have been made to improve predictions of lab quakes (Laurenti et al., 2022; Rouet-Leduc et al., 2017; Wang et al., 2022). Shreedharan et al., 2021 also included precursors from active transmission monitoring in their models and showed improved forecasting. By including inferred stress variation from active monitoring precursors in machine learning models, forecasts of the labquakes get better and better. However, the step to more complicated setups and actual forward forecasting in real-time and field scale still needs to be taken.

REFERENCES

Chiarabba, C., De Gori, P., Segou, M., & Cattaneo, M. (2020). Seismic velocity precursors to the 2016 Mw 6.5 Norcia (Italy) earthquake. *Geology*, *48*(9), 924–928. https://doi.org/10.1130/G47048.1

Epple, N., Niederleithinger, E., & Fontoura Barroso, D. (2022). Coda wave interferometry for monitoring bridges with embedded ultrasonic transducers – Lessons learned at the Gänstorbrücke bridge Ulm, Germany. *e-Journal of Nondestructive Testing*, *27*(9), 1–8. https://doi.org/10.58286/27221

IPCC. (2023). Climate change 2022: Mitigation of climate change. the working group iii report provides an updated global assessment of climate change mitigation progress and pledges, and examines the sources of global emissions. https://www.ipcc.ch/report/sixth-assessment-report-working-group-3/

Kim, K.-H., Ree, J.-H., Kim, Y., Kim, S., Kang, S. Y., & Seo, W. (2018). Assessing whether the 2017 M w 5.4 Pohang earthquake in South Korea was an induced event. *Science*, *360*(6392), 1007–1009. https://doi.org/10.1126/science.aat6081

Laurenti, L., Tinti, E., Galasso, F., Franco, L., & Marone, C. (2022). Deep learning for laboratory earthquake prediction and autoregressive forecasting of fault zone stress. *Earth and Planetary Science Letters*, *598*, 117825. https://doi.org/10.1016/j.epsl.2022.117825

Muntendam-Bos, A. G., Hoedeman, G., Polychronopoulou, K., Draganov, D., Weemstra, C., van der Zee, W., Bakker, R. R., & Roest, H. (2022). An overview of induced seismicity in the Netherlands. *Netherlands Journal of Geosciences*, *101*, e1. https://doi.org/10.1017/njg.2021.14

Niu, F., Silver, P. G., Daley, T. M., Cheng, X., & Majer, E. L. (2008). Preseismic velocity changes observed from active source monitoring at the Parkfield SAFOD drill site. *Nature*, *454*(7201), 204–208. https://doi.org/10.1038/nature07111

Picozzi, M., Iaccarino, A. G., & Spallarossa, D. (2023). The preparatory process of the 2023 Mw 7.8 Türkiye earthquake. *Scientific Reports*, *13*(1), 1–10. https://doi.org/10.1038/s41598-023-45073-8

Rouet-Leduc, B., Hulbert, C., Lubbers, N., Barros, K., Humphreys, C. J., & Johnson, P. A. (2017). Machine learning predicts laboratory earthquakes. *Geophysical Research Letters*, *44*(18), 9276–9282. https://doi.org/10.1002/2017GL074677

Shreedharan, S., Bolton, D. C., Rivière, J., & Marone, C. (2021). Machine learning predicts the timing and shear stress evolution of lab earthquakes using active seismic monitoring of fault zone processes. *Journal of Geophysical Research: Solid Earth*, *126*(7), 1–18. https://doi.org/10.1029/2020JB021588

Terakawa, T., Miller, S. A., & Deichmann, N. (2012). High fluid pressure and triggered earthquakes in the enhanced geothermal system in Basel, Switzerland. *Journal of Geophysical Research: Solid Earth*, *117*(7), 1–15. https://doi.org/10.1029/2011JB008980

Wang, K., Johnson, C. W., Bennett, K. C., & Johnson, P. A. (2022). Predicting future laboratory fault friction through deep learning transformer models. *Geophysical Research Letters*, *49*(19), 1–9. https://doi.org/10.1029/2022GL098233

A

ADDITIONAL DATA LARGE SCALE EXPERIMENTS

In this appendix, additional figures and pictures featuring the laboratory set up are shown for chapter 6: Monitoring stress variations in layered offset samples in true triaxial setting.

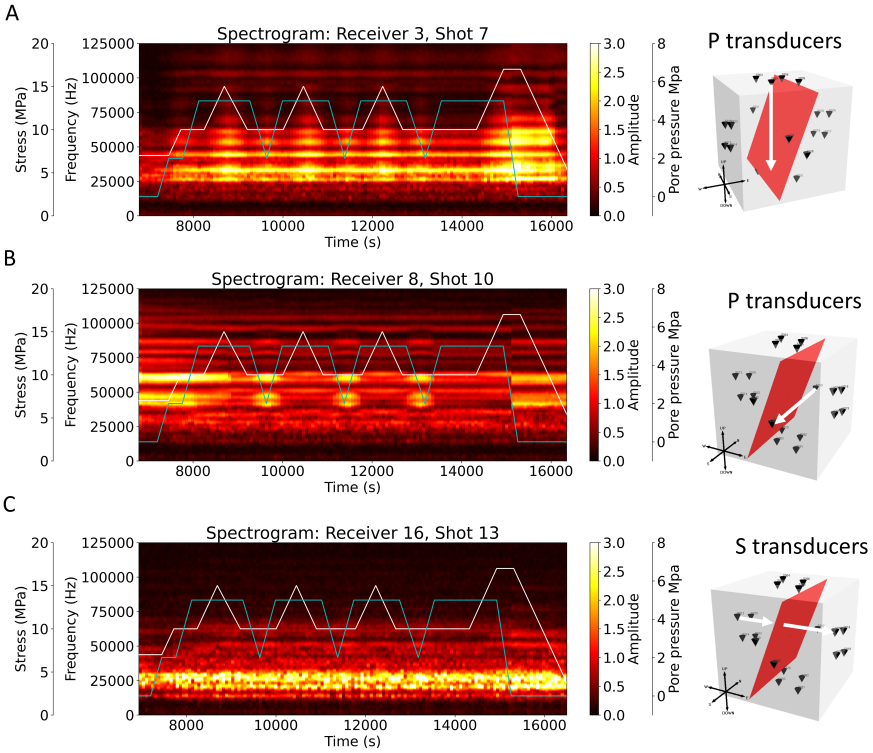

Figure A.1: Spectrogram of the transmission pairs of Figure 6.8. The vertical load on the sample (σ_1) and the pore pressure are plotted on top. A. a P-wave transducer pair for σ_1 direction. B. a P-wave transducer pair for σ_2 direction. C. a S-wave transducer pair for σ_3 direction.

Increasing vertical stress (σ_1) and changes in the pore pressure cause an amplification effect around certain frequency bands (Figures A.1, A.2,and A.4). This shows the influence of stress direction, as in Figure A.1B, and A.2B. The cycling pore pressure has most influence, while increasing the stress perpendicular to the measuring direction has minimal influence. The increased stress on the sample can cause less attenuation of the transmitted waves (chapter 2). Changing coupling can also have a large effect on the wave propagation, however, this should be a constant as the additional stress is compensated for by the spring behind the transducers (Figure 6.4).

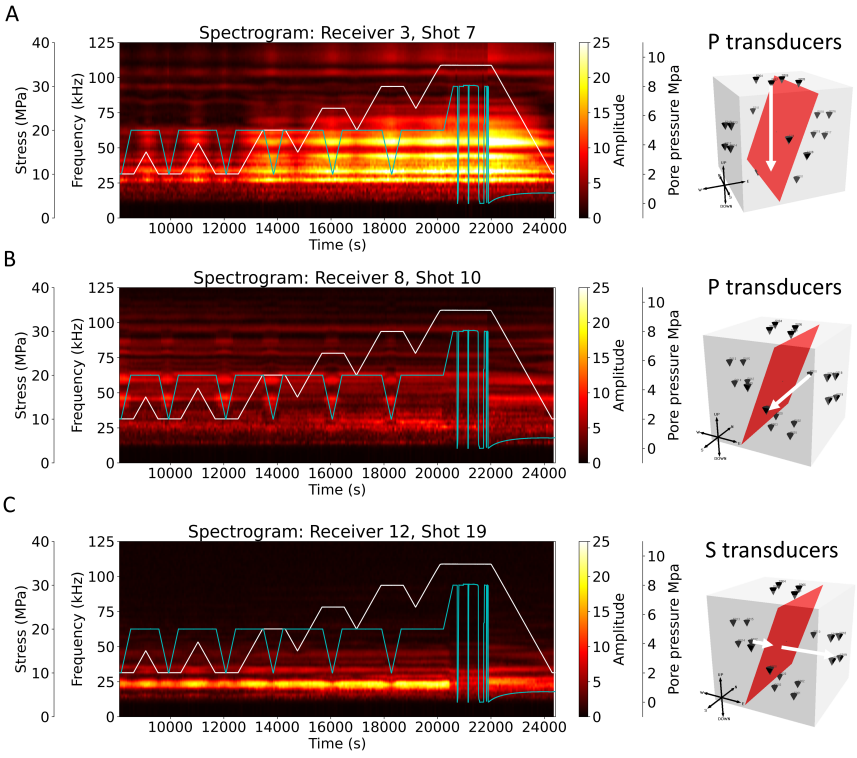

Figure A.2: As Figure A.1, but for the transmission pairs of Figure 6.11.

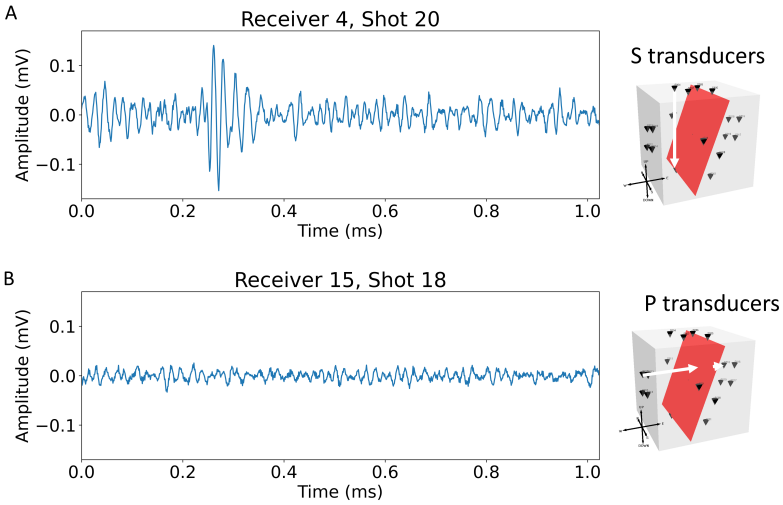

Figure A.3: Recorded wavelets of survey 170 (at time 20287 sec, during last cycle), Extra pair P-wave and S-wave pair for σ_1 direction and the σ_3 direction.

In chapter 6, only 1 transducer pair is shown for each loading direction. This is a P-wave pair in the Z- direction and a S-wave pair in the X-direction (the Y-direction only has P-wave pairs). To be complete, the recorded waves, the spectograms, decorrelation coefficient and transmitted amplitudes of a S- and P-wave pair for both directions are shown in Figures A.3 to A.6.

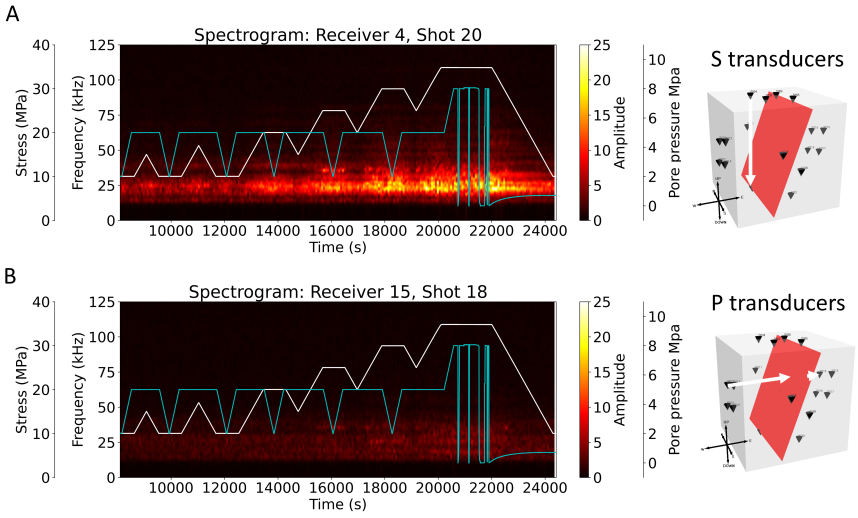

Figure A.4: As Figure A.1, but for the transmission pairs of Figure A.3.

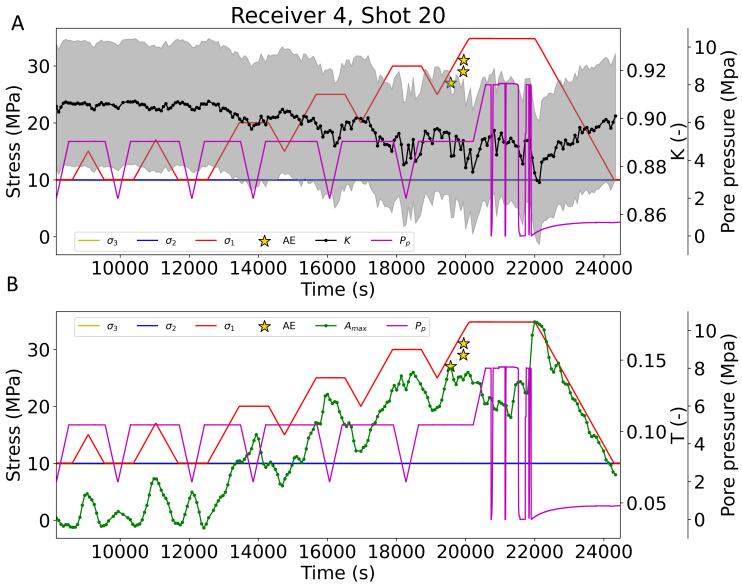

Figure A.5: The evolution of decorrelation coefficient K, and the transmitted maximum amplitude T for the duration of the second experiment in the Z-direction (σ_1 direction). Note the amplitude of the AE events can be seen in Figure 6.12.

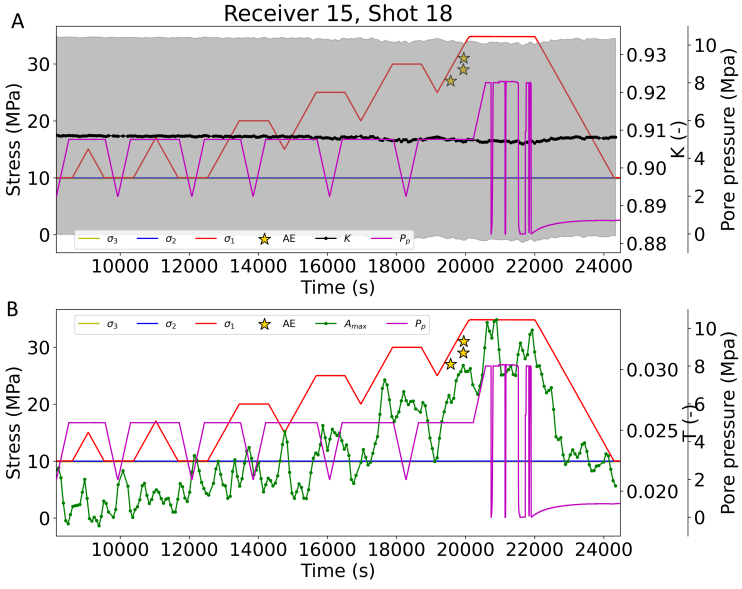

Figure A.6: As Figure A.5, but in the X-direction (σ_3 direction).

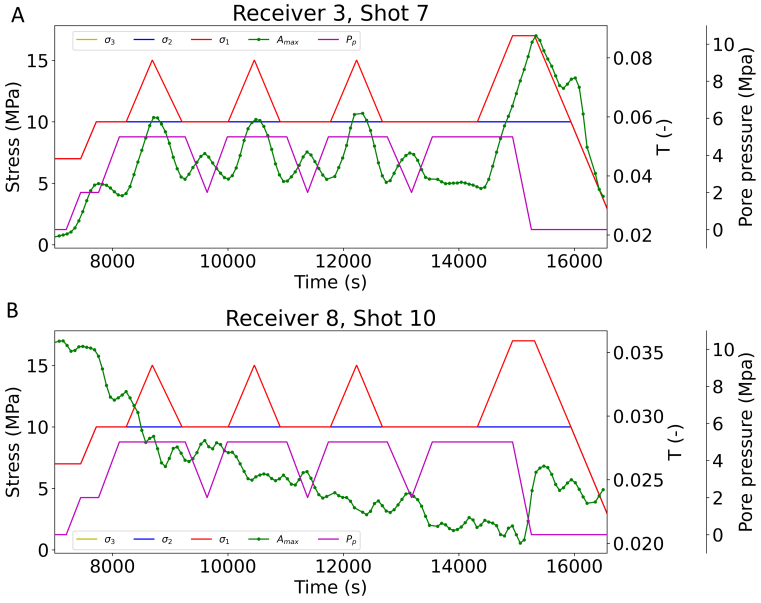

Figure A.7: The evolution of transmitted amplitude for (P-wave) transmission pair during the first experiment. A. in Z- or σ_1 direction and B. in Y- or σ_2.

The maximum transmitted amplitude for the transmission pairs during the first experiment are shown in Figure A.7. The amplitude follows the main stress changes in the Z-direction, but doesn't show a clear trend in the Y-direction. No clear indication to fault reactivation within the first experiment is visible from this data set either.

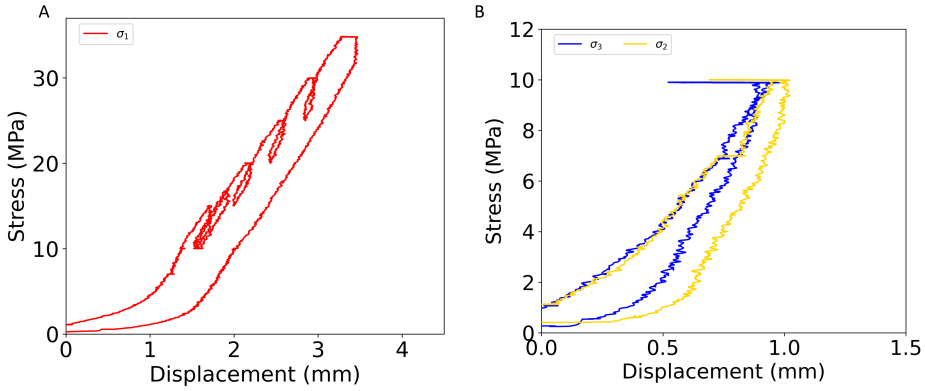

Figure A.8: Stress versus displacement for three directions. A. Axial stress versus deformation in Z direction (σ_1) showing inelastic deformation at the end of the experiment. B. Horizontal stresses versus deformation in X and Y direction (σ_3, σ_2)

The inelastic deformation is visible in the stress versus displacement graph (Figure A.8). In each cycle, some permanent deformation is visible. When returning to the original stress levels, it can be seen that about 0.6 mm displacement was induced in σ_1 direction. The recorded changes in K during the first loading protocol are very subtle, and are minimal compared to the standard deviation (Figure A.9).

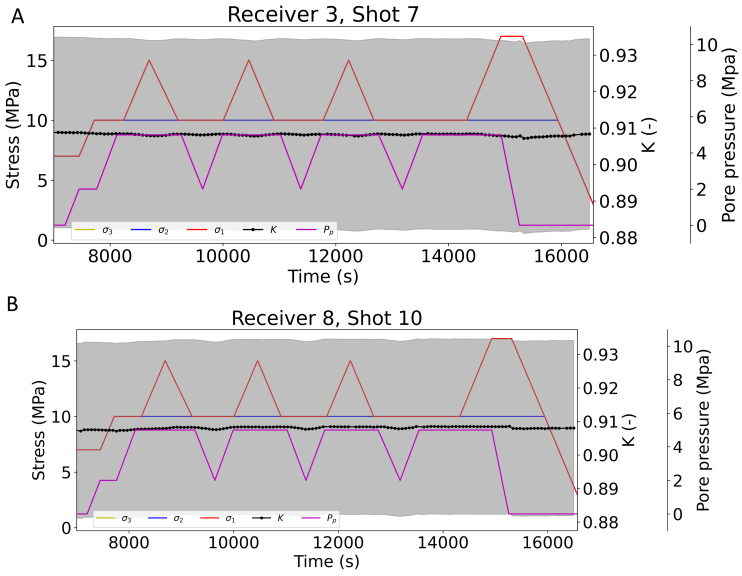

Figure A.9: The evolution of decorrelation coefficient K, including the standard deviation for the first loading protocol.

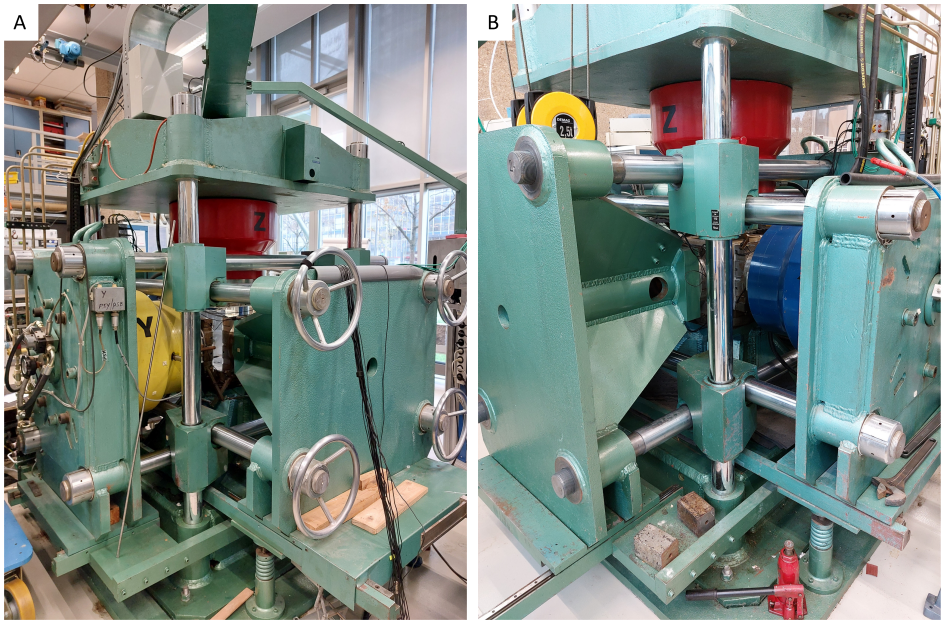

Figure A.10: Pictures showing the true triaxial loading machine in the lab. The piston of the vertical load Z is red, the yellow is the horizontal Y direction, and the blue the X direction. The opposite of the piston is the door, blocking movement. In this experiment Z = σ_1, Y = σ_2, and X = σ_3.

Figures A.10 to A.14 show pictures in the laboratory showing the loading machine and installation of the sample.

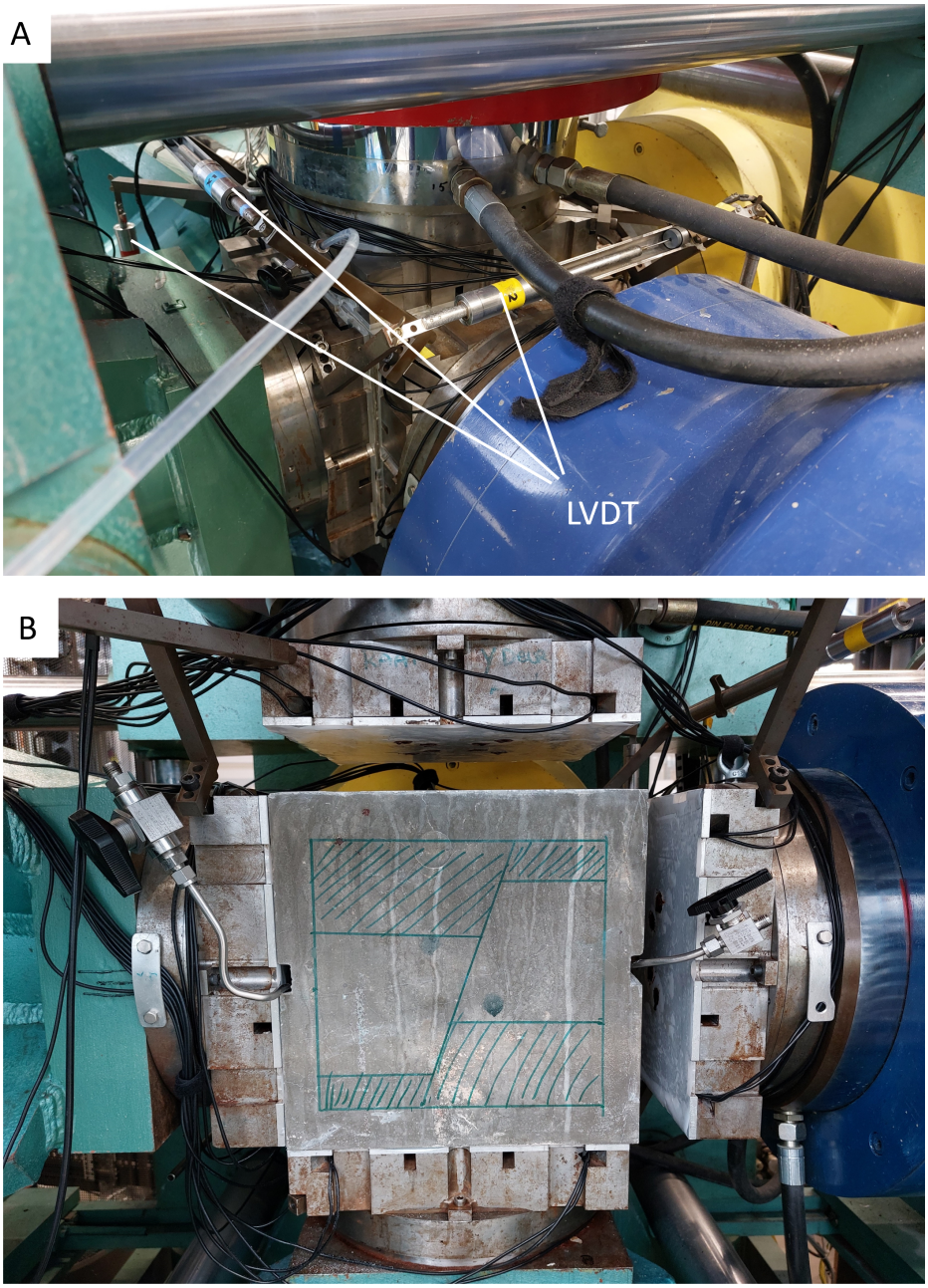

Figure A.11: Pictures showing a close up of the sample in the true triaxial loading machine in the lab. The piston of the vertical load Z is red, the yellow is the horizontal Y direction, and the blue the X direction. The opposite of the piston is the door, blocking movement. In this experiment Z = σ_1, Y = σ_2, and X = σ_3. The LVDT's are indicated in A and B showing the orientation of the sample in the machine and the fluid lines.

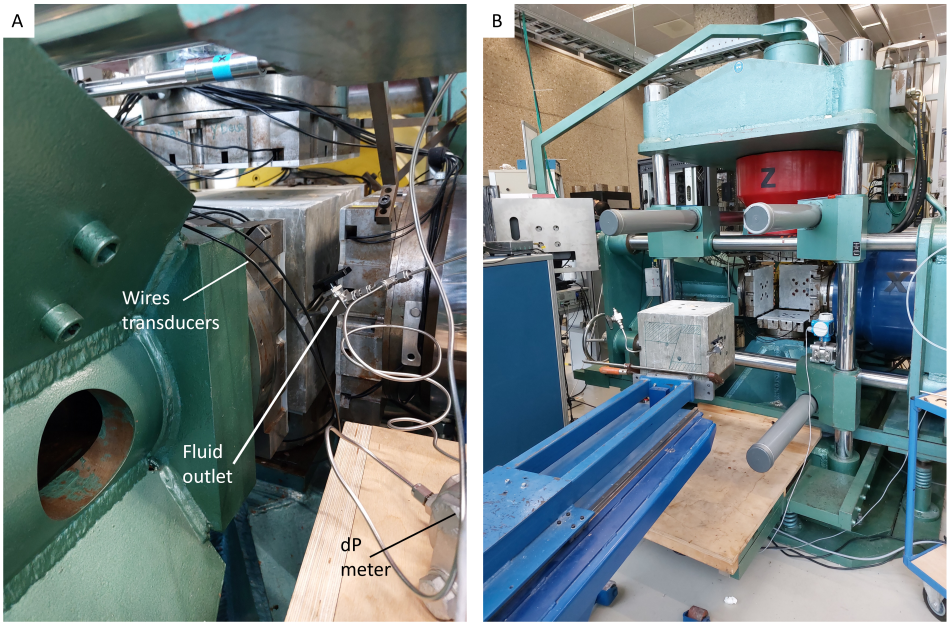

Figure A.12: Pictures showing the installment of the sample in the true triaxial loading machine in the lab. The piston of the vertical load Z is red, the yellow is the horizontal Y direction, and the blue the X direction. The opposite of the piston is the door, blocking movement. In this experiment Z = σ_1, Y = σ_2, and X = σ_3. A showing the fluid lines exiting the sample and the attachment to the differential pressure meter (dP meter) and all the wires from the transducers going to the acoustic acquisition system. B showing the sample just before installing it within the machine, note the plates are lined with Teflon sheets.

Figure A.13: Pictures showing the acoustic measurement set-up. A showing the plates with the transducers. B showing the Richter acoustic emission system, with the master computer on the top and directly below that 4 multichannel systems, below the screen the pulser amplifying system for amplification and active surveys and on the side mounted to the blue sheets, pre-amplifiers. C the bottom side, without the top-plate, showing the space for cables and transducers.

Figure A.14: Overview of the set up in the laboratory, including on the far left, indicated with an A the acquisition system of the dP meter, next to that B: the computers controlling the three principal stresses, Z = σ_1, Y = σ_2, and X = σ_3. In the back, behind the true triax, C: the acoustic acquisition system. D, the true triax in the middle and E on the right the 2 ISCO pump controlling the pore pressure,

B

SUPPLEMENTARY INFORMATION

Data availability.

The laboratory facilities at TU Delft were used to perform the experiments and record the data (loading data and waveforms) used in this thesis. These data are accessible at the 4TU.ResearchData repository.

- Chapter 2: Veltmeijer, Aukje; Naderloo, Milad; Barnhoorn, Auke (2023): Supporting data for the article “Forecasting of Rock Failure in the Laboratory using Active Acoustic Monitoring Methods”. 4TU.ResearchData. dataset. https://doi.org/10.4121/21557910
- Chapter 3: Veltmeijer, Aukje (2024): Supporting data for "Early detection of stress changes and failure using acoustic measurements - Chapter 3 Precursory signals to the onset of laboratory stress-driven fault slip through acoustic monitoring". 4TU.ResearchData. dataset. https://doi.org/10.4121/d5278a83-81d1-4a9c-8514-3ce8cd8991f7
- Chapter 4: Veltmeijer, Aukje; Naderloo, Milad (2024): Supporting data for: "Active and Passive Monitoring of Fault Reactivation under Stress Cycling". 4TU.ResearchData. dataset. https://doi.org/10.4121/d40d3812-c3db-46bb-8394-24473c735b23
- Chapter 5: Veltmeijer, Aukje; Naderloo, Milad; Anne Pluymakers; Barnhoorn, Auke (2023): Supporting data for the article “Monitoring and Forecasting Injection Induced Fault Reactivation and Seismicity in the Laboratory using Active Acoustic Methods”. 4TU.ResearchData. dataset. https://doi.org/10.4121/b4d97366-a512-4a93-9fe5-3cbda29fa9de
- Chapter 6: Veltmeijer, Aukje; Naderloo, Milad (2024): Supporting data for "Early detection of stress changes and failure using acoustic measurements - Chapter 6 Monitoring stress variations in layered offset samples in a true triaxial setting". 4TU.ResearchData. dataset. https://doi.org/10.4121/38262dab-3eea-4991-87a0-1b7e849efbfb

ACKNOWLEDGEMENTS

A little over 4 years ago, I started this PhD Journey. Throughout this time, I have received invaluable support from numerous persons. First and foremost, my gratitude goes to my promotors, Auke and Kees. Auke, thanks for the supervision over the last few years. You have given me lots of freedom to explore, learn, and figure things out myself, but were always ready to help, guide or steer me in the right direction. Your presence and concern for my well-being during the COVID pandemic, along with the creation of fun activities to make this period more enjoyable, are deeply appreciated. Kees, even though we didn't meet as often, you were always there for questions and feedback; your attention to detail has shaped this thesis into what it is.

Many thanks to my "lab buddy" Milad. Milad, I enjoyed working with you in the lab a lot, even though you always insisted on being at least 2 min late. We have performed many experiments together in the lab; some successful and some slightly less so. At least now I know you need to wash your clothes three times to remove hydraulic oil. I had a great time in the lab, even when this was very difficult during the COVID time; we have somehow made it work out well and always managed to joke around. The highlight of them all was of course when we managed to finally perform the big block experiments!

Of course, I also want to thank the others in our lab group for also experiencing that lab experiments do not always work out the way you want them. Anne, Chris, Kai, Shihou, Jon, Martijn, Entela, Parvin, and Debanjan. thanks for all the help and the insightful discussions over the years. Thanks, Anne and Auke for organizing our meetings outside in the park in front of the university during COVID. This was much needed, I enjoyed this a lot, even when it rained...

Special appreciation is reserved for the laboratory technicians, without whom none of the experiments would have been possible. Marc, your assistance with the machines, along with your musical serenades and encouragement in the lab, has been invaluable. Karel, thanks for always being there to help out with the acoustics, and creating the memorable passwords, which seemed to change every other week. Jens for providing all kinds of solutions to our problems and popping by in the afternoon just to have a look at what's going on.

I started this PhD journey alongside Aleks, Faezeh, Hamed, Iban, Jingming, Milad, Sara, and Samantha, forming our DeepNL office. Thanks for making our shared office lively with "inspirational" quotes, memes, plants, paintings, and not to forget Hamed's stuffed animal collection. Every time I went to a conference, I looked for a new addition to your furry friends. I had a great time with all of you the last couple of years. Faezeh and Jingming, I will miss our morning coffees; these were a great start of the day. Remember: "most terrible, best terrible." Even though we didn't agree yet on what this was supposed to mean, I liked the explanation that, hard or difficult times, will be remembered as the best times. Menno, you started around the same time and got to be an honorary member

of our DeepNL office. I greatly enjoyed our coffees in the afternoon, during which we could talk forever about whatnot.

I want to extend my gratitude to Florencia, Johno, and Billy for inviting me to the DOGS board. This has been a great experience at TU Delft. Johno, thank you for acknowledging my time as DOGS president has been the best. I also enjoyed ridiculing each other's research a lot. Thanks to David, Entela, and Iban, who joined the board later; it has been a pleasure.

My time at university has been enjoyable because of all my friends and colleagues over the years. Thanks to Amin, Andrea, Aydin, Camille, Chris, Eddy, Eli, Evvgenia, Fardad, Ilshat, Jasper en Jasper (you can decide among yourselves who is who), Joeri, Mahmoud, Marat, Maria, Martha, Max, Musab, Nazife, Nicolas, Sepideh, Sverre, Tim, and Yusuke for all the good times.

Outside of university, judo provided a source of relaxation and stress relief. My gratitude to Sophie, Marie, Sylvia, Michel, Simon, Jasper, Maurice, and all the others I undoubtedly forgot to mention.

My list wouldn't be complete without "Team Subliem": Hendrik and Michael. Michael, thanks for all the early dinners during COVID times and later when you started working up north; all the calls at 16.30 to announce your working day is already over. Hendrik for always making some time in your crazy travel schedule. And of course, Mark and Hugo, with whom I could always talk about the struggles of being a PhD candidate.

Finally, I want to thank my brothers, Steyn and Itse, and my parents for their support and love no matter what.

CURRICULUM VITÆ

Aukje Veerle VELTMEIJER

17-03-1996 Born in Delft, the Netherlands.

EDUCATION

2008–2014 Secondary School, pre-university education (VWO)
Grotius College, Delft, the Netherlands

2014–2017 B.Sc. Applied Earth Sciences
Delft University of Technology (TU Delft), the Netherlands

2016 Exchange Semester
University of Maryland (UMD), United States of America

2017–2019 M.Sc. Applied Geophysics
Delft University of Technology (TU Delft), the Netherlands
Swiss Federal Institute of Technology (ETH Zürich), Switzerland
Aachen University (RWTH Aachen), Germany

2019–2024 Ph.D. Applied Geophysics & Petrophysics
Delft University of Technology (TU Delft), the Netherlands
Thesis: Early detection of stress changes and failure using acoustic measurements
Promotors: Dr. A. Barnhoorn
Prof. dr. ir. C.P.A. Wapenaar

PUBLICATIONS

LIST OF PULICATIONS

5. M. Naderloo , **A. Veltmeijer**, A. Pluymakers & J.D. Jansen & A. Barnhoorn, *The Effect of Pressurization Rate and Pattern on Injection-induced Seismicity in Porous Media: An Experimental Study.* Journal of Geophysical Research: Solid Earth, (2024) (under review)

4. **A. Veltmeijer**, M. Naderloo & A. Barnhoorn, *Forecasting of Rock Failure in the Laboratory using Ultrasonic Monitoring Methods.* Geomechanics and Geophysics for Geo-Energy and Geo-Resources. (2024). (accepted, pre-print available at ESS Open Archive)

3. F. Shirmohammadi, D. Draganov, **A. Veltmeijer**, M. Naderloo & A. Barnhoorn, *Feasibility of reservoir monitoring in the Groningen gas field using ghost reflections from seismic interferometry.* Geophysical Journal International. Geophysical Journal International, **237**, 2 (2024).

2. **A. Veltmeijer**, M. Naderloo, A. Pluymakers & A. Barnhoorn, *Precursory Signals to Injection Induced Fault Reactivation in the Laboratory using Active Acoustic Ultrasonic Monitoring Methods.* Journal of Geophysical Research: Solid Earth, **129**, (2024).

1. M. Naderloo , **A. Veltmeijer**, J.D. Jansen & A. Barnhoorn, *Laboratory study on the effect of stress cycling pattern and rate on seismicity evolution* Geomechanics and Geophysics for Geo-Energy and Geo-Resources, **9**, 137 (2023).

LIST OF CONFERENCE PROCEEDINGS

6. **A. Veltmeijer**, M. Naderloo, & A. Barnhoorn, *Active and Passive Seismic Monitoring of Laboratory-Based Injection-Driven Fault Reactivation* , 84th EAGE Annual Conference & Exhibition (2023).

5. **A. Veltmeijer**, M. Naderloo, & A. Barnhoorn, *Seismic monitoring of laboratory fault reactivation by pore fluid injection.*, EGU General Assembly (2023).

4. **A. Veltmeijer**, M. Naderloo, A. Pluymakers & A. Barnhoorn, *Acoustic Monitoring of Laboratory Induced Fault Reactivation*, 83rd EAGE Annual Conference & Exhibition (2022).

3. M. Naderloo, **A. Veltmeijer**, & A. Barnhoorn, *Active and Passive Monitoring of Fault Reactivation under Stress Cycling.*, Second International Meeting for Applied Geoscience & Energy (2022).

2. **A. Veltmeijer**, M. Naderloo, & A. Barnhoorn, *Acoustic Precursors to Laboratory Induced Fault Slip and Failure.*, EGU General Assembly (2022).

1. **A. Veltmeijer**, M. Naderloo & A. Barnhoorn, *Monitoring and forecasting failure in laboratory using coda wave decorrelation*, EAGE GeoTech 2021 First EAGE Workshop on Induced Seismicity (2021).